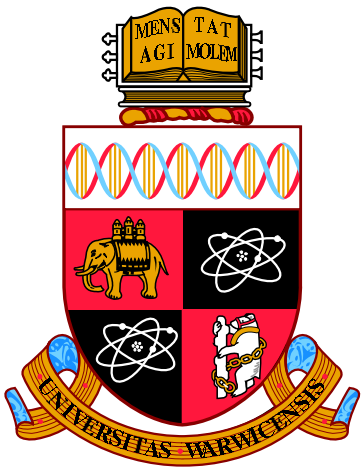

Molecular Simulations of Model Bilayers of Skin Lipids

by

David William O'Neill

Thesis

Submitted to the University of Warwick

for the degree of

Doctor of Philosophy

Chemistry

July 2019

THE UNIVERSITY OF WARWICK

Contents

List of Tables

List of Figures

Acknowledgments

First of all I would like to gratefully thank my supervisor Dr Rebecca Notman for all help and support throughout my time at Warwick. I'd like to thank her for all her patience as I know I'm not always the easiest person to deal with. I'd like to give personal thanks to Dr Annalaura Del Regno for her fruitful discussions on our work and hoe she's always willing to help me out. Thanks must go to all current and previous Notman group and Habershon group members for providing an enjoyable working environment.

I'd like to acknowledge the Centre for Scientific Computing, University of Warwick for the provision of computing facilities and to give thanks to the EPSRC for a PhD Studentship.

Finally, I'd like to that all my Family and friends for their unwavering love and support throughout this difficult, and at sometimes dark, journey!

Declarations

I confirm that my thesis has been prepared in accordance with the University of Warwick's guidelines on the presentation of a research thesis. It has been written by myself, except where acknowledged in the text. No part of this thesis has been previously submitted for examination for any other higher degree.

To date part of the Introduction in Chapter 1 has been published in a book chapter and a bilayer structure used in Chapter 4 was used in a published paper.

Computer Simulations of Lipid Membranes and Liposomes for Drug Delivery, DW ONeill, SY Noh, R Notman, Computational Pharmaceutics: Application of Molecular Modelling in Drug Delivery, 2015

Ethanol induces the formation of water-permeable defects in model bilayers of skin lipids, R Thind, DW O'Neill, A Del Regno, R Notman, Chemical Communications 51 (25), 5406-5409, 2015

Abstract

The lipid matrix within the SC is believed to be the main contributor to the skin's barrier properties. But the major problem is that the organisation of the lipids into the lamellar layers and their contribution to the barrier properties of the skin remains poorly understood. This thesis has attempted to address this issue through the use of molecular simulations of model bilayers of the SC under a variety of different conditions. The use of molecular dynamics simulations has allowed these membranes to be studied at the atomistic level that isn't accessible through conventional experiments.

It is shown that the hydration level within the lipid matrix has a direct impact on the bilayer conformation and thus the barrier properties of the SC. At low hydration a pooling effect is observed on the bilayer surface, which affects the order and orientation of the CERs. Lowering the hydration reduces the amount of CER-water hydrogen bonds and replaces them with adjacent CER-CER hydrogen bonds. The lateral hydrogen bonding network remains unchanged.

Through free energy calculations and the calculation of permeability coefficients, a mixed system of CER and OA has a greater permeability than either of its pure counterparts and thus would be a more favourable pathway for permeants, such as water, to migrate through. This enhanced permeability is shown to be due a combination of weakening the lateral hydrogen bonding network and disrupting the packing with it's 'kinked' tail.

Finite size and solvent effects on CG simulations with the interaction of DMSO on CER bilayers are presented. At low solvent to lipid ratios and larger bilayers, the small solvent chamber allows interactions of the CER bilayer with it's periodic image causing disruption to the conformation and leading to a change to a hexagonal phase. Solvent effects are observed when the amount of DMSO at the interface is higher for larger bilayer systems despite the same solvent to lipid ratio as a larger surface area can accommodate a greater number of DMSO molecules at the interface. Our results suggest that the system sizes of at least 256 lipids and 30 solvent molecules per lipid are required to avoid finite size effects in simulations of lipid membranes in mixed solvents.

Abbreviations

ACF Autocorrelation function

APL Area per lipid

CER Ceramide

CG Coarse-grained

CHOL Cholesterol

COM Centre of Mass

CEMOVIS Cryo-electron microscopy of vitreous skin section

DMSO Dimethylsulfoxide

DMPC 1,2-Dimyristoyl-*sn*-glycero-3-phosphocholine

DPPC 1,2-Dipalmitoyl-*sn*-glycero-3-phosphocholine

DSC Differential scanning calorimetry

FF Force field

FT Fourier transform

FFA Free fatty acid

FG Functional group

GROMACS GROningen MAchine for Chemical Simulations

HB Hydrogen bond

LJ Lennard-Jones

LPP Long periodicity phase

MD Molecular dynamics

NPT Isobaric-isothermal ensemble

NVE Microcanonical ensemble

NVT Canonical ensemble

OA Oleic acid

PABA p-aminobenzoic acid

PME Particle Mesh Ewald

PMCF Potential of mean constraint force

POPC 1-Palmitoyl-2-oleoyl-*sn*-glycero-3-phosphocholine

POPE 1-Palmitoyl-2-oleoyl-*sn*-glycero-3-phosphoethanolamine

RDF Radial distribution function

SPP Short periodicity phase

Chapter 1

Introduction

1.1 Statement of the Problem

The stratum corneum (SC) is the topmost layer of the skin which forms the main barrier to penetration of substances across the skin and to water loss from inside the body. An understanding of the molecular structure and organisation of the SC skin barrier is essential for many applications. In medicine, such knowledge is needed for developing new treatments for skin diseases and for the development of transdermal drug delivery products. In addition, the cosmetic industry continually develops personal care products, which are applied to the SC, to help protect and maintain healthy skin. Realising the potential of haptic technologies such as in electronic devices and for virtual training environments also depends on furthering this understanding. Understanding the level of toxicity and bioavailability of products such as hand gels, make-up and moisturisers on the skin are important so that they are safe for the public to use. Additionally, there are ethical issues associated with testing these products on animals. Understanding the mechanism of action of penetration enhancers that modify the barrier properties of skin in order to deliver drugs via the transdermal route, is also of high interest as it may aid in rational design of new penetration enhancers.

The SC consists of flattened, dead skin cells, called corneocytes, surrounded by layers of lipids. It is believed that the lipid layers are the main contributors to the skin's barrier properties. These lipids layers are composed primarily of ceramides (CERs), cholesterol (CHOL) and free fatty acids (FFAs). One of the major problems is that the organisation of the lipids into the lamellar layers and their contribution to the barrier properties of the skin remains poorly understood. This due to the difficulty of high resolution imaging of lipid phases and packing by experiments.

Molecular simulations can be a powerful tool to compliment, help interpret and guide experiments. They have less ethical and environmental issues than experiments. Molecular simulation allows us to probe the SC at atomic resolution. It gives a detailed picture of the interactions of the components of the skin at the molecular level and can provide insights as to how they contribute to the skins barrier properties while retaining its

flexibility. Since we dont have a definitive model, whether it is experimental or computational, one has to find a way of developing a model acting as a skin-lipid substitute that maintains the barrier properties characterized by the skin. The study presented here aims to investigate models of the skin lipids and their interactions under a number of conditions including level of hydration; and in the presence of the penetration enhancing molecules oleic acid (OA) and dimethylsulfoxide (DMSO) using molecular simulation.

This Chapter presents the background to the study. First, the knowledge of the structure and function of the skin is discussed, with a focus on the top layer of the skin, the SC. The roles of the SC lipids and how they are organised within this layer according to experiment are described. This is followed by a review of molecular simulations of skin. The next section explores skin penetration including its importance in transdermal drug delivery, the theory behind it, and a review of the key experimental and theoretical studies. Finally, chemical penetration enhancers are introduced with an overview of their properties and general mechanisms of action. Two well known penetration enhancers, that are studied in this thesis, OA and DMSO, are discussed in detail in a review of relevant experimental and simulation literature.

1.2 Structure and Function of Skin

1.2.1 Overview

The skin is the largest organ of the body allowing the transfer of water and heat in and out of the body. It is flexible, robust and can repair itself. The primary function of the skin is to act as a physical barrier to prevent toxic chemicals and micro-organisms from entering the body and causing harm. A virtue of being large and accessible is that it becomes an ideal route to administer therapeutic agents into the body via transdermal drug delivery. The skin can be categorised into four main layers: the subcutaneous fat layer, the dermis, the viable epidermis and the outermost layer, the SC, as seen in Figure 1.1.

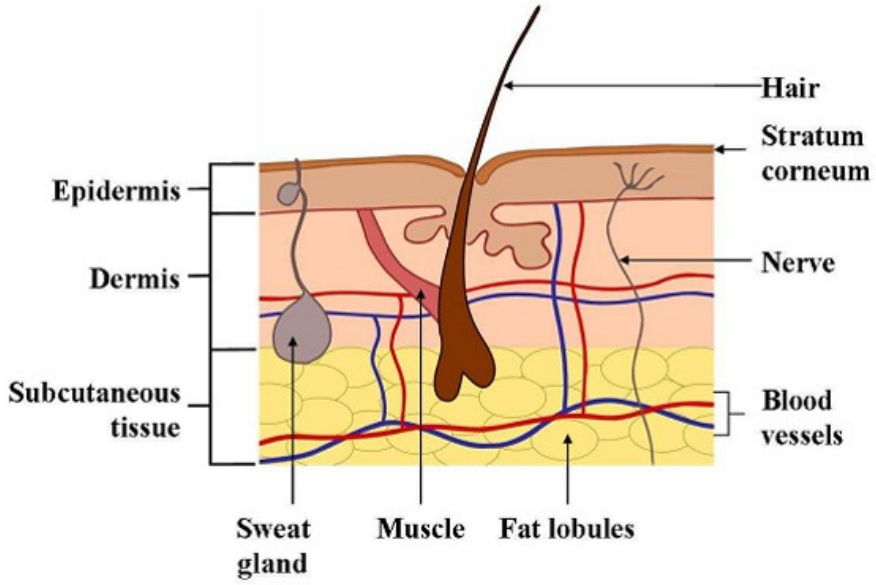

Figure 1.1: Schematic representation of the skin categorised into four main layers: the subcutaneous tissue, the dermis, the epidermis, and the top layer of the skin, the SC. Figure reproduced from Notman[1] with permission from author.

1.2.2 Subcutaneous Tissue

The subcutaneous fat layer is the link between the dermis and the underlying body constituents. Nerves and blood vessels are carried to the skin in this thick layer. The layer also gives insulation and provides an energy storage area.

1.2.3 Dermis

The dermis, with a thickness between 500-3000 μm, is the major component of the skin comprising of a network of connective tissue embedded with sebaceous, apocrine and eccrine (sweat) glands, blood vessels and nerve endings. As a consequence it is essential for maintaining body temperature and for the transport of oxygen, nutrients, toxins and waste. This layer provides minimal barrier to the delivery of most polar drugs, and when permeating substances reach this layer of the skin they will be carried away in the blood.

1.2.4 Viable Epidermis

The viable epidermis is a thin layer(100 μm thick) containing no blood vessels. As a result waste products diffuse across the dermo-epidermal layer. The function of the viable epidermis is to produce the SC and regenerate cells lost at the surface (desquamation). The epidermis is split into four distinct layers that represent the state of differentiation of the constituent skin cells, the keratinocytes. The keratinocytes are produced in the stratum basale before migrating towards the surface. In the stratum spinosium these keratinocytes are characterised by the presence of lamellar bodies that

contain parallel stacks of lipids. The cells are flattened in the stratum granulosum and lamellar constituents are bountiful. These lamellar bodies fuse with cell membranes, at the interface, spilling the contents into the SC. Hydrolysis of these lipids produces the CERs and FFAs that form the SC lipid lamellae.

1.2.5 Stratum Corneum (SC)

The SC is the topmost layer of the skin, which forms the main barrier to penetration of substances across the skin and to water loss from inside the body, despite being only 10-40 μm thick. The SC is produced in the final stage of differentiation of the epidermis. The keratinocytes are flattened into keratin-rich cells known as corneocytes and a mixture of lipids is released into the intercellur space. The SC is often considered to be organized in a bricks and mortar arrangement, with the corneocytes (bricks) surrounded by the lipid matrix (mortar)[10]. An overview on the skin detail can be seen in Figure 1.2.

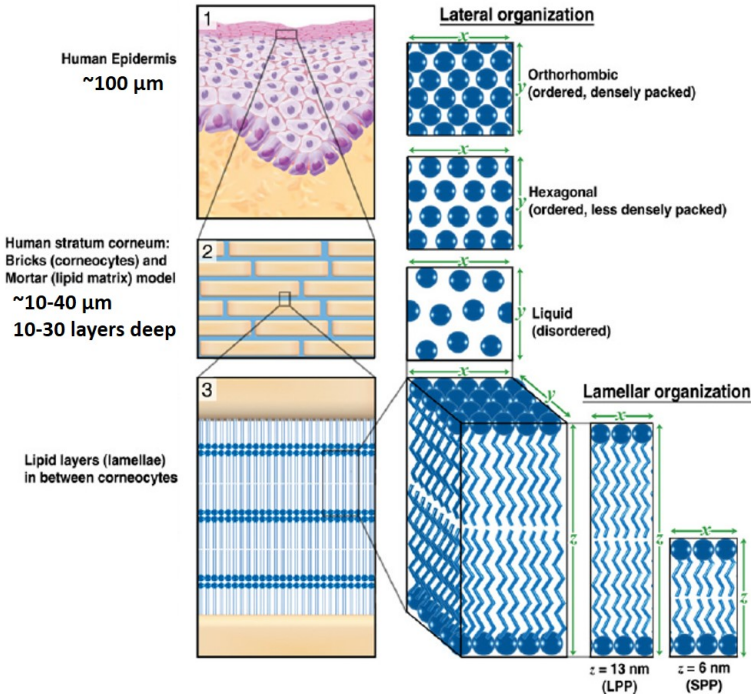

Figure 1.2: The epidermis is composed of four different layers. (1) The topmost layer of the epidermis, the SC, is formed by a brick (corneocytes) and mortar (lipids) structure (2). The lipid layer consists of multiple intercellular lamellae (3) with two coexisting lamellar phases. The lamellar organisation is categorised either as long periodicity phase (LPP) or short periodicity phase (SPP), depending on the type of CER. The lateral organisation can be a liquid, hexagonal or orthorhombic phase. Figure has been adapted from Janssens *et al.*[2] with permission from the American Society for Biochemistry and Molecular Biology.

This lipid matrix is arranged in lamellar layers which form the main barrier to penetration[11]. As a result of this barrier, only a limited amount of water can permeate through the lipid layers (known as transepidermal water loss) and out into the atmo-

sphere. This helps to maintain the low hydration of the lipids and may impart some flexibility to the structure.

1.2.6 Stratum Corneum Lipids

The lipid mixture that forms lamellar layers surrounding the corneocytes is made up of three major components; CERs, CHOL and FFAs. Each of these components has specific properties that help give the SC its strong barrier properties but at the same time allows it to be soft and flexible. Out of the three components, it is known that the CER class of lipids plays a pivital role in the barrier function of the skin[12]. There are at least 11 different types of CER[13] found in human SC, their molecular structures are shown in Figure 1.3. The fatty acid chains of the CERs ranging from 12 to 36 carbon atoms with the most common chain length being 24 carbons long[14]. Generally these chains are saturated allowing for tight lateral packing. As a result CERs exist in the ordered gel phase at room temperature[15]. One of the major properties that imparts structural integrity to the SC and allows it to act as a strong barrier is the hydrogen bonding network between headgroups of neighbouring CERs and CERs in other lamellar layers[16]. This network imparts structural integrity to the SC.

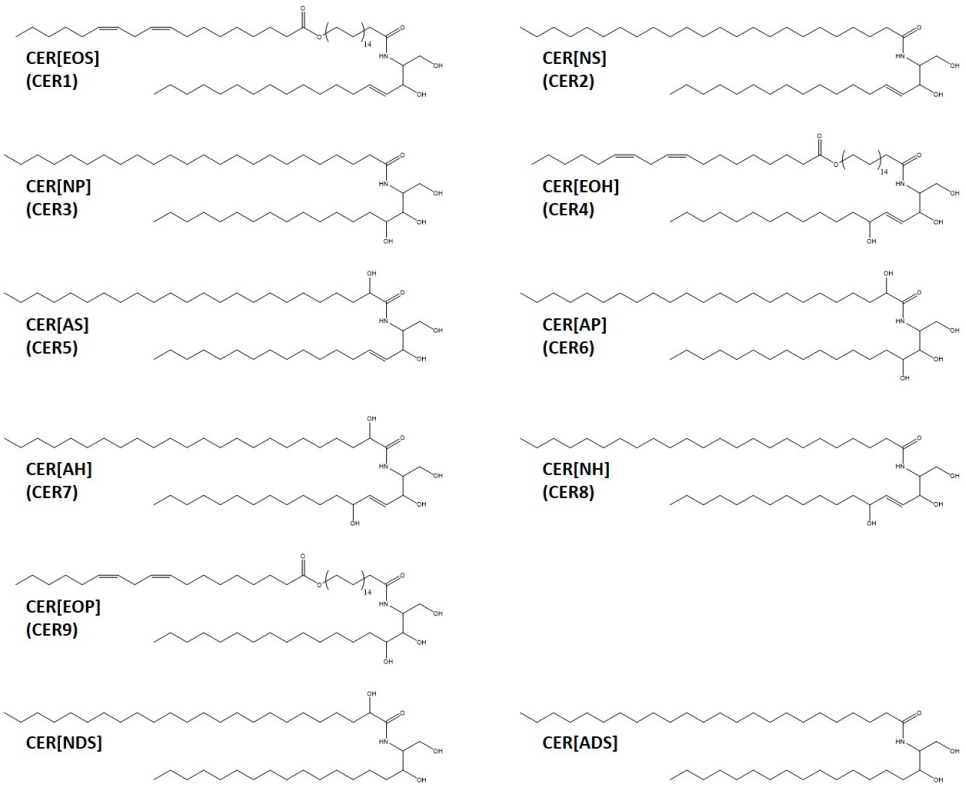

Figure 1.3: Molecular structures of CERs 1-11 found in the SC. A, α-hydroxy fatty acid; DS, Dihydrosphingosine; H, 6-hydroxysphingosine; N, nonhydroxy fatty acid; P, phytosphingosine; S, sphingosine; EO, ω-esterified fatty acid.

CHOL is a lipid found in animal membranes that can change the fluidity of membranes

depending on the constituents it interacts with. For example, differential scanning calorimetry (DSC)[17,18] and Fourier transform(FT)-Raman spectroscopy[18] experiments where CER were mixed with CHOL, showed that CHOL increased chain disorder of CERs. Therefore, the role of CHOL is thought to provide a degree of fluidity to what would be a rigid structure.

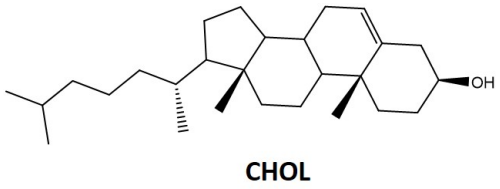

Figure 1.4: Molecular structure of CHOL.

FFAs, on the other hand, increase the density of the hydrocarbon chain packing[5,19] which suggests that they order the lipids. They also disrupt the CER headgroup packing by forming hydrogen bonds (HBs) with the lipid headgroups[20]. The large heterogeneity of the CERs and FFA hydrocarbon chain lengths give rise to a variety of lipid-lipid interactions within the lipid mixture. These interactions give rise to the unique and complex properties of the skin barrier.

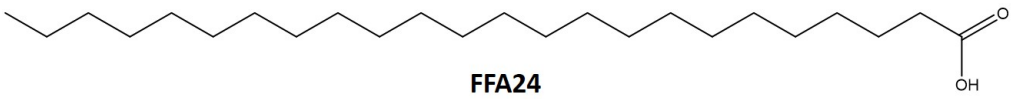

Figure 1.5: Molecular structure of FFA with 24 carbon atom chain.

1.2.7 Stratum Corneum Lipid Organisation

Lipids can be organised in a number of ways based on their packing and phase. The lipid lamellar structure is determined by the headgroup arrangement and the packing of the hydrocarbon tails. For CERs, these lateral organisations can be categorised as orthorhombic crystalline, hexagonal gel and liquid lamellar, and are dependent on the temperature. Each of these phases is shown in Figure 1.6. Wide angle diffraction of human and bovine SC shows peaks that correspond to orthorhombic patterns of 0.375 and 0.416 nm and liquid lamellar pattern of 0.46 nm. At 318 K, the orthorhombic and liquid lamellar patterns cease, to be replaced by only the 0.412 nm peak that corresponds to the hexagonal gel pattern, indicating that the system becomes a single phase on an additional temperature increase[21,22]. Temperatures above 343 K in human SC allow the motility of the hydrocarbon chains to increase, leading to the observation of the peak liquid lamellar pattern of 0.46 nm[23].

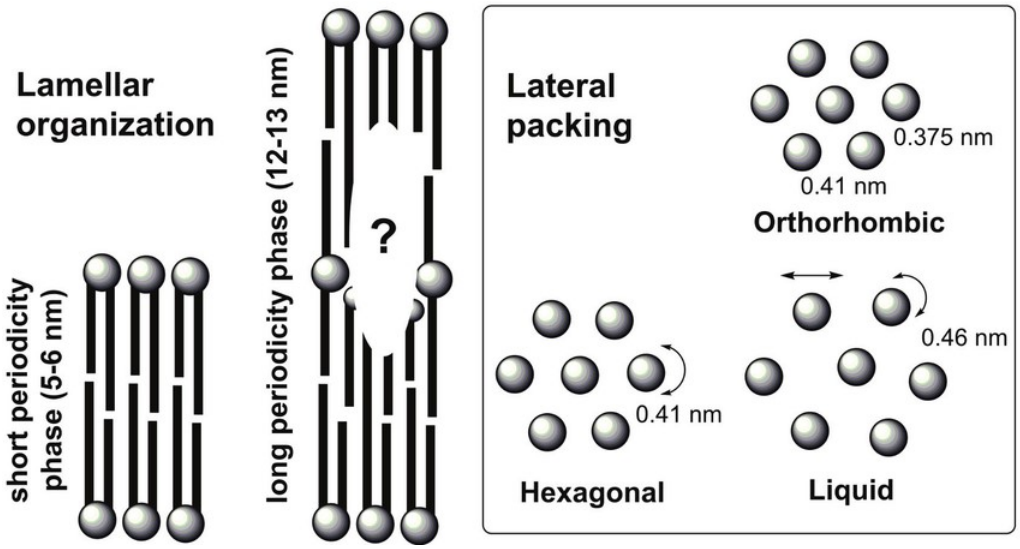

Figure 1.6: The lamellar organisation can coexist in a short periodicity phase (SPP) or in a long periodicity phase (LPP). The lateral organisation of the multiple lamellae is categorized as orthorombic crystalline, hexagonal gel, and liquid lamellar, depending on temperature. Figure has been reproduced from Vavrova *et al.*[3] with permission from De Gruyter.

Based on these experiments a number of models have been proposed of SC lipid organisation of the lipid lamellar layers. One such model is that of the domain mosaic model[4] shown in Figure 1.7. It is represented by crystalline lipids surrounded by fluid regions (grain boundaries). These grain boundaries allow for transepidermal water loss, yet the structure maintains the high barrier properties associated with the SC.

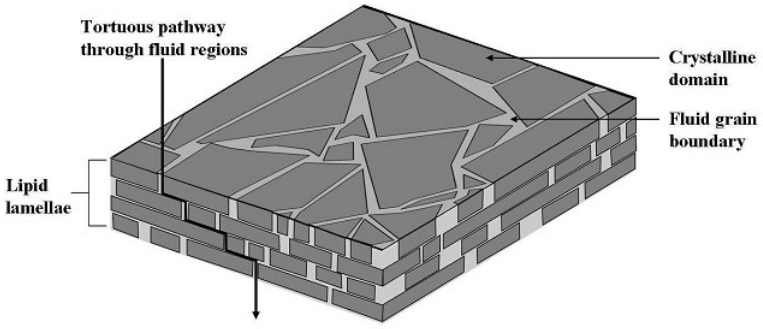

Figure 1.7: The domain mosaic model of the SC lipid lamellae. Figure has been reproduced from Forslind[4] with permission from the Society for the Publication of Acta Dermato-Venereologica.

Another model that explains the coexistence of crystalline and liquid phase lipids in the SC[24,25] is the sandwich model. This model is characterised by a trilayer lipid arrangement where crystalline layers sandwich a liquid layer that is rich in CHOL and unsaturated linoleic acid , see Figure 1.8, first suggested by Bouwstra *et al.*[5]. The two coexisting phases are characterised by repeat distances of 6 nm, the short-periodicity

phase, and 13 nm, the long periodicity phase, which have been seen in X-ray diffraction studies of pig, mouse and human SC[19,24,26].

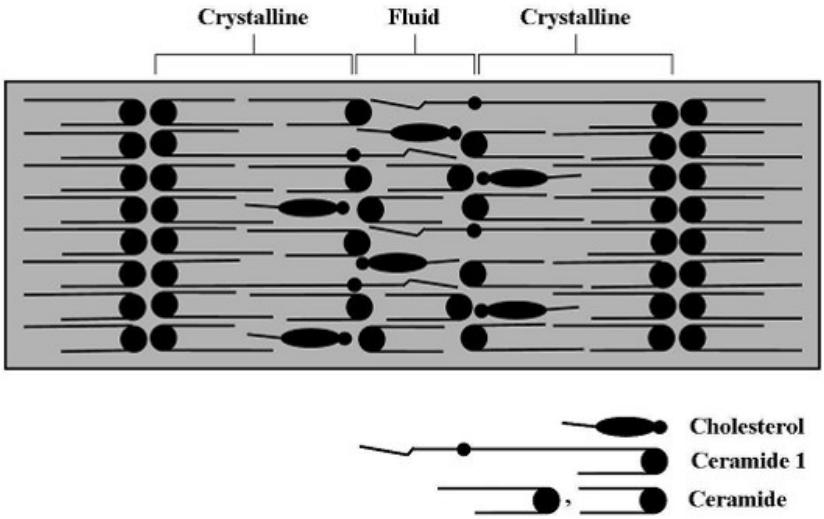

Figure 1.8: Sandwich model to describe the SC lipid organisation. Figure has been reproduced from Bouwstra[5] with permission from the Society for the Publication of Acta Dermato-Venereologica.

A single gel phase model, where the SC lipid lamellae can act as a single phase of packed lipid constituents can also be argued. In this model there are no energetically unstable phase boundaries that allow for greater permeability, just a macroscopic phase. Norlen and colleagues through the use of cryo-electron microscopy of vitreous skin section (CEMOVIS) experiments show that a possible lipid arrangement could form via stacked fully-extended CERs with CHOL associated with the CER sphingoid moiety. This model by Norlen[27] attempts to rationalise the skins low permeability towards water, as well as its robustness to various types of stress.

We can already see that as there are multiple models given to describe the lamellar layers of the skin lipids. As a result there is a lack of consensus of which model accurately depicts the top layer of the skin. Add to that the complex heterogenic nature of the lipid mixture, one can see why the SC remains poorly understood at the molecular level.

1.2.8 Review of Molecular Simulations of Skin Lipids

An alternative tool to try and help understand the SC is molecular dynamics (MD) computer simulation. This technique allows us to probe the SC at atomic resolution and gives us a detailed picture of the interactions at the molecular level and how they contribute to the skins barrier properties. The most common way of doing this is to use a CER model, it is the abundent component of the lipid matrix. The first simulation to use CERs to model the skin was by Pandit and Scott[28]. They carried out a

MD simulation of a hydrated 16:0 CER lipid bilayer at 368 K in the liquid-crystalline phase and compared the properties to an earlier simulation of 18:0 sphingomylelin and experimental data. They showed that the CER bilayer has significantly altered intermolecular hydrogen bonding compared to the simulated SM and there was a lack of electron density peaks compared to what you see for phospho- or sphingo-lipids. They concluded that as the CERs are absent of headgroups, the ordering behaviour of the water molecules at the lipid-water interface is significantly reduced, although the number of water molecules remains unchanged, primarily due to the hydrophobic nature of the interface. Essentially this paper provided a starting benchmark for further simulations of CERs in combination with other lipids in bilayers it should be noted, however that this study was not in the physiological relevant gel phase. Another excellent model used to represent the SC was that by Notman *et al*[29]. They used a single component bilayer of CER2, as it was believed to give the structural and dynamical properties that are generic to skin lipids. The model showed changes in phase at increasing temperatures; a gel phase structure at 283 K and 323 K, and a liquid-crystalline phase appearing at 363 K. These observations are consistent with experimental techniques that show a hexagonal gel structure below 360 K and a fluid structure at higher temperatures[15,30]. The tails were also hexagonally packed and the head groups were disordered at all temperatures simulated. The mismatch in the length of the hydrocarbon tails results in a region in the centre of the bilayer where the packing of the lipids is almost characteristic of the liquid-crystalline phase rather than the gel phase. The area per lipid for the gel phase model at 323 K was 0.374 nm^2 which was close to the experimentally known value of 0.378 nm^2[31]. Another important structural property is the narrow interfacial width ($\sim$0.4-0.6 nm) indicating that almost no water penetrates the bilayer, which is consistent with the accepted view that CERs are the component of the SC which governs the low permeability of water across it. The high barrier properties of this model are attributed to the lateral hydrogen bonding network between CER headgroups[32]. These CER bilayers have a higher area-compressibility modulus than phospholipid bilayers of the same phase. This high modulus is again attributed to the strong lateral hydrogen bonding between adjacent CER head groups.

The work by Das and his colleagues[8] showed the effects of both CHOL and FFAs on bilayer mixtures by simulating various molar ratios of the standard three components. Just like other simulation studies of skin-lipids, structural properties such as bilayer thickness, area compressibility and tail-order parameters were analysed. The authors note that the anisotropic arrangement of lipid molecules in a bilayer leads to an anisotropic local pressure profile, and hence local stress variations. The long asymmetric tails of the CERs formed a dense bilayer phase, with major interdigitation of the tails. With increasing temperature, the disordered region at the bilayer mid plane gradually thickens. FFAs increase the bilayer thickness and reduces its density across the bilayer in comparison to the pure CER bilayer, while CHOL reduces the thickness and increases the tail density, from the under the headgroup to the midplane, due

to the fact that its smaller and more rigid than the CER molecules. The presence of CHOL reduced the nematic order (lined in a specific direction with no positional sense), whereas FFA increases the order.

Further mixtures with FFAs and CHOL were investigated by Holtje *et al.*[33]. Two different models containing FFAs, with and without CHOL were modelled. Model A was used to investigate the behaviour of hydrated FFAs on bilayer properties while model B looked at the influence of CHOL on these properties. As there are no experimental data detailing an ideal distribution of CHOL molecules in skin lipids, the choice of random CHOL distribution was only one of various possibilities. At skin temperature the FFA fraction stayed in a highly ordered state crystalline state, but the phase behaviour was strongly influenced upon the addition of CHOL. It was seen that CHOL smoothes the rigid phases of the fatty acids by reducing the order of the hydrocarbon tails leading to a thickening of the hydrophobic thickness. As a result the area per molecule becomes larger. The simulations were in good agreement with the experimental data they obtained from FTIR analysis and NIR-FT Raman spectroscopy.

As of recently, modellers were limited to a handful of forcefields to accurately model skin lipids. Those such as CHARMM and Berger[34] are the most commonly used. The two of these along with OPLS, GROMOS and GAFF forcefields were compared by Papadimitriou[35] using MD simulations of CER NS. Typical bilayer properties were calculated and compared. It was concluded that although there is some discrepancy with intramolecular hydrogen bonding, a lack of experimental data prohibits a clear finding. The group of McCabe have added to this list by developing a coarse-grained model of CER NS[36]. They used multistate iterative Boltzmann inversion to derive the pair potentials, allowing the forcefield to be applicable over a range of state points. Their model is able to capture the directional nature of hydrogen bonding and gives accurate structural properties of CER bilayers. Another CG forcefield has also been developed by Sovova[9] to observe a pooling effect of low hydration on CER NS bilayers. A CG model can simulate times much longer than all-atom forcefields, such as CHARMM, due to the reduced number of particle interactions, smoother energy landscape and the ability to use a larger timestep; this comes at a cost of not capturing the specific chemistry. A united-atom forcefield such as Berger can occupy the middle ground, being atomistic but combining the alkyl hydrogens into the chain allowing it to be a cheaper solution.

The fact that skin lipids are in the gel phase when we simulate them poses certain challenges. These type of systems are viscous and thus cannot be fully equilibrated in an MD simulation. This means that the starting configuration will have a direct impact on the end configuration, as there is slow lateral diffusion, and thus the results. It is paramount that an appropriate starting configuration is used, but as there is a lack of consensus on the organisation of the lipids, it is challenging to determine if the

lipids are in their preferred arrangement or the simulation is stuck in a local energy minimum. Therefore, there is need to develop methodologies to enable simulation of the gel phase to converge to the low free energy structure.

1.3 Skin Permeation

1.3.1 Overview

There are a number of challenges within the pharmaceutical industry, none more so than the delivery of drugs to a target site. With the inclusion of high-throughput screening and rational drug design in the industry, drug discovery has progressed but bringing a new drug through to market is ultimately inhibited by the effectiveness of its delivery. One option is to deliver drugs is through the skin. Transdermal drug delivery can have many advantages compared to the standard oral approach. A transdermal route has reduced variability, can be easier to administer and the delivery process can be stopped if required. The major flaw with this route is that the skin acts as a barrier, with low permeability for drug molecules and even here there are a number of routes that can be taken to transverse the barrier. Nevertheless, there are a number of pathways by which some drug molecules permeates skin. One way is via a transappendageal route, i.e through a hair follicle. Other routes are transepidermal, either transcellular or intercellular described in Figure 1.9. Transmission electron microscopy studies of the diffusion of HgCl through human SC showed that penetration occurs mainly intercellularly[37], which indicates that the intercellular lipid domains of the SC give the main barrier for diffusion of substances.

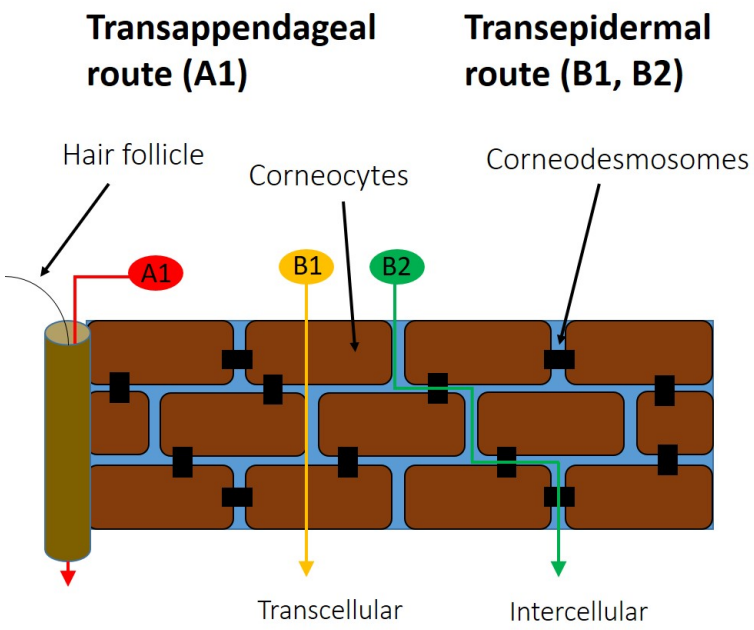

Figure 1.9: Routes across the skin. Figure has been adapted from Hadgraft and Lane[6] with permission from the Royal Society of Chemistry.

1.3.2 Theory of Skin Permeation

For molecules to pass through the skin they have to diffuse through the SC, viable epidermis layers and the upper layers of the dermis to get into the microcirculation. The SC provides the greatest resistance to the diffusion of these molecules through the skin.

The diffusion of molecules through the skin can be described by Fick's Laws of Diffusion.At steady state permeation, the flux, defined as the mass of permeant M passing through the membrane over a fixed unit area in time t, is given as

$$\frac{dM}{dt} = \frac{DC_0}{h} \tag{1.1}$$

where D is the diffusion constant of the permeant, C_0 is the concentration of the permeant in the first layer of the membrane and h is the bilayer thickness. It is difficult to measure C_0, but the concentration of the permeant in the donor solution C_d is usually known. These two concentrations are related by

$$P = \frac{C_0}{C_d} \tag{1.2}$$

where K is the partition coefficient of the permeant between the membrane and the donor solution. Substitution of Equation 1.2 and Equation 1.1 gives

$$\frac{dM}{dt} = \frac{DKC_d}{h} \tag{1.3}$$

As most of these quantities are difficult to measure in the skin, the permeability coef-

ficient k_p is often used. It is defined as

$$k_p = \frac{KD}{h} \tag{1.4}$$

The rate of permeation now becomes

$$\frac{dM}{dt} = k_p C_d \tag{1.5}$$

These equations demonstrate the key quantities that determine the rate of permeation, and which may be targets for altering the permeation of molecules across the skin.

When we get down to the molecular level a bulk kinetic model becomes inappropriate. This is due to the fact that we can't identify the regions of the membrane where partitioning and diffusion takes place. To remedy this we have to think of a permeant molecule transversing across a large number of infinitesimally-thin barriers aligned in a series. This can be characterised by the excess chemical potential $\mu(z)$ and the diffusion coefficient $D(z)$, of the permeant as a function of the cross sectional coordinate z across the membrane.

Therefore, for a molecular membrane, the total resistance that the permeant molecules encounters is calculated by the sum of all its local resistances:

$$R = \int_0^h \frac{dz}{K(z)D(z)} \tag{1.6}$$

The partition coefficient can be obtained from the excess chemical potential of the permeant molecule relative to when it is in bulk water from Equation 1.7:

$$K(z) = \frac{exp(-\Delta\mu(z)}{k_B T} \tag{1.7}$$

where k_B is the Boltzmann constant and T the temperature. The permeability K_p of the membrane can be described as the inverse of the resistance R. It is important to note that permeation can also occur in the plane of the lamellar layers not just in the perpendicular direction.

Another major limitation of simulating permeation of molecules across membranes, is that in a brute force simulation it is very unlikely that the permeation event will occur in the accessible timescale of microseconds. Take for example a small drug molecule of caffeine, which has an experimental permeability in human skin in the order of 10^{-4} cm h^{-1} [38,39], simulation of this timescale is virtually impossible. Again, we have to modify our methodology to circumvent this problem. It is possible to use a thermodynamic approach, the Potential of Mean Constraint Force (PMCF), see Section 2.6.2, where we focus on calculating the excess chemical potential of the permeant $\mu(z)$ across the membrane. The permeant molecule is constrained at fixed points along the z coordinate, free to move in the lateral directions, and during sampling collect the excess chemical

potential and the local diffusion coefficients. From these one can then calculate the permeability.

1.3.3 Experimental Measurements of Skin Permeation

The standard technique for measuring in vitro dermal absorption is to apply the test formulation to a sample of skin, which is pinned between the donor and receptor departments of a Franz diffusion cell[40].The formulation is situated on top of the skin sample with the receptor fluid in contact underneath. There are two different types of cell, the first is a static cell[40] which samples, and is replaced, with a new perfusate at every time point. This cell is typically horizontal, allowing the skin open to the air. The second, is a flow-through cell which uses a pump to pass perfusate through the receptor and is collected to obtain a flux. The diffusion cell should contain an inert non-adsorbing material and use multiple skin samples of area between 0.2 and 2.0 cm^2. The skin sample should be kept at in vivo skin temperatures of 32 $\pm$ 1 °C. The frequency of sampling should ensure that the rate of adsorption and absorption profile can be obtained.

1.3.4 Review of Molecular Simulations of Membrane Permeation

The use of potential of mean force calculations for calculating the permeability of small molecules was introduced by the work of Marrink *et al.*[41,42]. They calculated the excess chemical potential and diffusion coefficients at different locations across a 1,2-Dipalmitoyl-*sn*-glycero-3-phosphocholine (DPPC) bilayer for water, oxygen and ammonia, and thus were able to calculate their permeabilities. They were able to find the location of the main free energy barrier and determine its magnitude. For water, the barrier was seen in the lipid alkyl region and conversely for oxygen, the barrier was seen in the water layer due to its hydrophobic nature. The calculated permeabilities of these small molecules were in the same order of magnitude (10^{-1} cm s^{-1} for ammonia and 10^2 cm s^{-1} for oxygen) as experimental values. This was taken a stage further by Essex and colleagues as they studied a wider range of organic functional groups in a DPPC bilayer[43]. The calculated permeabilities resembled the experimental rank order but were a magnitude of order higher, this may be due to incomplete sampling of the permeation free energy surface. It was noted that the free energy barrier is what governs the largest change in the permeability. More small molecule permeation calculations have been done on the β-blockers alprenolol, atenolol and pindolol[44]. The authors correctly assigned the rank order for permeability but were a magnitude of order out in comparison to experimental values.

Even though simulations in the literature are mainly focused on studying permeation through phospholipid membranes we can still learn what factors may affect the permeation of molecules across a membrane, and apply that to skin lipid membranes. Das *et al.*[45] calculated the permeability of water in bilayers with varying ratios of CER, CHOL

and FFA. These structures include 1:0:0, 1:1:1 and 2:2:1 molar ratios at 350 K and an additional 2:2:1 structure at 300 K. It was determined that the permeability of water through the pure CER bilayer was 30 times lower than the experimental value of the SC while the permeability of the mixed bilayers was one order of magnitude higher than its corresponding pure version. More recently the effects of lipid phase and structure on permeation have been studied. Paloncyova and colleagues[46] analysed the interactions of p-aminobenzoic acid (PABA) and its esters with a DOPC bilayer in the fluid state and a CER2 bilayer in the gel phase using constraint MD simulations. They calculated the free energy profiles of all the molecules along the bilayer normal and showed that the profiles converged significantly slower for the gel phase system (∼100 ns for gel CER2 compared to ∼15 ns for fluid DOPC) and with a barrier height of three times higher. CER chain lengths can have a significant effect on permeation of water through the membrane, the permeability of water through bilayers of smaller-chain CERs was found to be an order of magnitude higher than that of its longer-chain counterparts[47]. The same authors also examined the permeation of a number of small molecules across tertiary membranes, with qualitative ranking in accordance with experiment, but a few magnitudes higher[48]. Possible reasons for this could be a inaccurate force field or improper sampling of phase space. It is important to note that only one reaction coordinate has been sampled, but in reality there are many that contribute to the overall permeability of the system and so this could explain the discrepancy of simulated and experimental values.

It has been suggested that error in potential of mean force calculations could come from a lack of sampling time for each point in the z coordinate. The lack of sampling is often because of the large number of independent simulations that the potential of mean force calculations require. As a result, the sampling time for each simulation will be restricted. A method to remedy this has been put forward by Essex and colleagues, where the lipids are represented by a coarse-grained (CG) model and the permeant at atomistic resolution, in what is know as dual resolution[49]. This methodology showed enhanced sampling of the order of two magnitudes but requires cross-interaction terms between the different resolutions.

1.4 Chemical Penetration Enhancers

1.4.1 Overview

Chemical penetration enhancers are substances that reversibly lower the barrier properties of the SC allowing drug molecules to permeate through the skin with less resistance. There are many known penetration enhancers for human SC available such as water, alcohols, unsaturated fatty acids, sulphoxides, pyrrolidones, surfactants, polyols and terpenes[50,51]. Although there is a plethora of options to choose from, most of them are currently unsuitable for pharmaceutical use due to high toxicity levels[52]. There is also

a lack of understanding at the molecular level of the mechanism of these chemicals. It is believed that there are at least three possible mechanisms; membrane fluidisation, phase separation, and lipid extraction[50], as shown in Figure 1.10. These mechanisms will be explained in more detail in the following sections.

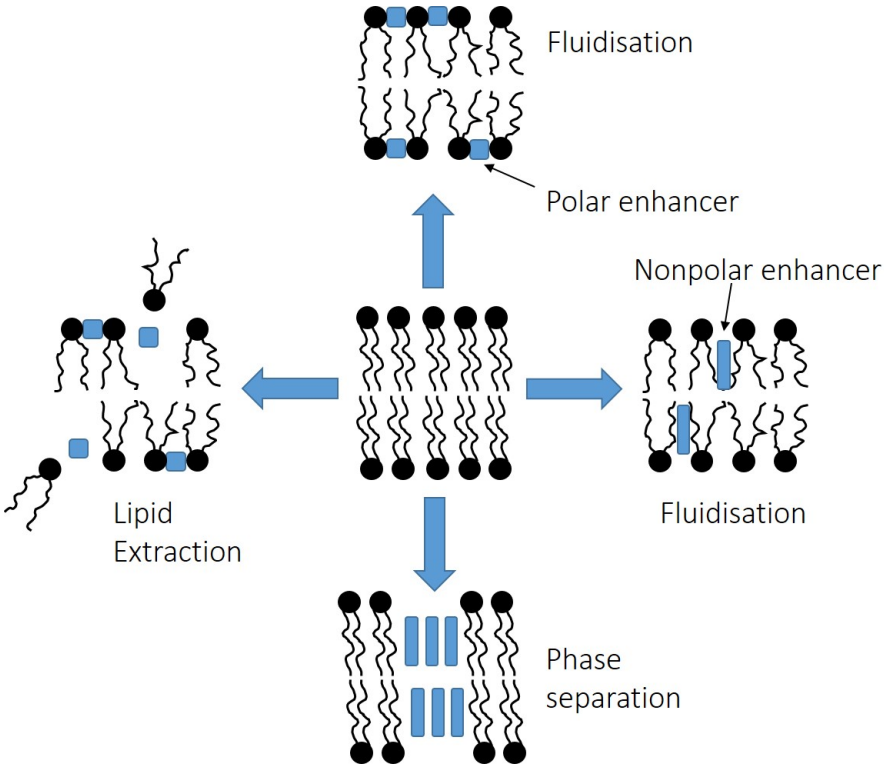

Figure 1.10: Mechanism of action of drug penetration enhancer molecules. Figure has been adapted from Barry[7] with permission from Springer Nature Journal.

1.4.2 Oleic Acid

The unsaturated free fatty acid OA (cis-octadec-9-enoic acid) is often used as a penetration enhancer for drug delivery through the skin[51,53–56]. It also has known therapeutic properties and can be used in inhalers[57] and can help in the reduction of cardiovascular disease and tumours[58–62]. It is believed that OA disrupts the packing of the skin lipids because of the "kinked" nature of the molecule due to its unsaturated bond. The molecular structure for OA can be seen in Figure 1.11.

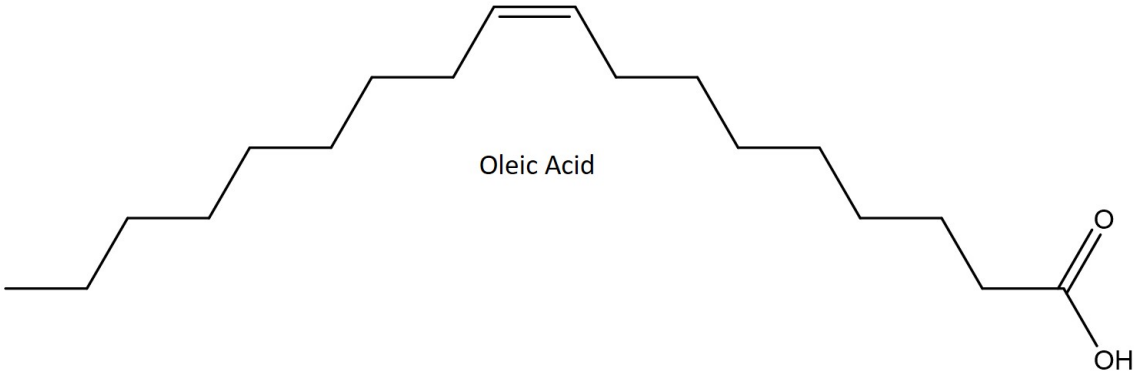

Figure 1.11: Molecular structure of OA.

The effects of OA on phospholipid membranes has been studied on many occasions. OA has been shown to have a small fluidizing effect on DPPC bilayers by decreasing the gel-to-liquid crystalline phase transition temperature by a couple of degrees[57,63]. Other experiments on DPPC bilayers show that OA disturbs the packing of the acyl chains[64] and there is evidence of phase separation at high surface pressures in DPPC liposomes[65]. Phase separation has also been observed in gel phase DPPC at high concentrations of OA[63] yet not for the fluid phase.

Interactions of OA may of course be different in the SC than in phospholipid bilayers due to the chemistry of the lipids and their resulting phase behaviour. As a result there has been an increase in the number of studies investigating the effects of OA on SC lipid models to develop therapeutic uses in industry. It is known that OA lowers the gel-to-liquid crystalline phase transition temperature of human SC[51,54,66] and below this temperature OA exists as a separate phase. Reduction of this transition temperature leads to an increase in permeation, as seen in experiments on porcine skin[67], which is facilitated by the kinked structure of OA and its disruption of lipid packing as previously mentioned.

It has been hypothesised that a possible mechanism for the enhanced penetration of small molecules is that OA fluidizes the membrane. Introduction of OA into the membrane disrupts the packing and thus inducing interdigitation causing a reduction in the bilayer thickness. Any defects at the interface through the OA could result in a weakening of the barrier to penetration[67,68]. Alternatively if phase separation does occur, permeants could directly diffuse through this OA layer. Despite the growing literature in this area, these hypotheses for the mechanism in which OA enhances penetration have not been fully examined. Therefore, in Chapter 4 of this study we analyse the various possible pathways in which small molecules, such as water, can permeate through model membranes of SC lipids with the aid of OA and deduce which pathway is most likely through the use of PMCF calculations. As a result we elucidate the mechanism of action of OA for enhanced penetration through structural analysis.

1.4.3 Dimethylsulfoxide

DMSO is another well studied penetration enhancer for hydrophilic and hydrophobic permeants[69,70]. It can be used as a cryoprotectant where it can prevent intracellular ice nucleation. It is an amphiphilic molecule that has a hydrophilic sulfoxide group and two methyl groups which are hydrophobic in nature. The effects of DMSO are known to be concentration dependent, with a concentration of 60% DMSO leading to effective penetration in human SC in many studies[50,69,70].

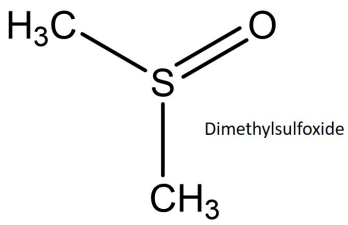

Figure 1.12: Molecular structure of DMSO.

There have also been many studies trying to determine the mechanism of action of DMSO. It has been proposed that DMSO promotes lipid fluidity by disrupting the order of the chains. DSC experiments on human skin show that DMSO lowers the temperature of the two phase transitions that are associated with lipid chain melting[51]. Fourier Transform Raman Spectroscopy on DMSO-treated skin showed that DMSO disorders the lipid chains at high concentrations[70].

The amphiphilic nature of DMSO can cause it to act as a spacer between lipid headgroups, leading to structural defects which can expand into pores that allow water to enter. This results in DMSO enhancing the permeability of hydrophilic molecules and ions by producing water pores, which could serve as channels to pass through. Pores only form at high concentrations and a large change in permeability has been observed experimentally[71], these pores have also been seen in simulation within phospholipid membranes[72–74] at are discussed in detail in Section 5.1. DMSO-induced water pores can also serve as pathways for lipid exchange across leaflets. These flip-flops could be problematic if something like phosphatidylserine was transferred, as it functions as a signal for apoptosis. This phenomenon could explain DMSOs toxicity to cells[71]. DMSO has a similar effect on SC lipids and due to being a HB acceptor, it can disrupt the lateral hydrogen bonding network of the SC. It has been observed to induce a gel-to-liquid crystalline phase transition in CER bilayers, where DMSO fluidizes SC lipids at high concentrations[51,70]. At these high levels of concentrations ($\geq$ 0.26 mol fraction) DMSO significantly effects the SC lipids[50,69,70].

1.4.4 Review of Molecular Simulations of Chemical Penetration Enhancers

There are now many more simulation studies observing the effects of penetration enhancers on membranes. In regard to these mechanisms, there have been numerous studies on DMSO, ethanol and OA.

Initial studies of the effect of increasing concentration of DMSO on DPPC bilayers using a coarse-grained model were first done by Notman *et al.*[72] It was seen that the DMSO molecules partition into the bilayer just beneath the head groups acting as spacer molecules between lipid head groups. This causes many structural changes such as an expansion in lateral area thus leading to a reduction in the bilayer thickness. This spacer action also changes the mechanical nature of the membrane; the increase in headgroup area per lipid causes an increase in the volume that the lipid tails can expand into thus reducing the tail density. These combined effects essentially make the membrane more affable to bending. This is evident through the decrease in the area compressibility modulus κ from 330 $\pm$ 20 mN/m for the pure DPPC system to 90 $\pm$ 10 mN/m for the 12% DMSO system and the significant increase in bending modulus κ. During one of the simulations (27% DMSO after 240 ns) there was a very rare occurrence of a water pore. The formation of this pore is believed to be caused by lipids getting deeper into the bilayer allowing access to a small amount of water and DMSO molecules this in turn facilitating the entry of greater number of water until an hourglass pore was formed. The authors compare this with experiments showing permeability enhancement effects of DMSO at concentrations greater than 26 mol %, also exactly replicated by the simulation results here.

These ideas were examined further by Gurtovenko and Anwar[73] using atomistic scale MD simulations. They used 14 different concentrations of DMSO with respect to water to infer three distinct modes of action for the permeation enhancing effects of DMSO. At low concentrations the DMSO molecules again act as spacer molecules, partitioning just below the head groups of the lipids levering them apart, reducing the membrane thickness and allowing the tails to become more disordered and fluid. At medium concentrations water pores are formed as was seen by Notman *et al.*[72] A further increase in DMSO concentration leads to desorption of lipids from the membrane and thus leads to rupturing of the bilayer. From this information of the various modes of action of DMSO it should now be possible to tune the DMSO concentration to a specific application, whether it be increasing permeability of hydrophilic molecules or acting as a cryoprotectant. This may be useful for penetrating phospholipid bilayer systems, but we must be wary of the downfalls of using high concentrations, the exchange of lipid molecules between one leaflet and another is probable if there are DMSO-induced water pores in the membrane, in some instances this can even lead to apoptosis[75].

Although previous simulation studies have proved invaluable in recognising and under-

standing the various mechanisms that DMSO employs in increasing the permeability of membranes, the work was mainly focused on phospholipids. If we want to improve transdermal drug permeation we have to investigate model systems that represent the skin such as those presented earlier in this chapter. Investigating the interactions of DMSO with the most prominent CER in the skin (CER2) as a pure bilayer, Notman *et al.*[29] were able to show results for a more realistic system. The effect of DMSO over the range 0.0-0.6 mol fraction DMSO was investigated. Again DMSO molecules were observed to accumulate at the head groups, where, unlike in phospholipid bilayers they weaken the lateral hydrogen bonding between the CERs. At concentrations of 0.4 mol or higher the CER bilayers underwent a phase transition from a gel to a liquid crystalline phase, which is characterised by the highly disordered tails and a decrease in the bilayer thickness, suggesting a higher degree of interdigitation. This fluidising effect of DMSO on SC lipids has also been seen experimentally[51,70] and its enhanced permeation effect has been seen in concentrations above 26% mol fraction[69,70]. The liquid-crystalline phase is expected to be more permeable to solutes than the gel phase, this is due to the disorder of the tail groups. The liquid-crystalline phase is also expected to enable a higher rate of diffusion and a lower free-energy barrier to the permeating molecule.

As was mentioned earlier on, small to medium chain alcohols such as ethanol are also known to be good penetration enhancers. An atomistic MD study on the effect of ethanol on 1-Palmitoyl-2-oleoyl-*sn*-glycero-3-phosphoethanolamine (POPE) and 1-Palmitoyl-2-oleoyl-*sn*-glycero-3-phosphocholine (POPC)[76] bilayers is well known in the literature. It was observed that ethanol acted in a similar way to DMSO in that it would partition itself underneath the headgroups of the phospholipids at low concentrations. But unlike DMSO these ethanol molecules don't just act as spacers but form their own HBs with the head groups. At higher concentrations, ethanol induced inverted micelles into the bilayer, containing small amounts of water trapped inside. It could be possible for these to act as delivery pockets, transporting polar molecules or ions from one leaflet to another within the membrane structure. No pores were induced as was seen with high concentrations of DMSO.

Similar studies have been applied to the effective penetration enhancer, OA[51,53]. This molecule can enhance delivery of drugs topically to the skin or transdermally via the skin. At physiological temperatures OA is believed to exist in a separate phase within the SC[63,77]. Originally it was believed that OA achieves its enhanced permeating ability through its kinked structure, due to its unsaturated bond, disrupting the packing of the skin lipids. Of course this hypothesis needed to be tested on some model systems. First of all we have a brief look at CG simulations on DPPC bilayers[78]. The concentration of OA was increased from 0 to 1 mol fraction with respect to the total lipid content. Hardly any structural changes were seen, the only change in property of note was the reduction of the compressibility modulus. It was not until chemical potential

calculations were run that it was understood that this original hypothesis did not hold for this model system. The calculations revealed a small increase in the permeability of the bilayers to water. The physiological effects of OA are more subtle than just a large perturbation of the structure.

OA seems to have relatively small structural effects on phospholipid bilayers, but again it is necessary to study its effects on more suitable models related to the SC. A lipid bilayer containing a 1:1:1 mixture of CER2, CHOL and lignoceric acid in water was ran using atomistic MD[79]. The concentration of OA was kept between 0 and 0.1 mol % and two different temperatures of 300 and 340 K were trialled. At the latter temperature, the diffusion of CHOL is enhanced as the concentration of OA is increased. There are minor structural changes that can be ascertained such as the reduction of the densities in the bilayer midplane and at the interface leading to an overall reduction in the bilayer thickness. It was also seen that the extent of hydrogen bonding didn't change with variation in OA. However, it was found that OA molecules are not able to line properly with the CERs due to the unsaturated bond they contain, as a result the half of the tail projects laterally away from the bilayer normal. This suggests that any changes made to the bilayer structure through the addition of OA is caused by the change in configuration at the interface.

Hoopes *et al.*[79] studies these structural effects by modelling mixtures of CER NS, lignoceric acid, CHOL with varying concentrations of OA at 300 and 340 K. Upon addition of OA, both the interfacial and midplane densities, the thickness in the hydrophilic interface at 300 K and the overall thickness at 340 K were reduced. This is due to the interdigitation that coincides with the temperature increase but happens regardless of the OA. OA did not have a significant impact on the hydrogen bonding of the CERs but introduced greater ordering of the non-hydroxyl fatty acid of the CER just below the headgroup. Dynamical properties such as the diffusion of CHOL can be seen to increase as a function of OA. These findings were enhanced most recently by Akinshina and colleagues[80] through their investigation of the effects of unsaturation of FFA tails using MD simulations of differing concentrations of natural fatty acids with CER NS bilayers. Mixed bilayers with saturated oils remained stable even with high oil concentrations. Low oil concentrations lead to rigid bilayers due to better packing and a transfer of HBs from lipid-water to lipid-lipid. Oils with unsaturation, such as OA, lead to instability of the bilayer structure at concentrations greater than 50%. The concentration required for this breakdown decreases as the number of *cis*-double bonds increase. With instability in the bilayer comes greater permeability.

It was observed by Peters *et al.* that OA and its analogues alter their positions in fluid 1,2-Dimyristoyl-*sn*-glycero-3-phosphocholine (DMPC) bilayers depending on their protonation status[81] and thus may have an effect on the structure. These structural effects are attributed to the kinked structure found in cis-OA *via* an unsaturated double bond.

To explore the effects of saturation Leekumjorn *et al.*[82] used MD simulations of saturated and unsaturated fatty acids, including OA, within fluid DOPC. It was shown that that the unsaturated fatty acids are able to reduce the lipid ordering within the membrane and thus increase its fluidity. In contrast, the saturated fatty acids promoted a closer packing of the bilayer tails.

1.5 Aims and Objectives of the Study

This study aims to explore the behaviour of model bilayers of the SC lipids under a variety of conditions and their interactions with penetration enhancers using molecular dynamics simulation. This is achieved by investigations of hydration, finite size and solvent effects, and the penetration enhancer OA on CER NS bilayers.

In Chapter 3, MD simulations of CER bilayers with varying hydration levels are presented. The purpose of this study was to investigate the concentration-dependent effects of hydration on a multi-layered CER bilayer, that have not been explored in previous atomistic simulations. It is found that the water content within the lipid matrix has a direct impact on the bilayer conformation and thus the barrier properties of the SC. At low hydration a pooling effect is observed on the bilayer surface, which affects the order and orientation of the CERs, leading to structural changes in the bilayer.

Chapter 4 presents the effect of OA on the free energy barrier to penetration in CER bilayers and compares with pure CER and OA bilayers. The effects of OA on the structural properties are shown. In addition, permeation coefficients of each system are calculated. The objective of this study is to characterise the effect of OA, acting as a penetration enhancer, on the permeation of the systems, thus predicting favourable pathways through the SC and discussing the mechanism of action. It is found that OA acts as a penetration enhancer by disrupting the lateral hydrogen bonding network of the CERs leading to an increase in permeability of the bilayer. A mixed CER/OA section would be the most favourable pathway for permeates, such as water, to migrate through these membranes. In a phase separated system, an OA pool would also be a more favourable pathway, than a pure CER area.

In Chapter 5, coarse-grained (CG) simulations of the interaction of DMSO, with varying solvent to lipid ratios, and CER bilayers of various sizes are presented. The aim of this study was to test the solvent and finite size effects for a penetration enhancer on CER bilayers. Periodic artifacts are observed at low solvent concentrations at larger bilayer sizes. Size effects are prominent as the surface area is increased, despite the same solvent to lipid ratio, greater amounts of DMSO accumulate at the interface enhancing the fluidization of the membrane and increased permeation.

Chapter 6 reviews the results of the studies and draws conclusions about the conditions

of a good model system when performing molecular dynamics simulations on CER bilayers. Conclusions about the mechanisms of action of chemical penetration enhancer molecules are also discussed. Areas for future investigation are suggested.

Chapter 2

Computational Methodology

2.1 Statistical Mechanics

Statistical mechanics is the theoretical framework used to convert microscopic level information that we can generate from computer simulations, into macroscopic information. This macroscopic information can be defined through the thermodynamic state using properties such as the number of particles (N), temperature (T), and pressure (P), while other thermodynamic properties can be derived through the equations of state.

Phase space is a multidimensional space, which includes the positions and momenta of particles all the particles in the system. Therefore, this space has $6N$ dimensions, where N is the total number of atoms in the system. An observable macroscopic property, A, at a particular point in phase space Γ, will evolve over time. This can be written as a time average of $A(\Gamma)$ taken over a long time period.

$$A_{ave} = \lim_{\tau \to \infty} \frac{1}{\tau} \int_{t=0}^{\tau} A(\Gamma(t))dt \tag{2.1}$$

For large numbers of molecules the time evolution of $A(\Gamma(t))$ becomes rather complex. To help simplify this, we can replace the time average with an ensemble average, where the ensemble is just a collection of points Γ in phase space.

$$\langle A \rangle = \int \int d\mathbf{p}^N d\mathbf{r}^N A(\Gamma)\rho(\Gamma) \tag{2.2}$$

This collection is distributed according to a probability density $\rho(\Gamma)$, which shows the probability of finding a configuration with $\mathbf{p}^N$ momenta and $\mathbf{r}^N$ positions. As the ensemble average is equal to the time average, and with conditions of constant number of particles, volume and temperature, the probability density becomes the Boltzmann distribution.

$$\rho(\Gamma) = exp(-E(\Gamma)/k_B T)/Q \tag{2.3}$$

where $E(\Gamma)$ is the energy, k_B is Boltzmann 's constant, T is the temperature and Q is the partition function. The partition function is a normalising factor and allows for the calculation of other thermodynamic properties. The most commonly used ensemble is the canonical ensemble (NVT), where Q is defined as

$$Q_{NVT} = \frac{1}{N!}\frac{1}{h^{3N}}\int\int d\mathbf{p}^N d\mathbf{r}^N exp[\frac{-H(\Gamma)}{k_B T}] \tag{2.4}$$

where h is Plank's constant, the Hamiltonian, H, is the sum of the potential and kinetic energy and the $N!$ factor comes from indistinguishibility of the particles. Other ensembles that can be used are the micro-canonical (NVE), isothermal-isobaric (NPT) and the grand canonical ensemble (μVT).

Thermodynamic properties such as the internal energy, pressure and heat capacity are mechanical properties that are related to the derivative of the partition function, and thus can be calculated from MD simulations. While thermal properties, such as the free-energy, the chemical potential and entropy require special techniques to be calculated. The following equations can be used to calculate the internal energy E

$$E = k_B T^2 \frac{\delta \ln Q}{\delta T} \tag{2.5}$$

the Helmholtz free energy

$$F = -k_B T \ln Q \tag{2.6}$$

the Gibbs free energy G for a system with constant volume V

$$G = -k_B T \ln Q + k_B T V[\frac{\delta \ln Q}{\delta V}] \tag{2.7}$$

and the entropy S

$$S = -k_B T \frac{\delta \ln Q}{\delta T} + k_B T \ln Q. \tag{2.8}$$

2.2 Molecular Mechanics

2.2.1 Introduction

Molecular mechanics is a method to describe all the atomic interactions within system of atoms or molecules through the use of a functional form and a set of parameters defined via a forcefield. For a more 'exact' treatment of these interactions, quantum mechanical (QM) calculations can be performed but for larger systems, such as those in biological environments, a QM treatment would not be feasible. Molecular mechanics simplifies this problem be assuming the Born-Oppenheimer approximation that electronic and nuclear motion can be separated. By concentrating on the nuclear coordinates of the

particles and discarding the electrons one can reduce the complexity of the problem into a number of simple pairwise interactions that can be described by the stretching of bonds, opening and closing of angles and the rotation of bonds. By taking all of these contributions into account the energy of the system can be measured moderately well. The set of parameters that are used in the potential energy function are defined in a forcefield. These generally include a number of equilibrium values and force constants for the bond stretching, angle bending and torsion rotations. It is necessary in the forcefield to assign an atom type for each individual atom, for example an atom maybe assigned to a particular type due to its hybridisation state or the chemical nature of other atoms to which it is bonded.

One of the most important details of a forcefield is the transferability of the parameters to other molecules. It would become laborious if we needed a different set of parameters for every individual molecule. A positive of having transferability in a forcefield is that it allows a set of parameters to be tested on a small number of cases and then can be applied to a larger range of problems. On the other-hand, a set of more general parameters may not always capture the correct chemistry or physics of a specific molecule.

It's important to note that there are many different forcefields available for various types of molecule, or even the same molecule. They are usually derived from a combination of existing experimental data and QM calculations to make sure that they reproduce the existing structural properties of a set of target molecules. The functional form of a simple potential energy function is the sum of the bonded and non-bonded terms (Equation 2.9). Where the bonded terms include bonds, angle and torsions (Equation 2.10) and the non-bonded terms include Lennard-Jones (LJ) and Coulombic interactions (Equation 2.11).

$$U_{Tot} = \sum U_{bonded}(r) + \sum U_{non-bonded}(r) \tag{2.9}$$

$$U_{bonded} = U_{bonds} + U_{angles} + U_{torsions} \tag{2.10}$$

$$U_{non-bonded} = U_{LJ} + U_{coulomb} \tag{2.11}$$

2.2.2 Bond Stretching

The potential energy function as a function of the bond stretching can be derived using the analogy of two balls separated by a harmonic spring. Where r is the bond separation distance, $U(r)$, the potential energy as a function of the separation, can be expressed by taking a Taylor expansion about the bond length at the minimum r_{eq} when the function has a potential energy of zero.

$$U(r) = U(r_{eq}) + \frac{dU}{dr} \mid_{r=r_{eq}} (r - r_{eq}) + \frac{1}{2!}\frac{d^2U}{dr^2} \mid_{r=r_{eq}} + (r - r_{eq})^2 \frac{1}{3!}\frac{d^3U}{dr^3} \mid_{r=r_{eq}} (r - r_{eq})^3 + ... \tag{2.12}$$

By truncating after the first non-zero term we have a simple expression for the vibrational potential energy.

$$U_{bond}(r_{AB}) = \frac{1}{2}k(r_{AB} - r_{AB,eq})^2 \tag{2.13}$$

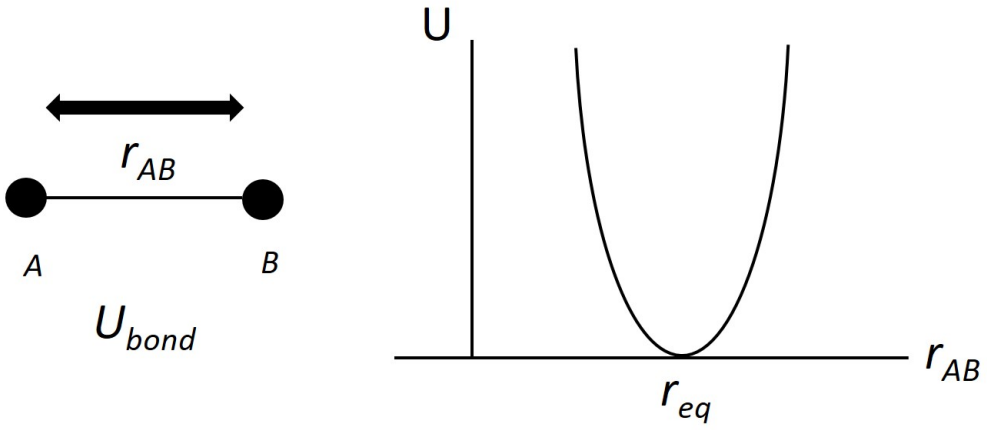

Figure 2.1: Bond energy term (U_{bond}) in the potential energy equation.

This functional form is fairly good at predicting these energy values compared with vibrational spectra but only near the reference bond length r_{eq}. At further bond stretches it becomes less accurate and at larger distortions in the bond length we predict the energy to become infinitely positive, which chemically doesn't make sense. The addition of more terms to our Taylor expansion should intuitively improve the accuracy of our forcefield but a negative form would lead to incorrect structures during energy minimisation and more equilibrium constants would be needed. An alternative functional form is the Morse potential (Equation 2.14). It has a larger range of r than other potentials but it's exponential function is computationally expensive.

$$U(r_{AB}) = D_{AB}[1 - \exp^{-\alpha_{AB}(r_{AB} - r_{AB,eq})}]^2 \tag{2.14}$$

2.2.3 Angle Bending

Another factor that affects the overall potential is the angle bending. The deviation of angles from their reference values can also be described using polynomial expressions, most commonly seen in the harmonic potential form as seen for the bond stretching (Equation 2.15). The accuracy of the force field can be improved by also using high order terms as seen in the bond stretching. For example the biomolecular force field by Cornell *et al.*[83] uses a quadratic expression while the MM3 organic forcefield uses a polynomial upto the sextic term[84]. This mechanical description does however have issues in describing linear bonds and bond angles that have multiple equilibrium values.

$$U_{angle}(\theta_{ABC}) = \frac{k}{2}(\theta_{ABC} - \theta_{ABC,eq})^2 \tag{2.15}$$

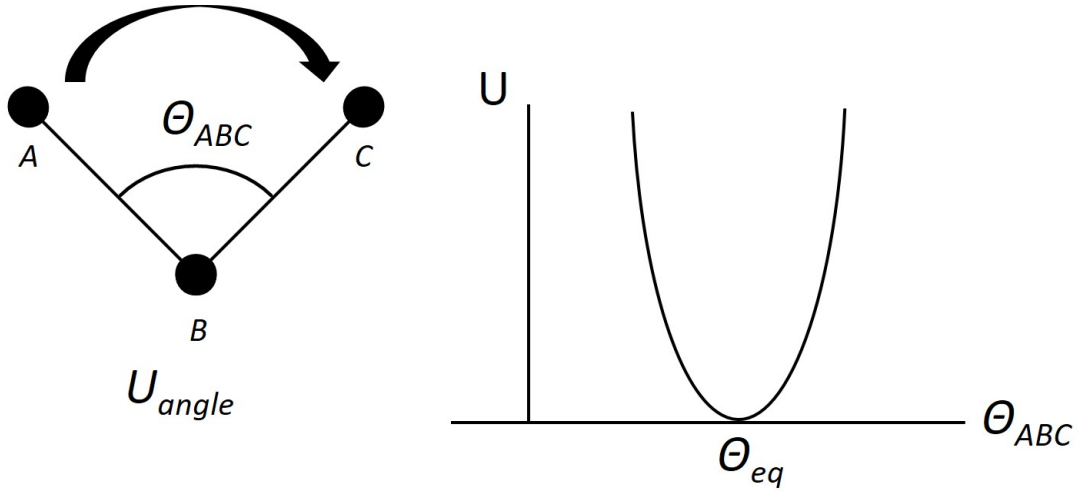

Figure 2.2: Angle energy term (U_{angle}) in the potential energy equation.

2.2.4 Torsion Angle Rotation

The torsional terms carry a large influence over the structure of molecules and thus by extension their energies. Therefore we need to accurately model this contribution to the potential. A torsion is defined as an angle between bonds AB and CD when they are projected into the plane bisecting the BC bond. Since the torsion angle is periodic in nature, a periodic function is needed to model the energy. Force fields for organic molecules use a cosine series expansion like the one in Equation 2.16. Where V_n is the amplitude as gives an indication of the barrier to rotation, n is the multiplicity, the number of minimum points in the function and γ, the phase factor determines the minimum value of the torsion. In the GROMOS forcefield used in this thesis, the torsional energy described by a torsional potential usually depends only on the atom types of the central bond and not those at the ends. Additional terms can be added and are associated with particular physical interactions such as differences in

electronegatively, hyperconjugation and unfavourable bond-bond eclipsing interactions, all of which are seen in a three term torsional potential of Fluromethanol[85].

$$U_{torsion}(\omega_{ABCD}) = \frac{1}{2} \sum_{(j)ABCD} V_{j,ABCD}[1 + (-1)^{j+1} \cos(j\omega_{ABCD} + \psi_{j,ABCD})] \quad (2.16)$$

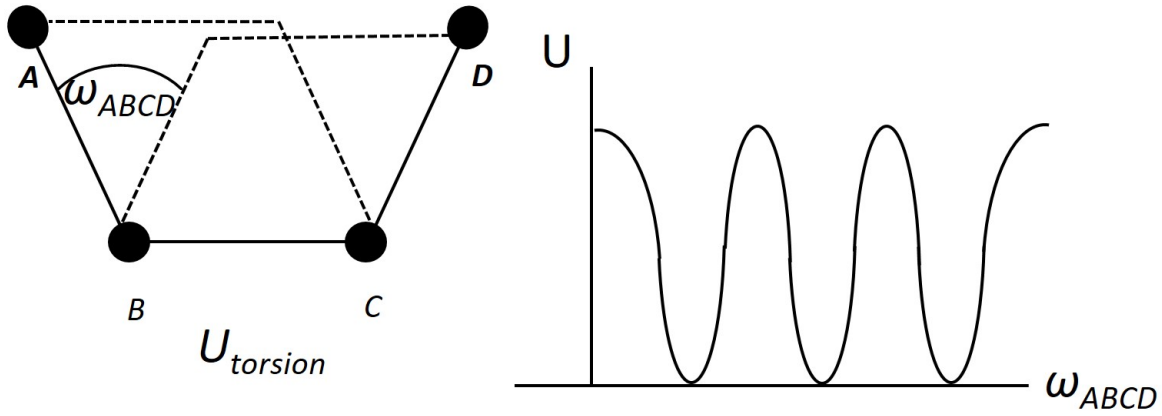

Figure 2.3: Torsion angle energy term ($U_{torsion}$) in the potential energy equation.

2.2.5 Out-of-plane Bending Motions

Molecules such as cyclobutanone would be incorrectly modelled using standard bond-stretching and angle-bending terms as in the previous equations. Experimentally, it is found that the oxygen atom is in the plane of the of the cyclobutane ring. To achieve this correct geometry we need to add additional terms to keep the sp^2 carbon and its bonded atoms in the same plane. The easiest way to achieve this is to use an out-of-plane bending term. This can be done by either the calculation of the angle θ between a bond from the central atom and the plane it lies in (Equation 2.17) or from the height h of the central atom above the plane defined by the other atoms (Equation 2.18). Both of these definitions can be modelled using a harmonic potential form.

$$U(\theta) = \frac{k}{2}\theta^2 \quad (2.17)$$

$$U(h) = \frac{k}{2}h^2 \quad (2.18)$$

2.2.6 Van der Waals Interactions

In molecular mechanics the dispersion and repulsive (Van der Waals) interactions between non-bonded atoms are modelled using the LJ potential (Equation 2.19, where σ is the interatomic separation distance when the energy is zero. The LJ potential has an attractive part that varies as r^{-6}, the leading term from theoretical treatments of the

dispersion energy such as the Drude model. The repulsive part of the potential varies as r^{-12} is used for calculations on large systems as the term can be easily calculated from r^{-6} and is less computationally expensive than an exponential form suggested by QM calculations.

$$U_{LJ}(r_{AB}) = 4\epsilon_{AB}\left((\frac{\sigma_{AB}}{r_{AB}})^{12} - (\frac{\sigma_{AB}}{r_{AB}})^{6}\right) \tag{2.19}$$

Setting $U = 0$ and differentiating with respect to r_{AB}, we obtain:

$$\frac{dU(r_{AB})}{dr_{AB}} = 4\epsilon_{AB}r_{AB}\left(-12(\frac{\sigma_{AB}}{r_{AB}})^{12} + 6(\frac{\sigma_{AB}}{r_{AB}})^{6}\right) \tag{2.20}$$

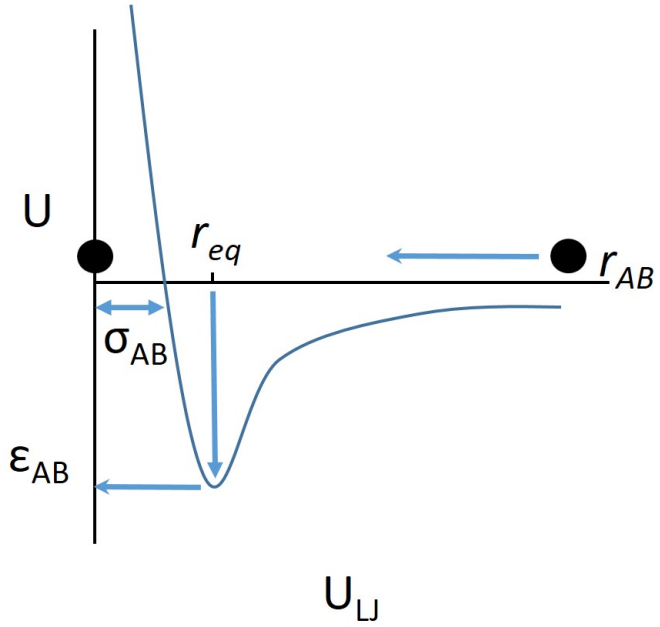

Figure 2.4: The LJ potential (U_{LJ}) showing the interatomic separation distance σ, the well depth ϵ and the equilibrium separation distance r_{eq}.

This can be rearranged to Equation 2.21, where r^* is the bond length at the minimum. By inserting this into the LJ equation we get $U = -\epsilon_{AB}$, showing that the parameter ϵ is the well depth. It is common for the LJ parameters to be set to 1 as thus simulations of noble gases can be done in terms of reduced units.

$$r^*_{AB} = 2^{1/6}\sigma_{AB} \tag{2.21}$$

The LJ equation is used in most forcefields although a more complicated functional can be used in a forcefield with fewer particles. An example of which is the Buckingham

potential (Equation 2.22), where a new parameter β is introduced. The Buckingham potential suffers from the problem of becoming steeply attractive at short range.

$$U(r_{AB}) = \epsilon_{AB}\left(\frac{6}{\beta_{AB}-6}\exp(\beta_{AB}\frac{1-r_{AB}}{r^*_{AB}}) - \frac{\beta_{AB}}{\beta_{AB}-6}(\frac{r^*_{AB}}{r_{AB}}^6)\right) \tag{2.22}$$

Polyatomic systems require the calculation of Van der Waals interactions between different types of atoms. To calculate the Van der Waals interaction energy between two molecules we need parameters for each atom-atom combination including the cross interactions (interactions between atoms of different type). Therefore a system containing N atom types would require $N(N-1)/2$ sets of parameters to describe these interactions. It is often assumed that any cross interactions can be derived from the parameters of pure atoms using a set of mixing rules. For atom types of similar properties the Lorentz-Berthelot mixing rules are used, where the collision diameter σ_{AB} is found using an arithmetic mean of the same species parameters (Equation 2.23) and the well depth calculated using the geometric mean (Equation 2.24). The main problem with these mixing rules is that the well depth is often overestimated by the geometric mean. Some forcefields, such as Jorgensen's OPLS[86], use the geometric mean for both the collision diameter and the well depth.

$$\sigma_{AB} = \left(\frac{\sigma_{AA}+\sigma_{BB}}{2}\right) \tag{2.23}$$

$$\epsilon_{AB} = (\epsilon_{AA}\epsilon_{BB})^{1/2} \tag{2.24}$$

2.2.7 Electrostatic Interactions

One also needs to model the charge distribution in a molecule to complete an accurate picture of the non-bonded interactions in a system. The most common way to capture the electrostatic properties of a molecule is through a fractional arrangement of point charges across the molecule. The electrostatic interaction between two molecules can then be calculated as a sum of the point charges using Coulomb's law (Equation 2.25).

$$U_{coul}(r_{AB}) = \sum_{i=1}^{N_A}\sum_{j=1}^{N_B}\frac{q_i q_j}{4\pi r_{ij}\epsilon_0} \tag{2.25}$$

Where N_A and N_B are the number of point charges on each of the two molecules, q_i

and q_j are the partial charges, ϵ_0 is the permittivity of free space and r_{ij} is the separation distance between the charges i and j. It is important to note that $U_{coul}(r_{AB})$ varies slowly as $1/r$ which has consequences for using this equation in practice in MD calculations, see Section 2.5.3.

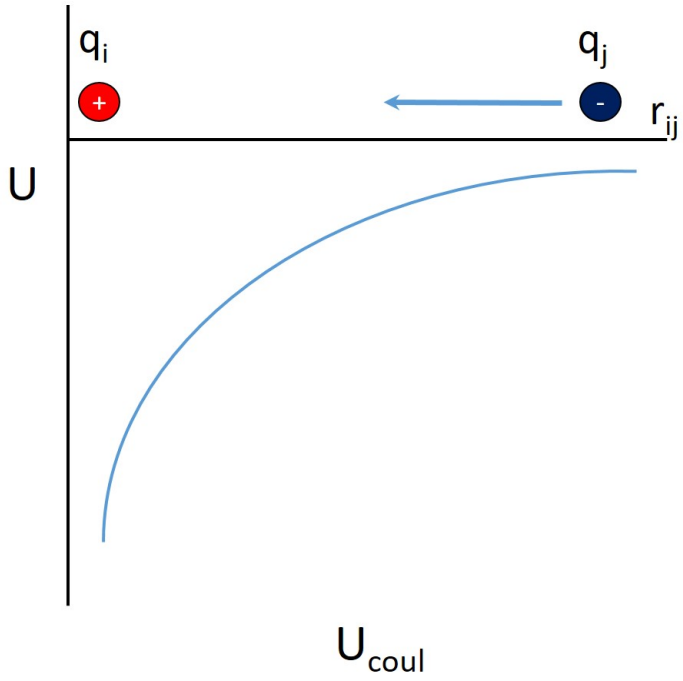

Figure 2.5: The Coulomb potential U_{coul} where q_i and q_j are the partial charges associated with atoms i and j respectively, and r_{ij} is the separation distance between the charges i and j.

2.2.8 Forcefields for Lipid Simulation

A forcefield to be accurate and reliable it must reproduce the structure, phase and behaviour of the lipids under different conditions such as temperature, hydration and compositional heterogeneity. The lipid forcefield must also be validated to ensure that it captures the specific properties and behaviour of the lipids on their own or in bulk. A number of validated force forcefields include AMBERLipid14[87], CHARMM36[88], GROMOS54A7[89] and Berger[34]. These forcefields are validated by comparing simulated properties with experimental values including scattering form factor, membrane thickness, area per lipid and lipid order, and the dynamical property lateral self-diffusion. In this work the potential energy function and interaction parameters employed for atomistic CERs are based on the united atom force of Berger.

2.2.9 Berger Lipid Forcefield

Berger *et al.* noted that the LJ parameters for the CH_n groups in the OPLS forcefield[86] could be responsible for the too low volume and high heat of vaporization in previous lipid simulations. To improve these parameters, they simulated a bilayer system of

pentadecane molecules, which aimed to represent the hydrophobic chains of the lipids, and adjusted the LJ parameters to yield the correct volume and heat of vaporization. Those parameters were then used to simulate a 64 DPPC bilayer using different headgroup charge frameworks and comparing the results of volume per lipid, atom pair distances and orientational order parameters of the lipid chains with other forcefields and experimental data.

The Berger lipid forcefield uses the standard parameters of the GROMOS forcefield all bonds, angles, improper dihedrals and headgroup dihedral angles. The Ryckaert-Bellemans potential[90] was used for the hydrocarbon chains. A united atom approach for the hydrocarbon CH_n groups is applied, where nonpolar hydrogen atoms are combined with the C atom to be represented as a single particle. This allows the simulations to be computationally cheaper as there is a reduction in the number of interactions to be calculated. The non-bonded interactions were computed from the LJ potential and Coulomb interactions, as described in Sections 2.2.6 and 2.2.7. The OPLS parameters[86] were used for the non-bonded interactions, while the united groups of the hydrocarbon chains were adjusted in accordance to their pentadecane simulations. Combining rules were used to get the mixed LJ parameters. The LJ contribution to the non-bonded 1,4 interaction was reduced by a factor of 8. This forcefield has been used in simulations of palmitoylsphingomyelin[91], which has a comparable molecular structure to that of CER NS except for a phosphatidylcholine headgroup. To adjust the forcefield, to accommodate for the CER NS headgroup, partial charges from palmitoylsphingomyelin, as acheived by Mombelli *et al.*[91], were partitioned into neutral charge groups across the CER headgroup, see Figure 2.6.

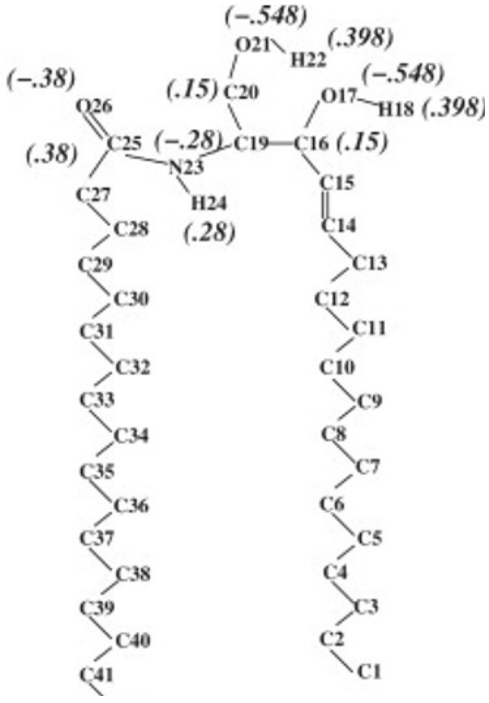

Figure 2.6: Partial charges for CER headgroup based on serine side chain. Figure has been reproduced from Das *et al.*[8] with permission from CellPress.

2.3 Energy Minimisation

2.3.1 Introduction

It is usually necessary to energy minimise the complex energy function to get a good starting geometry for MD simulations. Minimum energy arrangements of the atoms corresponds to stable states of the system. There are a number of energy minimisation algorithms that are based on the derivatives of the potential energy which include steepest descent, conjugate gradient, and Newton-Raphson minimisation. The steepest descent minimisation method was used for all energy minimisations in this thesis.

2.3.2 Steepest Descent Minimisation

The steepest descent minimisation method is a first order algorithm that gradually changes the coordinates of the atoms as the system is moved towards the minimum energy configuration. The starting point of each iteration is the configuration obtained from the previous iteration step. In the steepest descent, the first derivative of the potential energy, $\mathbf{g}$, is calculated and then the system is moved in the opposite direction of the force, $\mathbf{d}$.

$$\mathbf{d} = -\mathbf{g} \tag{2.26}$$

Once the direction has been defined, the amount to move along the gradient line needs to be decided. This can be determined either by taking an arbitrary step size or by performing a line search. Steepest descents is a good method for avoiding high-energy configurations but the minimisation path oscillates and continually over-corrects itself which is inefficient. The method will also generate many small steps down a long narrow valley, which becomes computationally expensive as the minimisation evolves. It is important to note that in steepest descent minimisation method you cannot make any uphill moves so the algorithm always finds the nearest local minimum and cannot overcome energy barriers.

2.4 Molecular Dynamics Simulations

In a molecular dynamics (MD) simulation, configurations of the system are generated by integrating Newton's laws of motion thus creating a trajectory. The force on each particle will change depending on the positions of the all the other interacting particles in the system. As this results in all the particles being coupled to one another it is often referred to as a many-body problem, which cannot be solved analytically. Newton's equations of motion are therefore solved by breaking the integration into small time steps, Δt.

As force F is the negative first derivative of potential energy U with respect to position r ($F = -dU/dr$), the force acting on each particle in the system can be calculated

using the forcefield potential energy function in Equation 2.9. The force is then used to calculate the acceleration a of each particle at time t using $F = ma$ where m is the mass of the particle. Using the position and current velocity of each particle at time t we can calculate the particle's new positions and velocities at $t + \Delta t$. The force on each particle is now calculated at this new time $t + \Delta t$, which enables us to determine the new acceleration of each particle. These steps are repeated to generate new configurations after each time step, which can be displayed one after another as a trajectory. The timestep is typically 1-2 fs, and is limited by the fast frequency of bond stretching.

The Verlet algorithm is commonly used to generate trajectories in MD simulations[92]. It uses positions and accelerations from the current time and the positions from the previous time step to calculate the positions at the next time step. The new and previous positions can be approximated as a Taylor Series expansion (Equations 2.27 and 2.28) using the current position, velocities and accelerations.

$$\mathbf{r}(t + \Delta t) = \mathbf{r}(t) + \mathbf{v}(t)\Delta t + \frac{1}{2}\mathbf{a}(t)\Delta t^2 + \frac{1}{6}\mathbf{b}(t)\Delta t^3 + \mathbf{O}(\Delta t^4) \tag{2.27}$$

$$\mathbf{r}(t - \Delta t) = \mathbf{r}(t) - \mathbf{v}(t)\Delta t + \frac{1}{2}\mathbf{a}(t)\Delta t^2 - \frac{1}{6}\mathbf{b}(t)\Delta t^3 + \mathbf{O}(\Delta t^4) \tag{2.28}$$

These approximations are added together and rearranged to show the future position as:

$$\mathbf{r}(t + \Delta t) = 2\mathbf{r}(t) - \mathbf{r}(t - \Delta t) + \mathbf{a}(t)\Delta t^2 + \mathbf{O}(\Delta t^4) \tag{2.29}$$

The error is to the 4th order and although the velocities are not explicitly given they can be estimated from the difference in position at the previous and future time steps.

$$\mathbf{v}(t) = \frac{\mathbf{r}(t + \Delta t) - \mathbf{r}(t - \Delta t)}{2\Delta t} \tag{2.30}$$

As the Verlet method only requires two sets of positions and the acceleration for all atoms it does not require large amounts of memory however the velocities cannot be obtained until the positions of the next step have been computed.

The MD program GROMACS uses the Leap-frog algorithm[93] which has a different set of relationships (Equation 2.31 and 2.32). This method uses the velocities at $t - \frac{1}{2}\Delta t$

and the accelerations at t to calculate the velocities at $t + \frac{1}{2}\Delta t$. These velocities are then used to generate the new positions. The velocities at time t are obtained according to Equation 2.33.

$$\mathbf{v}(t + \frac{1}{2}\Delta t) = \mathbf{v}(t - \frac{1}{2}\Delta t) + \Delta t \mathbf{a}(t) \tag{2.31}$$

$$\mathbf{r}(t + \Delta t) = \mathbf{r}(t) + \Delta t \mathbf{v}(t + \frac{1}{2}\Delta t) \tag{2.32}$$

$$\mathbf{v}(t) = \frac{1}{2}\left(\mathbf{v}(t + \frac{1}{2}\Delta t) + \mathbf{v}(t - \frac{1}{2}\Delta t)\right) \tag{2.33}$$

2.5 Practical Considerations for MD

2.5.1 Thermostats

The temperature is a thermodynamic property that fluctuates in MD simulations. It is related to the kinetic energy K through the momentum of the particles in the system. Where N_c is the number of constraints and so $3N - N_c$ is the total number of degrees of freedom.

$$K = \sum_{i=1}^{N} \frac{\mathbf{p}_i^2}{2m_i} = \frac{k_B T}{2}(3N - N_c) \tag{2.34}$$

To control the temperature in a system, the weak coupling scheme of Berendsen[94] can be used. In this scheme an external heat bath is used to set the desired temperature. The bath can add or remove energy from the system thus altering the temperature by scaling the velocities after each step.

$$\frac{dT(t)}{dt} = \frac{1}{\tau}(T_{bath} - T(t)) \tag{2.35}$$

The magnitude of the parameter τ determines how tightly and bath and the system are coupled together. The change in temperature between steps is:

$$\Delta T = \frac{\Delta t}{\tau}(T_{bath} - T(t)) \tag{2.36}$$

And thus the scaling factor λ becomes:

$$\lambda^2 = 1 + \frac{\Delta t}{\tau}\left(\frac{T_{bath}}{T(t)} - 1\right) \tag{2.37}$$

A large value of τ leads to weak coupling and a small value leads to a strong coupling. If the value of the coupling parameter is equivalent to the time step then the original velocity scaling is recovered. A coupling constant of 0.4 ps is often used in conjunction with a time step of 1 fs. The advantage of using this type of coupling scheme is that the strength of the coupling can be adapted to what the user requires. The main downside is that the Berendsen thermostat does not generate a proper canonical ensemble as it suppresses the fluctuations of the kinetic energy. To correct the kinetic energy distribution a stochastic term can be added (Equation 2.38), this now becomes the velocity rescaling thermostat[95],

$$dK = (K_0 - K)\frac{dt}{\tau_T} + 2\sqrt{\frac{KK_0}{N_f}}\frac{dW}{\sqrt{\tau_T}} \tag{2.38}$$

Where N_f is the number of degrees of freedom, τ_T is the temperature coupling time constant and dW a Wiener process. This thermostat now produces the correct kinetic energy distribution with the same advantages as the Berendsen thermostat.

Another common method used to obtain constant temperature is that of an extended system method by Nosé[96] and Hoover[97]. The Hamiltonian of the system is extended by including a thermal reservoir and a friction term. The friction force is the product of each particle's velocity and the friction parameter ξ. The time derivative is calculated from the difference between the kinetic energy and the reference temperature. The equations of motion for the particles' under this scheme are given by Equation 2.39, where the equation of motion for the friction parameter ξ is given by Equation 2.40.

$$\frac{d^2\mathbf{r}_i}{d^2} = \frac{\mathbf{F}_i}{m_i} - \frac{p_\xi}{Q}\frac{dr_i}{dt} \tag{2.39}$$

$$\frac{dp_\xi}{dt} = (T - T_0) \tag{2.40}$$

The strength of the coupling is determined by the 'mass' parameter Q in tandem with the reference temperature T_0. The conserved quantity for the equations of motion

using the extended Nosé-Hoover equations of motion is given by the Hamiltonian H in Equation 2.41, where N_f is the total number of degrees of freedom.

$$H = \sum^{N} \frac{\mathbf{p}_i}{2m_i} + U(\mathbf{r}_1, \mathbf{r}_2, \ldots, \mathbf{r}_N) + \frac{p_\xi^2}{2Q} + N_f kT\xi \tag{2.41}$$

Barostats

ss The system can also be coupled to a barostat, such as the Parrinello-Rahman[98,99], that gives the correct NPT ensemble. The box vectors are represented by the matrix $\mathbf{b}$, the barostat volume of the box by V and $\mathbf{W}$ is a matrix parameter that determines the coupling strength. The matrices $\mathbf{b}$ and $\mathbf{P}_{ref}$ are the pressure and reference pressures, respectively.

$$\frac{d\mathbf{b}^2}{dt^2} = V\mathbf{W}^{-1}\mathbf{b}'^{-1}(\mathbf{P} - \mathbf{P}_{ref}) \tag{2.42}$$

The inverse mass parameter matrix $\mathbf{W}^{-1}$ determines the strength of the coupling (Equation 2.43). L is the largest box matrix element, the isothermal impressibilities β_{ij} and the pressure time constant τ_p can be defined to the user's specifications.

$$\left(\mathbf{W}^{-1}\right)_{ij} = \frac{4\pi^2\beta_{ij}}{3\tau_p^2 L} \tag{2.43}$$

The modified equations of motion are:

$$\frac{d^2\mathbf{r}_i}{d^2} = \frac{\mathbf{F}_i}{m_i} - \mathbf{M}\frac{d\mathbf{r}_i}{dt} \tag{2.44}$$

$$\mathbf{M} = \mathbf{b}^{-1}[\mathbf{b}\frac{d\mathbf{b}'}{dt} + \frac{d\mathbf{b}'}{dt}\mathbf{b}']\mathbf{b}'^{-1} \tag{2.45}$$

2.5.2 Periodic Boundary Conditions

Periodic boundary conditions allow simulations to be performed using a small number of particles yet still produce bulk properties. A three-dimensional shaped box of particles is replicated in all directions. The particle's coordinates in these image boxes can be computed using multiples of the box lengths. When a particle in the central box leaves it is replaced by an image particle from the opposite side, in this way the total number of particles remains constant inside the central box. A number of different shapes can be used for the periodic images; the most common is the cuboidal box due to its geometrical symmetry. If we try and calculate all the interactions between a particle in the central box with all other particles, including the image particles, then we get an infinite number of terms. This is impossible to calculate in practice, therefore for a short-range potential energy function we make an approximation by only considering interactions between a given particle, centered in a simulation cell the same size as the

simulation box, and other particles within that cell, that is with the closest periodic images of the other N-1 molecules. This is called the "minimum image convention" and was first used by Metropolis *et al.*[100]. The calculation of the potential energy in the minimum image convention involves 1/2 $N(N\text{-}1)$ terms, which still can be quite a large calculation for a high number of particles.

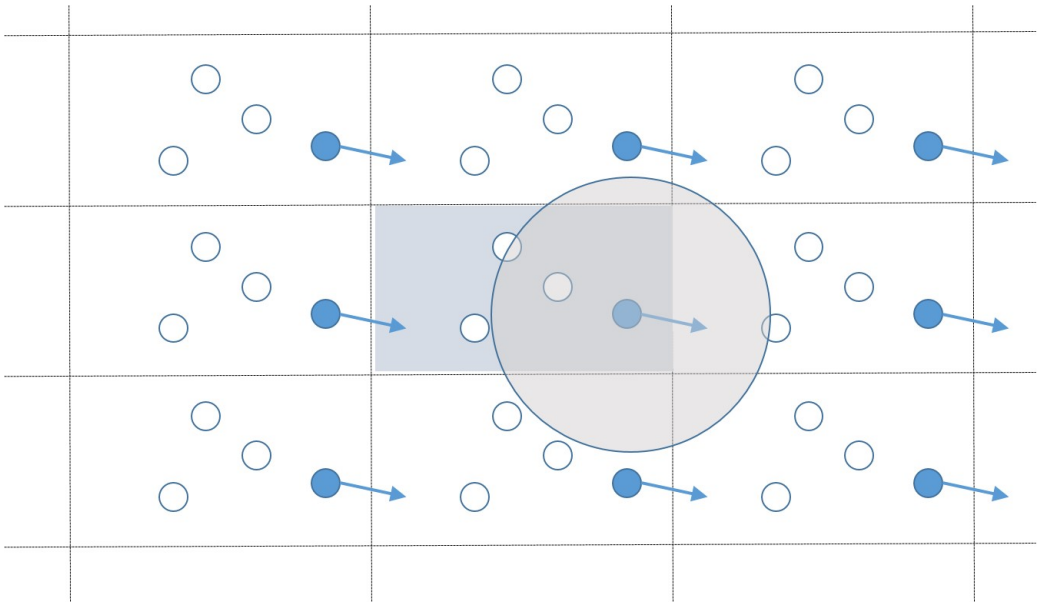

Figure 2.7: Periodic boundary conditions (shown in 2D for illustration purposes). The central square represents the simulation cell. As the solid particle moves out of the simulation cell it reappears on the other side. The circle shows the cut-off distance for the potential energy calculation and the shaded area within the circle contains the minmum images of all the particles with respect to the solid particle.

2.5.3 Ewald Summation

The Ewald summation method was first devised by Ewald[101] to study the energetics of ionic crystals. The method is used to calculate the Coulombic interactions between all particles in the simulation box and the periodic images in a cell array with a spherical edge. The central box is defined as a cube of side L and the image boxes are related by specifying a vector of a multiple of the box. In general, for a box which is positioned at a cubic lattice point $\mathbf{n}(= (n_xL, n_yL, n_zL)$, with n_x, n_y, n_z being integers, where r_{ij} is the minimum distance between the charges i and j, the contribution to the potential energy of the charge-charge interactions in the central box and its surrounding images is given in Equation 2.46. The prime on the first summation denotes that the series does not include the interaction $i = j$ for $\mathbf{n} = 0$

$$V = \frac{1}{2} \sum_{|\mathbf{n}|=0}^{\prime} \sum_{i=1}^{N} \sum_{j=1}^{N} \frac{q_i q_j}{4\pi\epsilon_0 |\mathbf{r}_{ij} + \mathbf{n}|} \tag{2.46}$$

In total there are the interactions in the central box, the interactions between the central box and all the image boxes and the interaction between the spherical array of boxes and the surrounding medium. The summation converges slowly and can vary

significantly at small values of r. A way to get around this problem is to split the summation into two separate series that both converge faster than their combination. To achieve this in the Ewald method, each charge is surrounded by a charge distribution, typically Gaussian, of equal magnitude and opposite sign. The sum of these interactions is performed in 'real space' and converges rapidly. To counteract this change a second charge distribution is added and the summation is performed in 'reciprocal space'. Finally a self-term is subtracted and a correction term is added depending upon the medium that was surrounding the sphere of simulation boxes. Although the Ewald sum is the 'correct' way to accurately calculate the interactions of long-range forces it is quite computationally expensive. Nevertheless, it has been used in simulations involving ionic melts, proteins, DNA and lipid bilayers. Improvements to the efficiency of the calculation of the reciprocal space summation using a grid-based charge distribution, known as the particle-mesh method[102], is a current popular approach and is the method used for all atomistic MD simulations in this thesis.

2.5.4 Constraints

For a large system with many particles the time step is often small to reproduce the dynamics. The caveat is that a small time step is computationally expensive. To circumvent this, a larger time step can be used if the bond lengths are constrained. These dynamic constraints are given by

$$m_i \mathbf{r}_i^{\cdot\cdot} = \mathbf{F} + \mathbf{g}_i \tag{2.47}$$

where r_i and m_i are the coordinates and mass of atom i, F is the force on atom i via the potential energy function and g is the constraint force. The most commonly used algorithms for bond constraints are SHAKE[103] and LINCS[104].

2.6 Free Energy Calculations

2.6.1 Introduction

Some processes, such as the penetration of a drug molecule across a membrane, occur on timescales longer that what is accessible through standard MD simulations. However, thermodynamic properties such as the free energy barriers can be determined through the use of advanced methods such as PMCF[41], umbrella sampling[105] and metadynamics[106]. These methods can be used to compute free energies by directing the system over these barriers on timescales that are feasible. In this thesis the PMCF method was used and is outlined below.

2.6.2 Potential of Mean Constraint Force Method

In this method the permeant, a water molecule in our case, is constrained via the centre of mass at a given height z in the bilayer (where z is the direction of the bilayer

normal) and allowed to freely move in the xy plane. For each step, the equation of motion is calculated and then the coordinates of the permeant are corrected to satisfy the distance constraint between the COM of the permeant and the bilayer. The force F_i required to maintain the constraint is calculated at each MD step and is given by:

$$F_i = m_i \frac{\Delta z}{(\Delta t)^2} \tag{2.48}$$

where m_i is the mass of the permeant, Δz is the displacement of the permeant along the constraint z axis and Δt is the time step. The force $F(z,t)$ acting on the permeant at a given z is equal to the negative of the force needed to maintain the constraint in the z direction. The free energy difference $\Delta G(z)$ can be synonymous with the potential of mean force (PMF) and is given by:

$$\Delta G(z) = -\int_{outside}^{z} \langle F(\acute{z}) \rangle_t d\acute{z} \tag{2.49}$$

Dynamic properties of the system, such as the diffusion $D(z)$, can also be calculated using the friction coefficient $I\acute{(}t)$ at each time and height using:

$$D(z) = \frac{RT}{\acute{I}} = \frac{(RT)^2}{\int_0^\infty \langle \Delta F(z,t) \bullet \Delta F(z,0) \rangle dt} \tag{2.50}$$

where R is the gas constant and T is the temperature. The permeability P of the permeant can then be calculated from the membrane resistance R_m:

$$R_m = \int_{outside}^{z} \frac{\exp(\Delta G(\acute{z})/RT)}{D(\acute{z})} d\acute{z} = \frac{1}{P} \tag{2.51}$$

This method has been described in greater detail in other studies.[8,42,43,107]

2.7 Coarse-Grained Models

2.7.1 Introduction

Simulating biological systems using an all atom forcefield can necessitate simulations of many thousands or even millions of particles. As such the number of interactions becomes large rather quickly. The result of this is that MD simulations are limited to certain length and timescales. A way to try and circumvent these limiting factors is to use a coarse-grained (CG) model instead, where a number of heavy atoms and their associated hydrogens are mapped onto a single interaction site[108–110]. This mapping tries to obtain the optimum balance between computational efficiency and chemical representability. A CG model will have improved computational efficiency as there would be a reduction in the number of particles in the system, which means less total interactions to calculate at each step. CG particles have a greater mass and thus oscillate more slowly, which in turn affords the use of a larger timestep. The inclusion of hydrogen atoms into the mapping leads to the loss of chemical details such as C-H

bonds, thus there is less friction and the energy landscape becomes smoother, which results in the resulting dynamics being artificially sped up, 4× faster in the Martini CG forcefield for example[110–112].

Although CG models have advantages over their all-atom counterparts, they also possess a number of caveats. The efficiency of the speed up given by the mapping is a direct result of the loss of chemical detail in the model. One such chemical detail is that of hydrogen bonding. Hydrogen bonding is not explicit in CG simulations but HBs are crucial to describing biological structure and function. Therefore, it becomes questionable whether the model can accurately and reliably reproduce experimental data. Often CG models use the mapping to interaction sites as a means to create chemical building blocks, an attempt to forgo the loss of chemical detail[108]. But this creates an alternate problem in terms of transferability and raises the issue of whether these building blocks can be used to model other molecules that have not been specifically parameterised for them. Further limitations of the Martini CG forcefield are described in Section 2.7.3 below. A CG model is used in Chapter 5 to simulate CER NS bilayers with varying amounts of water and DMSO to study the effects of penetration, amount of solvent and system size, and determine any possible artifacts in our systems to advise future researchers on appropriate bilayer sizes and solvent concentrations.

2.7.2 Development of Coarse-Grained (CG) Interaction Potentials

There are a number of different coarse-graining models; solvent-free models[113–115], models with explicit water[116–118] or models that include chemical specificity[108,119]. The development of these models can be split into bottom-up or top-down approaches. A bottom-up approach leads to models that have been parameterised through the use of atomistic simulations to develop a CG potential via Boltzmann inversion[120] or force matching approaches[119]. A top-down approach is where the non-bonded interactions are parameterised to create chemical building blocks that can be used for a broad range of applications without the need for reparameterisation. These building blocks are validated either from comparison with atomistic simulations[121–123] or experimental data[124–128].

2.7.3 Martini Forcefield

Mapping

The Martini model[108–110], which is used in Chapter 5, uses a four-to-one mapping of heavy atoms and associated hydrogens. The mapping of water is the same, as four water molecules are mapped to a CG water bead. Ions are represented by a single CG bead, representing the ion and its first hydration shell. Ring molecules (e.g. benzene, cholesterol and some amino acids) are mapped at a higher resolution, use up to two heavy atoms to a CG bead. The beads which are akin to chemical building blocks are different types. The Martini model has four main types of particle: polar (P), non-polar

(N), apolar (A), and charged (Q), and each of these has subtypes that denote its hydrogen bonding properties or its degree of polarity. For example, d = donor, a = acceptor, da = both, 0 = none, and number from 1 = low polarity to 5 = high polarity. These different combinations of types and subtypes gives rise to a total of 18 different CG beads.

Potential Energy Function

The bonded interactions in the Martini model are described by the standard set of potential energy functions, using harmonic bond and angle potentials, and dihedral potentials, see Section 2.2. Proper dihedrals are mainly used to give secondary structures to peptides, while improper dihedrals are used to prevent out-of-plane distortions of planar groups. The bonded interactions are parameterised using data from atomistic geometries or via comparison with atomistic simulations. In this parameterised approach, the atomistic simulations are converted into a mapped CG simulation by matching the centre of mass of the corresponding atoms to the centre of mass of the CG bead. The distribution functions are calculated for the mapped simulation and compared to those obtained from the true CG simulation. Finally, the CG parameters are changed gradually through a series of iterations until there is a satisfactory overlap of the distribution function.

The non-bonded interactions are described by a LJ 12-6 potential. The strength of these interactions is determined by the well depth, ϵ_{ij}, which ranges from 5.6 to 2.0 kJ mol^{-1}, for strongly polar groups and between polar and apolar groups respectively. The size of the particles is determined by $\sigma = 0.47$ nm for normal particles and $\sigma = 0.43$ nm for ring-like molecules. The ϵ_{ij} value is also scaled to 75% of the standard value for these ring-like molecules. Charge groups are given a charge $\pm e$ and interact via a Coulombic energy function. Coulombic interactions are screened with a relative dielectric constant $\epsilon_{rel} = 15$ to account for the reduced set of partial charges seen in an atomistic forcefield. The non-bonded interactions are cutoff at $r_{cut} = 1.2$ nm. The LJ potential is shifted from $r_{shift} = 0.9$ nm to r_{cut}. Introducing this shift creates an artificial distance-dependent screening effect. Non-bonded interactions were parameterised using a systematic comparison to experimental data including the free energy of hydration, the free energy of vaporisation, and the partitioning free energies between water and a number of organic phases, for each of the 18 different CG particle types. Martini simulations are stable with a timestep up to 40 fs or 20 fs for systems that contain ring-like structures[108–110]. Lower values for the timestep are inefficient due to numerical integration time steps[129].

Validation

The Martini forcefield provides parameters for an assortment of biomolecules including different lipid types[108,130–132]. The premise that CG beads act as chemical building blocks and are parameterised so that they are transferable for other molecules requires

validation. One way is to validate against atomistic simulations, such as in a study that reproduced atomistic dimerization free energies of amino acid side chain analogues to within 1 kT and the replication of atomistic profiles of fullerene pairs, in a variety of solvents, through calculations of the potential of mean force[123]. A second way to validate is in comparison with experimental data. For example the areas per lipid are within 0.1-0.2 nm^2 for many different lipid membranes[108,110] simulated using the Martini CG forcefield. An advantage of using a model type like Martini is due to its limited set of interaction parameters they can be further optimised by other researchers. Due to the flexibility and transferability of the Martini interaction parameters there have been a wide range of applications including; lipid membrane characterisation[133–135], lipid polymorphism[136] membrane protein oligomerisation[137], self-assembly of soluble peptides and proteins[138], conformation changes in proteins[139], peptide induced membrane permeabilisation[109], drug and gene delivery systems[140], lipoprotein particles[141], membrane fusion[142], lipid monolayers[143], surfactant self-assembly[108], carbohydrates[144], polymers[145], and nanoparticles[146].

Limitations

The Martini forcefield has a number of limitations, some of which are inherently a CG problem, in that the mapping limits both the chemical and spatial resolution of the model. This can be observed when trying to map beads to the lipid DMPC, having 14 carbon atoms, which lies somewhere between 3 and 4 beads. Therefore the mapping to specific lipids is not unique, and so properties such as the lipid bilayer density profiles become limited. This can also be seen in the sterols, where a small change in the ring structure can have a significant effect on the thermodynamics of systems containing these biomolecules, which are not represented in a CG model. An effort to improve the parameters of Martini sterols using a virtual-site description has been shown by Melo *et al.*[147]. Another limitation is the ability of the model to account for electronic polarizability, such as the interactions in proteins and the interactions between benzene molecules. The CG model struggles to reproduce the resulting geometries. Although coarse-graining creates a smoother energy landscape, speeding up the kinetics of the system[148]. The consequences of this effect can not be easily predicted. It has been shown that Martini generates a 4× speed-up[110,111], but this speed-up is molecule type dependent[112]. The lack of explicit HBs in the model could be an explanation for why some molecules govern different speed-ups. This speed-up in simulation time can also be expressed in terms of diffusion, therefore properties such as viscosity need to be carefully examined when dealing with CG systems. One of the biggest limitations of the Martini forcefield is the limited fluid range given by the LJ 12-6 potential, which often results in water freezing even at room temperature, with the melting temperature at 290 ± 5K[110]. A way to remedy this freezing effect is to include the addition of water particles with a slightly larger radius, known as 'anti-freeze' particles[110] or through the use of a polarizable water model[149].

2.7.4 CG Ceramides

The Martini force field is commonly used for simulating lipids[130–132,136,150–153] but there are few attempts to incorporate parameters for CERs. In general there is a lack of experimental data on detailed compositions of pure CER bilayers. As a result of this, to parameterise a CER CG force field, atomistic simulation data must be considered instead.

For the CG model of CER NS by Sovova[9], the standard Martini parameters for the hydrocarbon tails were unchanged except an additional bead was added to the sphingosine tail to reproduce the atomistically determined membrane thickness. This change resulted in a 3 to 1 mapping of some of the tail beads rather than the standard 4 to 1 for the entire molecule. The parameterisation method was that of Hinner *et al.*[134] and a mapping scheme that produced unimodal distributions of bond lengths and angles was preferred. The bonding parameters were adjusted to reproduce area per lipid and membrane thickness properties in-line with their atomistic counterparts. The headgroup parameters were modified to focus on reproducing the gel phase at 300 K. Two sets of CG parameters were produced, with and without dihedral terms for the headgroup region. However, deployment of the parameters with the dihedral term limits the timestep to 8 fs for stable simulations compared to 30 fs without.

The mapping of the scheme that converts the atomistic representation of CER NS to a CG one is shown in Figure 2.8. In this model, the probability distributions of bond lengths are in good agreement with the atomistic simulations of Sovova[9]. The angles less so, as there is a compromise to get a good agreement for the area per lipid. Inclusion of the dihedral terms reproduces the dihedral distribution well but given the similar overall results regardless if they are included, they are most likely to be omitted allowing for a much longer time step (30 fs)[9].

To validate the CG forcefield parameters, a number of properties were calculated and compared with previous atomistic simulations of CER NS and experimental values where possible. The APL value of 0.46 nm^2 is a bit larger than the experimental value for CER NS with C16:0 (0.38 nm^2)[31] although the authors claim this may be down to shorter tailed CERs in a monolayer arrangement[9]. Comparison with other simulation studies using atomistic forcefields is difficult due to variation in simulation temperature and acyl tail length. For example, Guo *et al.*[154] reported 0.424 nm^2 for CER NS with 16:0 acyl tail at 305 K, Metcalf and Pandit[155] give a value of 0.44 nm^2 for CER with C24:0 tail at 323 K, and Notman *et al.*[156] calculated an APL of 0.374 nm^2 for lignoceryl CER NS at 323 K.

Another structural property commonly calculated is the membrane thickness. The thickness calculated using this forcefield is 4.9 nm and is the same for their atomistic simulations and the value of 4.94 nm by Notman *et al.*[156] and Das *et al.*[8] An experi-

mental value for the repeat distance of dehydrated CER NS is 5.6 nm through the X-ray diffraction experiments of Shah *et al.*[30], adjusting for the addition of the headgroup region shows reasonable agreement with the CG model of Sovova. It is important to note that CG models cannot reproduce the tilt of CER tails[157] and overestimate the area compressibility modulus in the gel phase compared to atomistic simulations (22.3 N m^{-1} compared to 3.2 N m^{-1})[9]. Comparison of electron density profiles between the CG and atomistic simulations shows them to have similar positions of the main peaks and thus are in good agreement and ultimately describe the behaviour of CER NS below the phase transition temperature reasonably well.

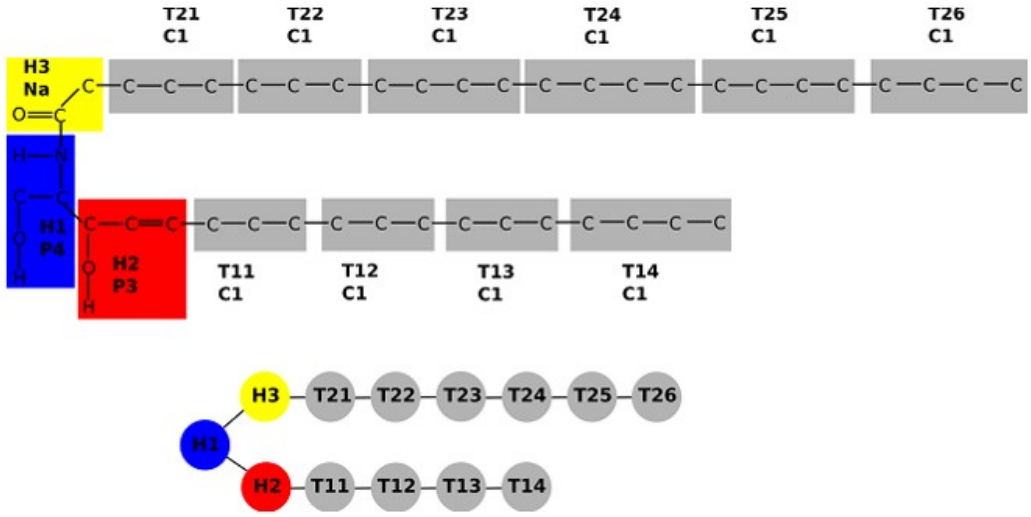

Figure 2.8: Mapping scheme and bead types for ceramide NS in the adapted Martini forcefield by Sovova[9]. Figure reproduced from Sovova[9] with permission from ACS Publications.

2.7.5 CG DMSO

DMSO is comprised of a polar sulfoxide group and two hydrophobic methyl groups; its molecular structure is shown in Figure 1.12. DMSO shows stronger interactions with water, than water does with itself, due to both dipole-dipole and hydrogen bonding interactions[158]. These interactions lead to non-ideal behaviour in regards to the heat of vaporisation of DMSO in water[159] and its freezing[160]. As DMSO has an amphiphilic nature, it could be better represented as a dimer, with a polar and non-polar bead connected by a weak harmonic bond[72] (See Figure 2.9). Generally, a CG forcefield[108] would have a mapping of 4 atoms to a single bead, but for this idea a single bead to represent DMSO would not give suitable chemical characteristics.

The LJ interactions of the nonpolar bead are the same as those in the CG DPPC model. The LJ interaction parameter, ϵ, of the polar CG bead, was adjusted to reproduce the relative heat of vaporisation of DMSO, with respect to the CG water model, through a series of MD simulations of pure CG DMSO systems in a similar fashion as that of

Geerke *et al.*[159]. Another process in the parameterisation of this model was to incorporate the effect of the stronger interaction between DMSO and water than that of itself[158]. This is obtained through calculation of the internal energy of simulations of equimolar mixtures of DMSO and water, leading to an increased value of ϵ for the polar DMSO bead compared to the DMSO-DMSO interaction. The DMSO-lipid interactions remain the same as those from the generic CG polar and nonpolar beads that form the DMSO dimer. Greater detail can be found on the parameterisation of this forcefield in the study by Notman *et al.*[72] and its supporting information.

This forcefield was used in the simulations of a DPPC bilayer in water with varying concentrations of DMSO in the study by Notman *et al.*[72]. The results for area per lipid and bilayer thickness as a function of DMSO concentration as well as the density profile of the DPPC bilayer containing 6 mol% DMSO are consistent with the X-ray scattering experiments of Yu and Quinn[161] on the bilayer fluid phase, which shows a decrease in the thickness with an increase in the DMSO concentration. The observations of that study were also in-line with those seen in atomistic simulations of similar systems by Sum and de Pablo[162]. The area per lipid headgroup has quantitative agreement, 0.71 nm^2 for 6 mol% DMSO at 323 K compared with 0.72 nm^2 for 5 mol% DMSO at 325 K in Sum and de Pablo, and shows that the model is beyond the 'semi-quantitative' CG lipid forcefield of Marrink *et al.*[108].

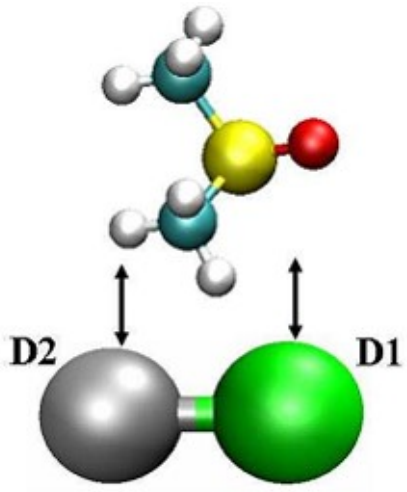

Figure 2.9: DMSO as two CG beads denoted D1 and D2 for a hydrophilic particle (green) and a hydrophobic particle (grey). The DMSO carbon atoms are coloured cyan, sulphur in yellow, oxygen in red and hydrogen in white.

2.8 Simulation Set-ups Used in this Thesis

2.8.1 Atomistic simulations (Chapters 3 and 4)

In Chapter 3, CER NS bilayers containing 284 lipids with varying concentrations of hydration (0, 2, 4, 6, 10 and 30 waters per lipid) were produced. Water was equilibrated around the CERs at 305 K with diminishing position restraints for a total of 5 ns followed by a further 1 ns without position restraints. Each system was replicated in the z direction to produce two bilayers stacked on top of each other. Systems were ran for 40 ns, the first 20 ns is classed as an equilibration period to reach a stable area per lipid. A more detailed protocol is provided in Section 3.2.1

In Chapter 4, a configuration of an equilibrated pure hydrated CER bilayer at 100 ns was taken from Thind *et al.*[163] and used as the starting configuration for a steered MD simulation. A pure 288 OA bilayer was hydrated with 30.2 water molecules per lipid, as in the pure CER bilayer. The structure was energy minimised and equilibrated, first with position restraints on the OA molecules and then without position restraints in the NPT ensemble for 5 ns. A further 20 ns NPT run was made to ensure all the bilayer properties had reached equilibrium. The mixed CER and OA bilayer was constructed and energy minimised, with a 5 ns NPT equilibration with position restraints on the CERs. The bilayer was hydrated with a further energy minimisation and NPT ensemble equilibration. A further 20 ns NPT run was made to ensure all the bilayer properties had reached equilibrium. A more detailed protocol can be found in Section 4.2.1.

For all atomistic simulations, the potential energy function and interaction parameters employed for the CER were based on the united atom forcefield of Berger[34] and partial charges were applied to the headgroup in the manner of Mombelli[91]. This forcefield has been described in detail in previous works[156] and in Section 2.2.9 of this thesis. The parameters for OA were also taken from Berger. The water was modelled using the SPC potential[164].

Simulations were carried out using the GROMACS package version 4.5.4[165], and employed the Nose-Hoover thermostats[96] coupled separately to the lipid and water molecules with a time constant of 5 ps and a Parrinello-Rahman barostat[98] with a time constant of 5 ps and compressibility of 4.5×10^5 bar^{-1} for semi-isotropic pressure coupling. The simulation cell was kept orthogonal by setting the off-diagonal terms of the compressibility matrix to zero. Standard periodic boundary conditions were applied in all three directions. All bonds were constrained using the LINCS algorithm[104] and the time step was 1 fs. The LJ interaction cut-off was 1.2 nm using a shift function. Particle Mesh Ewald summation was used for the electrostatics with a cut-off of 1.4 nm for the short range part of the calculation.

2.8.2 Coarse-Grained Simulations (Chapter 5)

In Chapter 5, a single CER NS molecule was replicated in the x and y dimensions, producing a monolayer 8×4 long. This was replicated in the z direction to create a bilayer containing 128 lipids. This was used as a basic block in building the larger bilayer systems denoted 'L'. For the 2L systems, the block was replicated in the x direction (2×1). For the 4L systems, the block was replicated in both the x and y (2×2). For the 8L systems, the block was replicated four times in the x direction and two times in the y (4×2). Each of these systems also contains 10, 50, 70 and 100 solvents per lipid, where the possible effects of the amount of solvent can now be monitored. The solvent consisted of a composition of water and DMSO (0.625 mol%). To equilibrate the systems an energy minimisation was first performed, followed by a 480 ns NPT run with position restraints of 1000 kJ mol^{-1} on the CERs in all directions, enabling the solvent to equilibrate. Due to slow convergence of the volume of the solvent, the reference pressure was increased in the z direction to four times that in the x and y for 75 ns. Once the volume had equilibrated, a 75 ns simulation was performed to relax the system at standard pressure. Finally, position restraints were removed and the systems were ran for a further 150 ns in the NPT ensemble to ensure the systems had equilibrated and the APL remained constant. All systems were ran at 305 K and 1 bar pressure. Systems were then ran for 3 μs where the first 2 μs are regarded as equilibration for penetration of DMSO in the bilayer. The final 1 μs trajectories are the production runs and were used for our analysis. A more detailed description of this protocol can be found in Section 5.2.1

The potential energy function and interaction parameters employed for the CER were based on the modified Martini coarse-grained forcefield of Sovova[9], using a 4:1 mapping of heavy atoms to CG beads. DMSO parameters were described by the forcefield of Notman seen in previous works[72]. The water was modelled using the Martini forcefield[110].

Simulations were carried out in the NPT ensemble using the GROMACS package[165], and employed the V-rescale thermostats[95] coupled separately to the lipid and solvent molecules with a time constant of 5 ps and a Berendsen barostat[94] with a time constant of 1 ps and compressibility of 3.0 x 10^5 bar^{-1} for semi-isotropic pressure coupling. The simulation cell was kept orthogonal by setting the off-diagonal terms of the compressibility matrix to zero. Standard periodic boundary conditions were applied in all three directions. All bonds were constrained using the LINCS algorithm[104] with a time step of 30 fs. The LJ interaction cut-off was 1.2 nm using a shift function and a cut-off of 1.4 nm was used for the Coulombic interactions.

Chapter 3

A Molecular Dynamics Investigation of the Influence of Hydration on Structural Properties of Ceramide NS Multilayers

3.1 Introduction

The SC is the topmost layer of the skin and helps govern which substances can permeate in and out of the body[11]. This biological material thus helps maintain the correct water levels required for the body to function optimally through the use of this barrier. Consequently, if we want to maximise the potential of transdermal drug delivery and improve the quality of personal care products (moisturiser, shower gel, make-up etc.) a greater understanding of the SC's molecular structure and organisation in relation to its barrier properties will be fundamental. A detail description of the structure and organisation of the skin can be found in Section 1.2.

Although the SC has strong barrier properties, it is still prone to disruption, which can allow pathogens to infiltrate and cause disease. Diseased skin is often associated with changes in lipid composition[166–168] including that of atopic dermatitis[23]. Another side effect of this breakdown is the water loss from the skin. Dehydration of the skin is a common factor in many skin diseases such as eczema and other forms of dermatitis, linked to abnormal ceramide composition[169–173]. There has been considerable research into solutions for atopic dermatitis such as moisturising creams containing colloidal oatmeal[174], emollinets[175] and ceramides[176–180]. Another approach is through diet using supplements[181,182]. All these approaches reduce transepidermal water loss, keeping skin hydrated and healthy. For healthy skin the water content has been reported to exist at varying amounts, between 15 and 40 % by weight[183–185]. A small amount of

water is bound to molecules such as Natural Moisturising Factor (NMF) and within the lipid matrix[186]. Most recently there has been evidence to suggest that only a small amount of water (∼2wpl) may exist between lamellar layers[187] in the form of pools.

Water is a key contributor to the structure and dynamics of lipid bilayers due to the hydrophobic nature of lipid tail groups. Effects of hydration have been readily studied on a variety of lipids and has shown to lead to the swelling of DPPC bilayers[188–190] and thus an increase in thickness. Hydration can also have a significant effect on the phase of DMPC[191] and DPPC[192] bilayers. For example, a neutron scattering study of hydration dependent DMPC bilayers by Trapp and colleagues shows that a reduction in the water content moves the transition temperature to higher temperatures and is related to the mobility of the head group protons[193]. Ulrich has also shown a similar effect, that the lipid chain melting point and ice melting point are hydration dependent in DOPC bilayers[189]. Jendrasiak and Smith studied the hydration behaviour of a number of sphingomyelins (SM) in combination with other lipids using adsorption isotherms[194]. The presence of choline in the phospholipid headgroup did not guarantee strong water adsorption. The headgroup was also removed from the SM to study ceramides, which were found to be very weak water absorbers.

There appears to be limited studies of hydration effects on the barrier function of the skin as it is experimentally challenging due to the complexity of the systems, as both keratin and desmosomes[12] are surrounded by the lipid matrix. Most experimental studies assessing hydration are able to give structural data on these systems but lack detailed information on the SC's molecular interactions. Tfayli *et al.* used Raman spectroscopy to show the effect of relative humidity variations on the polar interactions, lateral packing and conformational order of three different ceramide species[195]. CER 3 and 5 showed a more compact and organised structure with stronger polar interactions at intermediate hydration, while the opposite was true for CER 2. While Bouwstra *et al.* showed high levels of water content can reduce the ordering of lipids in the SC and may explain the strong the penetration-enhancing effect of water[26]. Numerous other experimental techniques have been used to study hydration effects on ceramide systems including Infrared spectroscopy[196], high-resolution cryo-scanning electron microscopy[197], X-ray powder diffraction[198], FT-Raman spectroscopy[198], differential scanning calorimetry (DSC) and attenuated total reflection Fourier transform infrared spectroscopy (ATR-FTIR). It can be seen that hydration has a significant effect on the packing of ceramides, with a decrease in the hydration leading to orthorhombic phase[196] in a number of ceramides, and even a liquid phase in anhydrous CER AS bilayers[198] when above the melting chain transition temperature.

Molecular simulations can provide information on the interactions at this small length scale that are out of the reach of conventional experimental techniques. Studies on the effects of hydration are becoming more prominent and reveal greater ordering of

the headgroups of DMPC[199] and DOPC[200] at low hydration levels. These low levels of hydration stabilize gel phase DPPC bilayers in CG models[157]. Structural changes are believed to be modest compared to that of dynamical properties, Pinnick *et al.* for example showed that water diffusion increases upon further hydration in POPC bilayers[201]. Other dynamical properties such the orientational dynamics of water have been studied as a function of hydration in DLPC bilayers[202]. Hydration also affects the electronic properties, such as the surface potential, dipole and quadrupole moments of lipids as can be viewed in ab intio calculations of PC[203].

Again, as with experimental data, changes in hydration on ceramide bilayers are limited in comparison to the well studied phospholipids. Del Regno and Notman[204] studied the permeation pathways through lateral domains in tertiary component bilayers at different lipid ratios and levels of hydration using potential of mean constrained force calculation. It was found that CHOL-rich domains emerge from heterogeneously distributed fully hydrated bilayers over time and it is through these domains that water has a favourable permeation pathway. The authors suggest this permeation pathway is favourable due the CHOL having a disordering effect on the gel-phase lipids. For comparison, in low hydrated systems, water pools form between headgroups causing both wet and dry regions. These water pools effect the permeation pathway. Other simulation studies that have simulated low hydration bilayers also observe a similar effect[9,205]. Sovova *et al.* provide CG force field parameters for CER NS that are consistent with the Martini forcefield and show good agreement with previous atomistic simulations. These parameters were then used to simulate the phase behaviour of CER NS as a function of hydration and temperature. It was observed that the bilayer melt into an irregular phase at low hydration with water droplets of varying size. In a study of dehydration of multilamellar fatty acid bilayers, it was observed that charged fatty acids are able to sequester cations between lamellae that are fully hydrated and thus suggests that undulations in this structure can control the diffusion of hydrophilic substances by altering the positional and rotational order of water molecules in the form of droplets[205] and water pools were also seen in dehydrated fatty acid membranes.

Generally in simulation of bilayers, a single membrane is studied along with periodic boundary conditions to replicate the structure in all directions to generate macroscopic properties. For MD simulations of ion channel permeation the use of a two-bilayer setup is a common occurrence. One can use the compartments, created via this setup, to have a charge imbalance which create an ionic concentration gradient and potential difference across the membrane. This has been applied by Kutzner *et al.*[206] in predicting ion conductance and selectivity, as well as illuminating the mechanisms for this conductance in bacterial channels. This double bilayer setup has been used numerous times by de Groot and colleagues in electrophysiology simulations of ion permeation in potassium channels[207–209]. The setup has also previously been used to study the osmotic pressure asserted on bilayers[210] and its associated affect on water transport

through carbon nanotubes[211]. In simulations of SC lipids one would also want to use multilayer structures rather than single bilayer, as they can restrict the conformations the ceramides can adopt and thus limit the insight gained. Continued advancement in hardware now allows us simulate larger systems at the ns and even μs timescales. As a result, there is an increasing trend at looking at multilayers of SC components in the literature[212–215]. For example, Iwai and others studied stacked bilayers of fully extended ceramides with cholesterol and show that this structure can rationalise the skin's low permeability toward water and other hydrophilic substances and is robust towards other environmental factors[212]. Das used multilayers to show that at physiological temperatures a gel-like phase can be found, and this phase facilitates rapid cholesterol flip-flop[214].

In this chapter we have carried out MD simulations of double ceramide bilayers with varying levels of hydration to determine the effects of hydration on the structural and dynamic properties of the bilayer, with the aim furthering our understanding of how water influences the permeability of skin and elucidating and links between the water content of the skin and the optimal flexibility and permeability of skin required for normal function. Double bilayers, where two bilayers are stacked on top of each other with a thin water layer between were chosen to allow for the calculation of inter-leaflet hydrogen bonds between bilayers low levels of water.

3.2 Computational Methodology

3.2.1 Initial Configurations

Initial configurations were generated by creating a 12 x 12 grid of ceramide NS lipids in the hair pin conformation, molecular structure given in Figure 1.3. The grid was energy minimised. The two end lipids were removed leading to a monolayer containing 142 lipids. The monolayer was reflected so that a bilayer containing 284 lipids was produced. The dimensions of the simulation box were 7.594, 7.594, 6.655 nm for the x, y, z directions respectively. The simulation box was increased to allow for the random addition of water molecules fill space above and below the bilayer. The z dimension of the box was set to 6.655, 6.655, 6.8, 7.0, 7.5 and 11.0 nm for the six systems with the varying levels of hydration; 0, 2, 4, 6, 10 and 30 waters per lipid (wpl), were produced, see Figure 3.2. Any excess water between the headgroups of each leaflet for each bilayer was removed. The water was equilibrated around the ceramides first using the NVT ensemble at 305 K for 1 ns with position restraints on the ceramides in all directions, followed by an equilibration period of 4 ns under the NPT ensemble with position restraints decreasing from 10000 to 0 kJ mol^{-1} and a final 1 ns with no restraints. For lower hydration levels of water (2wpl and 4wpl) it proved problematic to achieve an uniform distribution of water in all coordinate directions, therefore a multiple step process was required to equilibrate the water molecules around the ceramides, as detailed in Table 3.1. The bilayer in these systems was duplicated after Step 2.

Step	Ensemble	Time (ns)	H_2O Temp(K)	Restraints (kJ mol^{-1})
1	NVT	2	405	10,000
2	NPT	2	405	10,000
3	NPT	1	405	10,000
4	NPT	1	355	10,000
5	NPT	1	305	10,000
6	NPT	1	305	1000
7	NPT	1	305	100
8	NPT	1	305	0

Table 3.1: Equilibration steps for low levels of hydration.

Each system was then replicated in the z direction to produce a double bilayer. All systems were run for 40 ns, the first 20 ns is regarded as the equilibration time for ceramides at each hydration level to reach its equilibrium value for the area per lipid. The area per lipid over time can be seen in Figure 3.1 where the APL plateaus for each hydration level within the first 20 ns. The number of hydrogen bonds as a function of time can also be used to verify the equilibration of the systems. Therefore, the final 20 ns trajectories were used for our analysis. No extra repeat simulations were ran, but structural properties calculated include both bilayers except for the bilayer thickness

which was calculated separately and can be compared with each other.

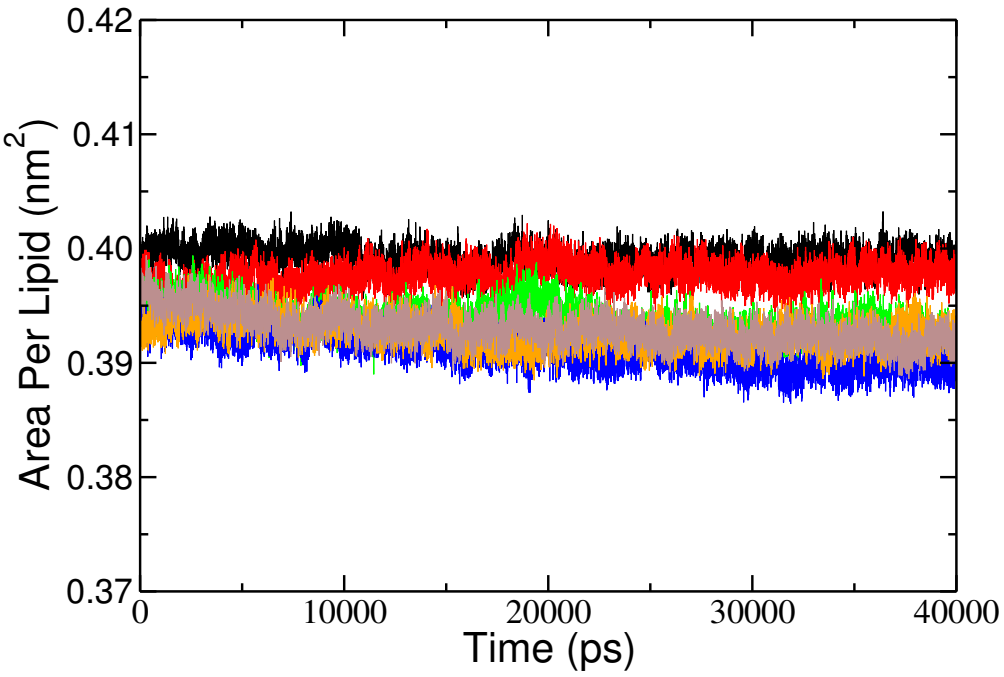

Figure 3.1: Area per lipid as a function of hydration over time. 0 wpl in black, 2 wpl in red, 4 wpl in green, 6 wpl in blue, 10 wpl in orange and 30 wpl in grey.

3.2.2 Forcefield details

The potential energy function and interaction parameters employed for the ceramide were based on the united atom forcefield of Berger[34], which was originally parameterized for phospholipids and uses GROMOS87 parameters for headgroups and a Ryckaert-Bellemans potential for the lipid tails. This forcefield has been described in detail in Section 2.2.9. The forcefield gives sufficient agreement with experimental data for structural properties such as bilayer thickness, chain tilt, APL, density profiles and order parameters which can be see in the comparison of forcefields by Papadimitriou[35]. Due to its united atom approach, and inability to observe the orientation of the H-atoms one cannot see the possible orthorhombic phase. The water was modelled using the SPC potential[164].

3.2.3 Simulation Parameters

Simulations were carried out in the *NPT* ensemble using the GROMACS package version 4.5.4[165], and employed the Nosé-Hoover thermostats[96] coupled separately to the lipid and water molecules with a time constant of 5 ps and a Parrinello-Rahman barostat[98] with a time constant of 5 ps and compressibility of 4.5 x 10^5 bar^{-1} for semi-isotropic pressure coupling. The simulation cell was kept orthogonal by setting the off-diagonal terms of the compressibility matrix to zero. Standard periodic boundary conditions were applied in all three directions. All bonds were constrained using the

LINCS algorithm[104] and the time step was 1 fs. The Lennard-Jones interaction cut-off was 1.2 nm using a shift function. Particle Mesh Ewald summation was used for the electrostatics with a cut-off of 1.4 nm for the short range part of the calculation. Results were analysed using the GROMACS[165] package and MEMBPLUGIN[216] in VMD[217].

3.2.4 Analysis

Area per Lipid

Area per Lipid is an essential property to describe membranes as it is one of the few parameters that can be directly compared with experiment to validate our simulation results. The area per lipid is affected by the phase, fluidity and as we will show here, level of hydration. In simulations of membranes this parameter is often used to determine the extent of equilibration of the system. The x and y coordinates of the previous set of points are projected onto a plane determined by the simulation box. This is divided into polygons through a Voronoi diagram and the area for each is calculated using analysis via MEMBPLUGIN[216] and is averaged over the 20 ns trajectory period.

Thickness

The thickness of a bilayer depends on the lengths of the lipid acyl chains which compose the membrane. The tilt angle of these chains also heavily contributes to this property. The membrane thickness tool in MEMBPLUGIN measures the distance w between two density peaks, the first and second central moment of the mass density profile of a chosen atom along the membrane normal. Often the bilayer thickness in phospholipids is measured using the phosphate-to-phosphate distance between leaflets but as ceramides lack this atom type, the amide nitrogen is used as a substitute. The thickness is measured over time and averaged over the 20 ns trajectory period using the MEMBPLUGIN[216] tool in VMD[217].

Tilt Angle

The tilt angle can help define the structural properties of the membrane. The tilt angle can be calculated between a chosen vector, defined by two atoms of a lipid, and the bilayer normal, in this case the z axis via the MEMBPLUGIN[216] tool in VMD[217]. The tilt angle is averaged over the 20 ns trajectory.

Order Parameters

The structural ordering of the hydrophobic tails in lipid membranes directly affects the membrane fluidity and the thickness. Deuterium order parameters can be measured experimentally using NMR techniques. The order parameters for each methyl group C_n is calculated using the following equation:

$$S_z = \frac{3}{2}\langle \cos^2 \theta_z \rangle - \frac{1}{2} \tag{3.1}$$

where θ_z is the angle between the z-axis of the simulation box and the molecular axis under consideration. The molecular axis is defined as the vector from $C_{(n-1)}$ to $C_{(n+1)}$. The brackets indicate the ensemble average. The order parameter for each CH_2 segment was calculated separately for each axis giving a good idea of the ordering from head to tail. An order parameter of 1 indicates full order along the interface normal, -1/2 represents full order perpendicular to the normal while 0 represents isotropic orientation.

Density Profiles

Density profiles are constructed by dividing the bilayer into slices along the normal direction and averaging the number of different components in each slice using the density tool in Gromacs. The ceramide, water and headgroup density are calculated in this manner.

Percentage Coverage

The bilayer was split into a grid in the xy plane, where each grid box was the estimated size of a water molecule. By selecting water within a certain z range, it was possible to determine which grid box each water molecule in the system fits into. The percentage of boxes filled is defined as the percentage coverage.

Hydrogen Bonding

The number of ceramide-water, lateral (between ceramides in the same monolayers) and perpendicular (between ceramides in adjacent monolayers) ceramide-ceramide hydrogen bonds were calculated using the geometric criteria:

$$r \leq r_{HB} = 0.35nm \tag{3.2}$$

$$\alpha \leq \alpha_{HB} = 30^\circ \tag{3.3}$$

The value of $r_{HB} = 0.35$ nm corresponds to the first minimum of the RDF of SPC water. The program analyses the donor-acceptor distance (r) distribution and hydrogen-donor-acceptor angle (α) distribution of all H-bonds as well as the number of H-bonds in each time frame.

3.3 Results

Observation of the trajectories of the simulations allows monitoring of any additional structural and dynamical changes that are not seen in the common analysis motifs. In Figure 3.2 we can see for the higher levels of hydration (30 and 10 wpl) that there is an even distribution of water, above and below the bilayers. No water enters the bilayers during both the equilibration and production runs except for a single molecule in the 30 wpl. For lower levels of hydration (6 wpl, 4 wpl and 2 wpl), an uneven distribution of water is seen as the simulation progresses despite a somewhat uniform starting distribution. A 'pooling' of the water molecules occurs at the interface leading to larger bilayer curvature. This 'pooling' of the water molecules to form droplets has been observed in other low hydration FFA[205] and CER[9,204] simulations. Throughout the simulations almost no water entered the bilayer due to the excellent barrier properties of the ceramides enhanced by the lateral hydrogen bonding network between adjacent ceramides. By looking at the positions of the centre of mass of each ceramide in the xy plane, we observed the hexagonally packed structure. Although a higher level of order can be seen for greater hydrated ceramides, a number of defects still remain. All simulations regardless of the amount of water show ceramides hexagonally packed leading to a gel phase structure. The formation of orthorhombic packing was not seen at low hydration in the simulations as in model systems determined via mid-infrared spectroscopy[196]. Once water was added to the bilayer surface the coverage for the lowest level of hydration (2wpl) was 44.56 % as can be seen in Figure 3.10. The percentage coverage increased in a linear fashion as larger numbers of water molecules are added to the surface. At 10wpl the coverage is over 99 % suggesting that the amount of water may be akin to that of bulk water, as no change in the amount of water will increase the coverage to anything significantly higher.

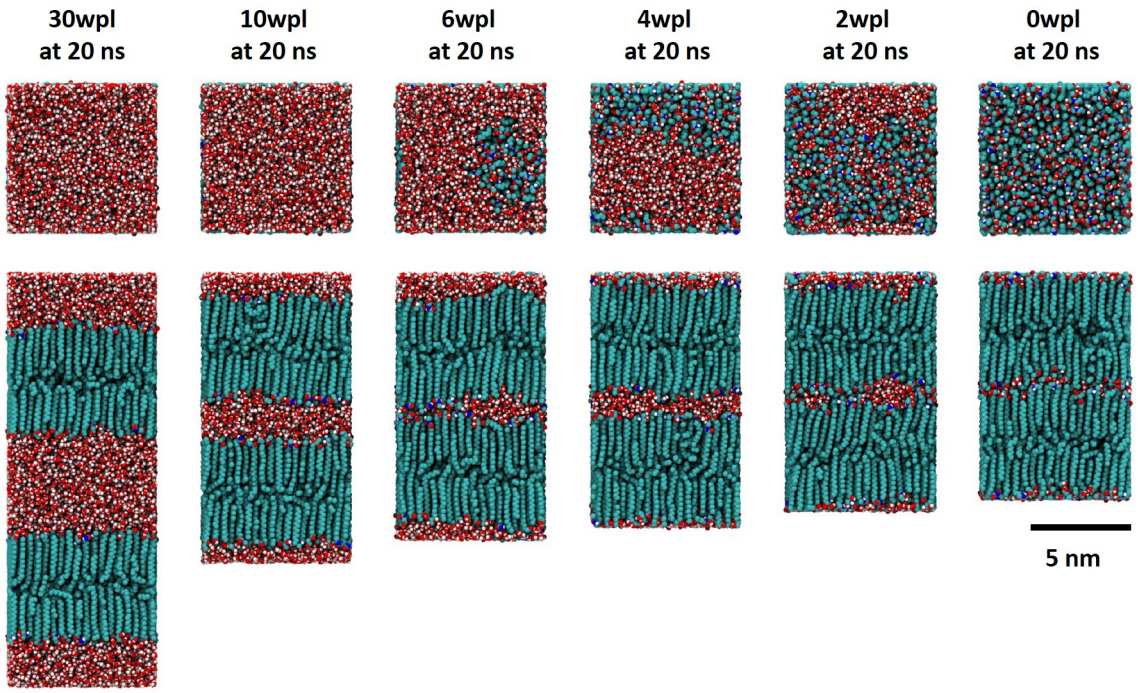

Figure 3.2: Snapshots of each double bilayer system at a different level of hydration are shown at the end of the production run (20 ns). The top graphic shows a top-down view of the bilayer surface. The bottom graphic is a side view of the double bilayer system. Oxygen atoms are shown in red, hydrogen atoms in white, nitrogen atoms in blue, and hydrocarbon tails are coloured cyan.

Analysis of the tilt angle of the C24 chain in Figure 3.3 shows that an increase in hydration level from 2wpl through to 6wpl leads to a decreasing of the tilt angle from $\approx$12.8° to $\approx$11.3°. This reduction in tilt angle suggests that the height of the bilayer in the bilayer normal direction would increase. Upon further hydration the tilt angle starts to increase to $\approx$11.6° indicating a reverse in the height in the bilayer normal direction. The lipid tilt angle could help explain the change in thickness of the ceramide systems. Previous simulations using this forcefield have calculated the tilt angle to be around 10°[35], 13°[204], or 17°[154,156] depending on temperature and hydration which play a significant effect on the packing of the lipids.

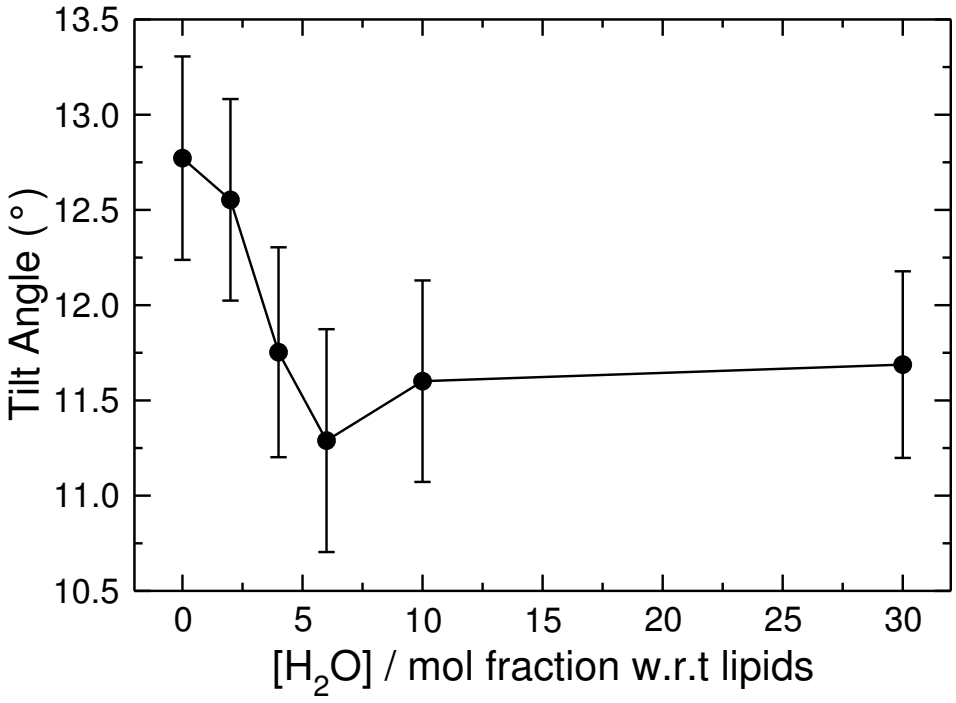

Figure 3.3: Tilt angle of the C24 chain as a function of hydration.

The density profiles of the bilayer systems are shown in Figure 3.4. The profiles are mirrored due to the presence of the double bilayer. Generally all the profiles show similar characteristics. For the greatest hydrated system of 30wpl, there is a flat region corresponding to bulk water leading to a decrease in the density at the interface, where the water interacts with the ceramide headgroups. The density of the ceramides is most prominent at the interface due to the mass of headgroups and decreases as one approaches the center of the bilayer. This low density corresponds to the looser packing of the tail ends. Attributes of bulk water density can also been seen in the 10wpl density profile. It is noticeable in these two profiles that the headgroup density is separated into four distinct peaks, thus indicating a block of water separates them, leading to no head-head interactions. The headgroup density peaks merge at the 6wpl hydration level due to the head-head interactions between opposite bilayers, this behaviour is intensified at 4wpl due to the increased pooling effect at lower levels of hydration. Density of the headgroup peaks decreases inversely with the level of hydration until the 6wpl level. Subsequently the peak density increases as the level of bulk water is achieved.

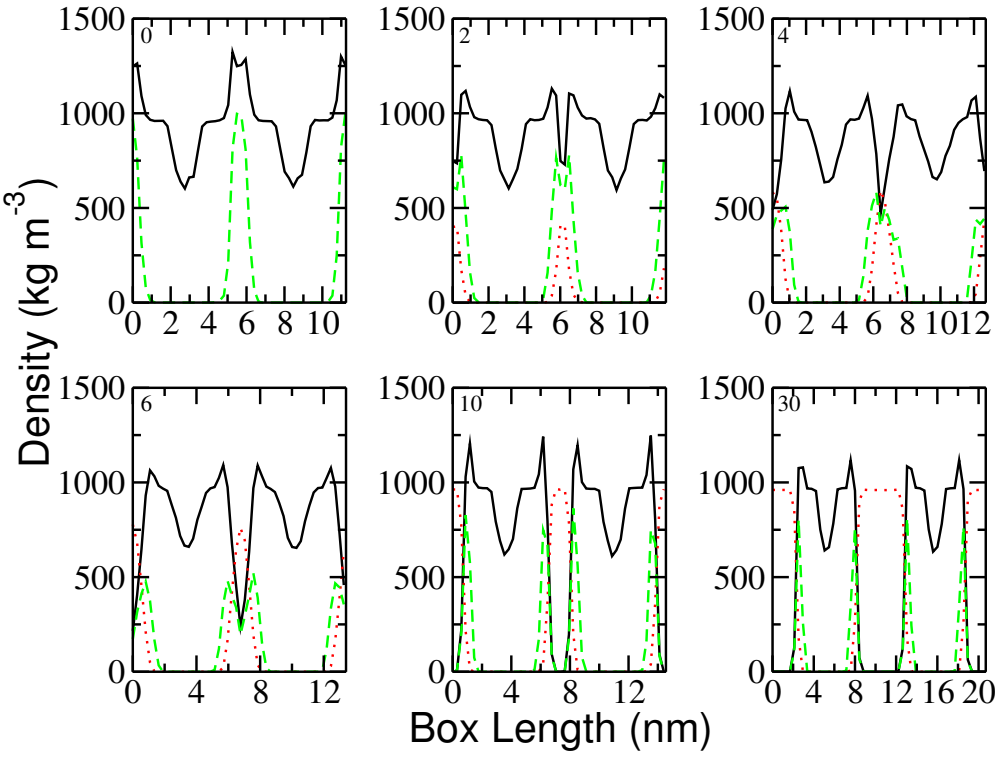

Figure 3.4: Density profiles for double bilayer systems with varying hydration levels. Ceramide density shown in black(solid), headgroup density shown in green(dashed) and water density shown in red(dots).

In these double bilayer systems there are two distinct trends observed in the APL when the level of hydration is varied, seen in Figure 3.5. Low levels of hydration, i.e. the anhydrous bilayers and the lowest amount of water per lipid (2wpl) have similar values for their area per lipid of 39.9 Å^2 ± 0.1 (3s.f) and 39.8 Å^2 ± 0.1 (3s.f) respectively. The next group involves bilayers with moderate or high levels of hydration with values of APL ranging between 39.0 and 39.3 Å^2. The area per lipid decreases as a function of increasing hydration until the 6wpl level is reached. This trend is reversed once the 10wpl hydration level is reached. The APL of the fully hydrated system (30wpl) of 39.3 Å^2 follows close agreement with the experimental values of ∼40 Å^2 determined using X-ray scattering[218], 38 Å^2[31] and 42 Å^2[219] and that of previous ceramide simulations by Das[8](38.9 Å^2) and Papadimitriou[35](38.1 Å^2). The trend of a larger APL with increasing hydration level from around 6 to 30wpl is also observed in simulation studies of phospholipids. Mashl *et al.*[200] observed an increase in APL of DOPC bilayers when increasing hydration level from 5.4 to 11.4 to 30wpl, while similar observations were made by Hogberg and Lyubartsev for DMPC bilayers[199].

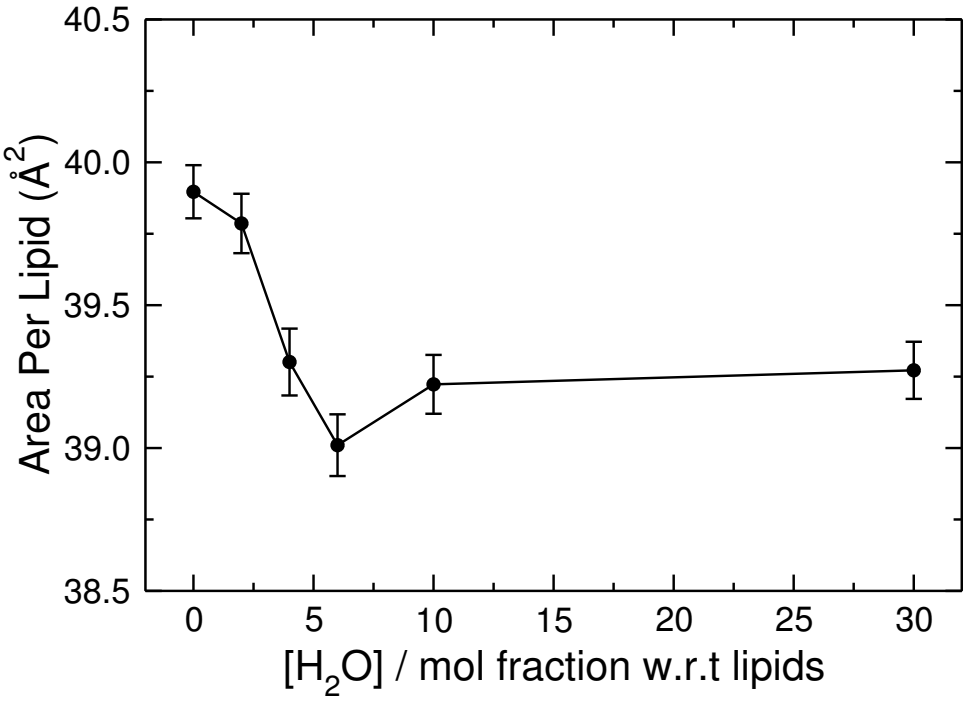

Figure 3.5: Area per Lipid as a function of hydration.

The thickness of the bilayers mirror the trend, Figure 3.6, seen with the area per lipid in that an increase in the level of hydration is associated with a thickening of the bilayer upto 6wpl. A peak thickness of 5.3 nm $\pm$ 0.2 is identified at the 6wpl hydration level. A further increase in the number of water molecules leads to a decrease in the thickness. As the hydration level approaches bulk water the thickness begins to plateau. The thickness calculated here seems to be reasonable in comparison to the bilayer repeat distance of 5.6 nm for dehydrated ceramide NS determined through X-ray diffraction experiments by Shah et al.[30] given that thickness of the headgroup region is added. The values here are larger than the atomistic values of Notman (4.94 nm)[156] and the atomistic and CG values of Sovova (4.9 nm)[9] but smaller than that of Papadimitriou (5.75 nm)[35] and Das (5.71 nm). The variation in values could be attributed again to different temperatures and lipid composition. Another factor could be the methodology used in determining these values; headgroup distance, water density as a function of bulk water or via bilayer volume. This trend of a decrease in membrane thickness after 6wpl is observed for phospholipids such as DOPC[200], POPC[201] and DMPC[199] is simulations studies of varying hydration.

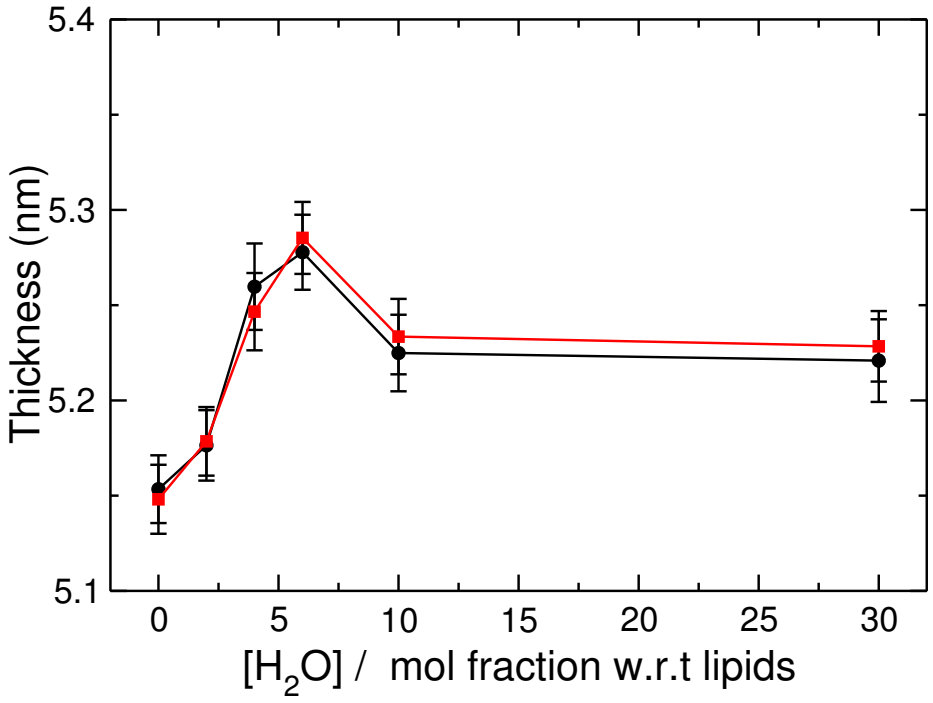

Figure 3.6: Bilayer thickness as a function of hydration. Upper bilayer shown in black and lower bilayer shown in red.

The ceramide NS has two hydrocarbon tails and by calculating the order parameters a measurement of the alignment of these chains in the bilayer can be obtained. The order parameters of atoms in each chain are shown in Figure 3.7. The order parameter profiles for all the bilayers are qualitatively similar, with a lower overall ordering of the C24 chain compared to the C16 chain. There is a high degree of disorder for atoms in the chain closer to the interface but a higher degree of order going down the chain. This decreases again towards the center of the bilayer where a more fluid like region is found. Between 0wpl and 6wpl, as the level of hydration increases the order of the chains also increases for the first 15 atoms of the chain. There is no difference in the order parameters of the lower half of the chains due to changes in hydration as we approach the bilayer center. For the atoms that are closest to the headgroup and the interface, i.e C atoms 1-4, higher order is seen as the amount of water is increased. As we move down the chain it becomes clear that the 6wpl hydration level is the most ordered follow by 30, 10, 4, 0 and 2wpl, in that order. Ordering in the tails, as the bilayer mid-plane is reached, is significantly reduced and the level of hydration does not impact the order parameter. A similar trend is seen in the C16 chain, although for the most ordered atom the series follows 6, 10 , 4, 30, 2, 0wpl. Ceramide order parameters are significantly higher than their phospholipid counterparts due to being in the gel phase but systematic ordering in the chains upon dehydration of the bilayer is a clearer trend observed in simulations of DOPC[200] and DMPC[199].

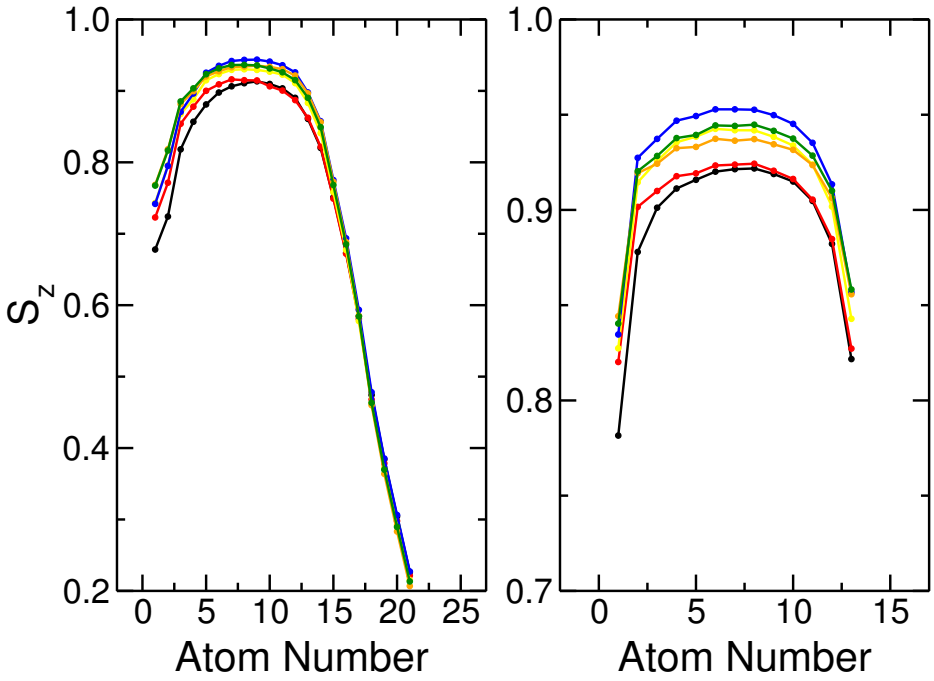

Figure 3.7: Order parameters for the C24 chain (left) and the C16 chain (right). 0wpl in black, 2wpl in red, 4wpl in yellow, 6wpl in blue, 10pl in orange and 30wpl in green.

The strong barrier properties of the stratum corneum are believed to be caused by the lateral hydrogen bonding network between adjacent ceramides[16]. Therefore, if we want to improve our understanding behind this and modify the barrier for various applications, we have to understand how this hydrogen bonding occurs and whether or not a change in hydration level affects the number or type of hydrogen bonds.

We first examine the number of ceramide-ceramide hydrogen bonds. The breakdown of lateral and perpendicular ceramide-ceramide hydrogen bonds and those between ceramide and water are shown in Figure 3.8. An initial decrease in the lateral hydrogen bonds between adjacent ceramides is observed upon the addition of water to the anhydrous system. Further increases of hydration do not lead to any significant change in the number of lateral hydrogen bonds. It is clear that an increase in the hydration level causes an decrease in the number of perpendicular hydrogen bonds between ceramides on opposite leaflets. Conversely an increase in the amount of water increases the number of hydrogen bonds with ceramides until bulk water is reached where upon it plateaus. At this level the ceramides are saturated in this current structure. In simulations of DPLC bilayers, an increase in hydration level lowered the number of water-lipid hydrogen bonds[202]. The total number of hydrogen bonds per lipid increases from the 0wpl to the 2wpl level and only by a small amount therein after. Once the amount of bulk water has been reached, there is no further change in the total amount.
The hydrogen bonds with each functional group was sliced into its lateral and perpendicular components, as well as it's interactions with water, Figure 3.8, where FG1(C16:H18), FG2(C20:H22), FG3(N23:H24) and FG4(C25:O26) are the headgroup functional groups. We can see that the number of hydrogen bonds for both FG1 and FG2, the hydroxyl

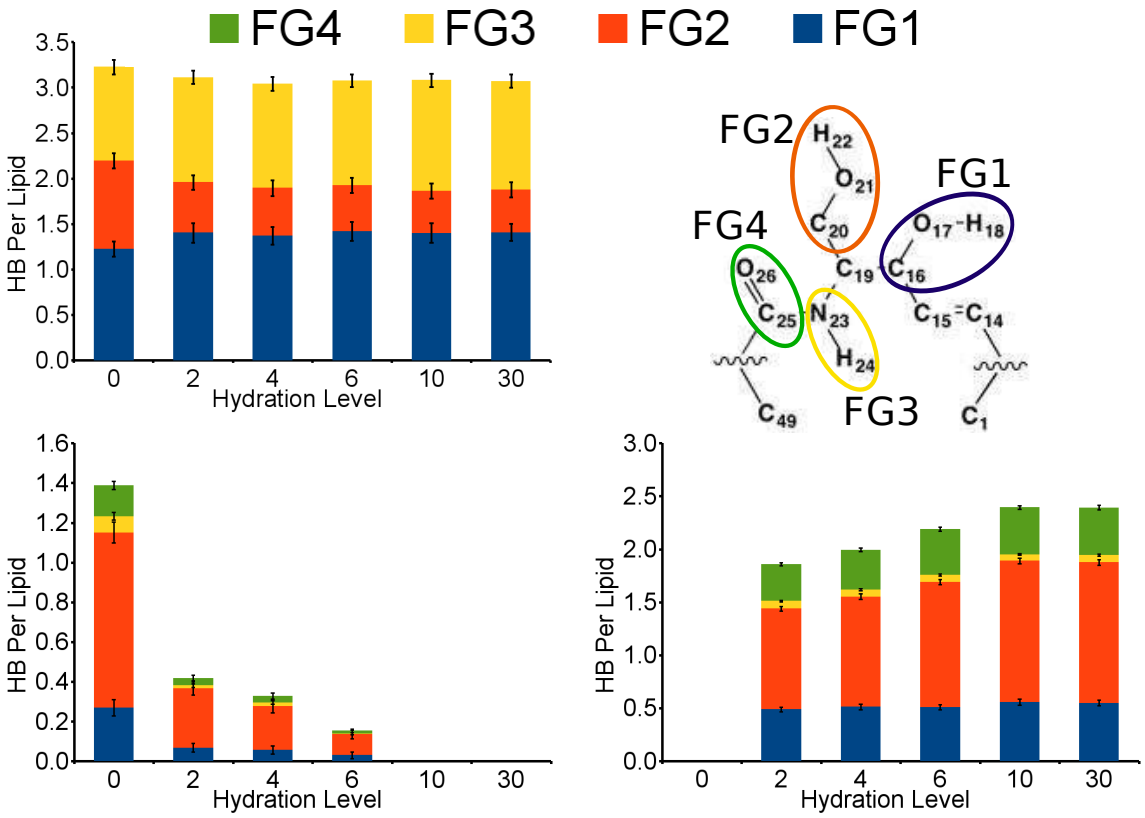

Figure 3.8: Hydrogen bonds as a function of hydration level with respect to lateral ceramides (top left), perpendicular ceramides (bottom left) and water (bottom right).

groups, increases as a function of hydration until it reaches the bulk level of water where an increase is no longer seen. There appears to be no significant difference to the amount of hydrogen bonds regarding hydration level for FG3. For FG4 we observe an increase from the 2wpl level to 6wpl and then a slight increase as we approach full hydration, although this is not statistically significant.

For the lateral component, FG1 increased when water is added to the anhydrous system. There is no change upon further hydration. The opposite can be seen for FG2, where an initial decrease is seen. This continues upon the addition of water although they are within error. FG3 follows the same initial trend but does not change after any further increase in hydration level.

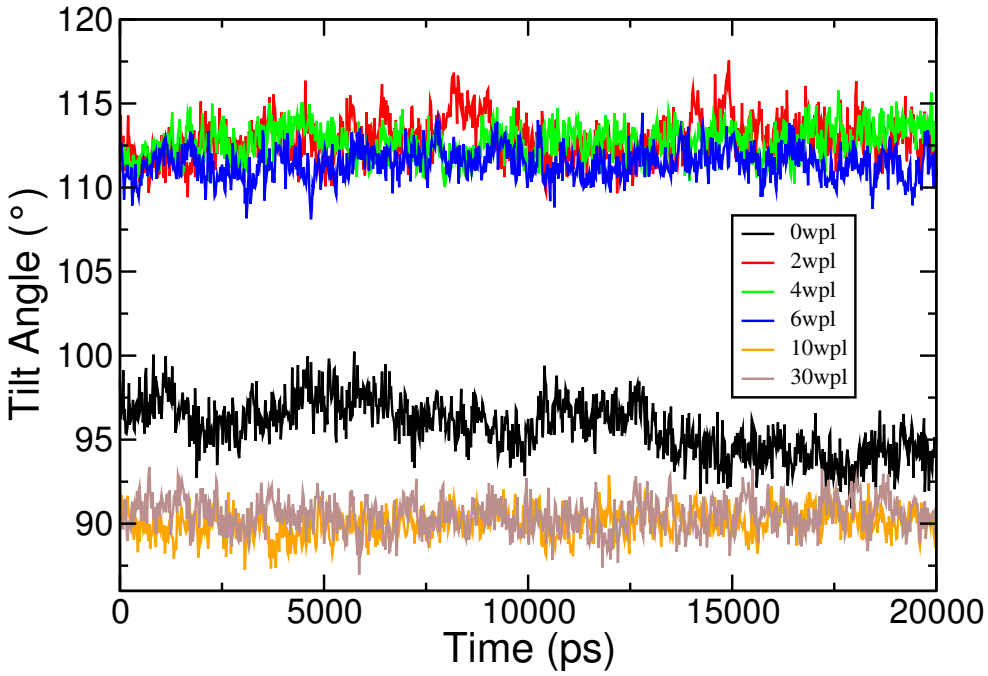

Figure 3.9: COH tilt angle over time as a function of hydration.

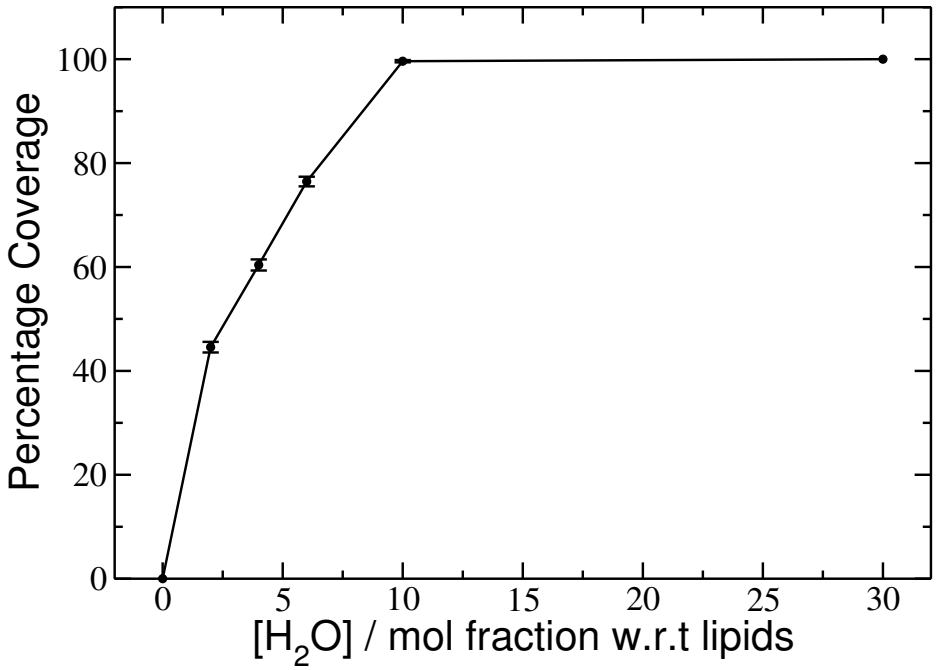

Figure 3.10: Percentage of the bilayer surface covered with water molecules as a function of the hydration level.

3.4 Discussion

Although we observe alteration in the structural properties of the ceramide bilayers, such as the APL, thickness, order, chain tilt and hydrogen bonding through the addition of water, the mechanism in which these occur has not yet been described. We consider packing, headgroup arrangement and conformational effects in trying to explain these structural changes.

First off it is reasonable to assume that any effect on the tilt angle of the hydrocarbon chains is directly affected by the ordering of the headgroups. We first calculated the radial distribution function (RDF) of the centre of mass (COM) of the ceramides in a single leaflet to determine the packing. A number of well defined peaks can be seen in Figure 3.11 for all levels of hydration. The clear primary and secondary peaks are a strong indication of the hexagonally packed structure we expect to see with gel-phase ceramides. This is confirmed in our observations by looking at a top down snapshot of the COM of the ceramides for each hydration level. We do not see signs of an orthorhombic phase in any of our simulations or through analysis of the RDF. The first peak shows the relative probability of finding a lateral ceramide as its nearest neighbour, the highest g(r) values can be seen for the 30 wpl hydration level and can be seen to scale down as the level of hydration is reduced. The secondary peak follows a similar trend with fully hydrated levels (30 and 10 wpl) with large g(r) values, the medium hydration levels (6, 4 and 2 wpl) having lower values and the anhydrous bilayer having the lowest value. This suggests that higher levels of hydration lead to an increase in order and closely follows that of the tail order parameters. Both the primary and secondary RDF peaks are of similar magnitude which again show the strong order of the ceramides which can be attributed to a combination of lateral and water hydrogen bonds. We can conclude that a change in hydration doesn't alter the phase of the lipids but can lead to a stronger ordering effect on the headgroups.

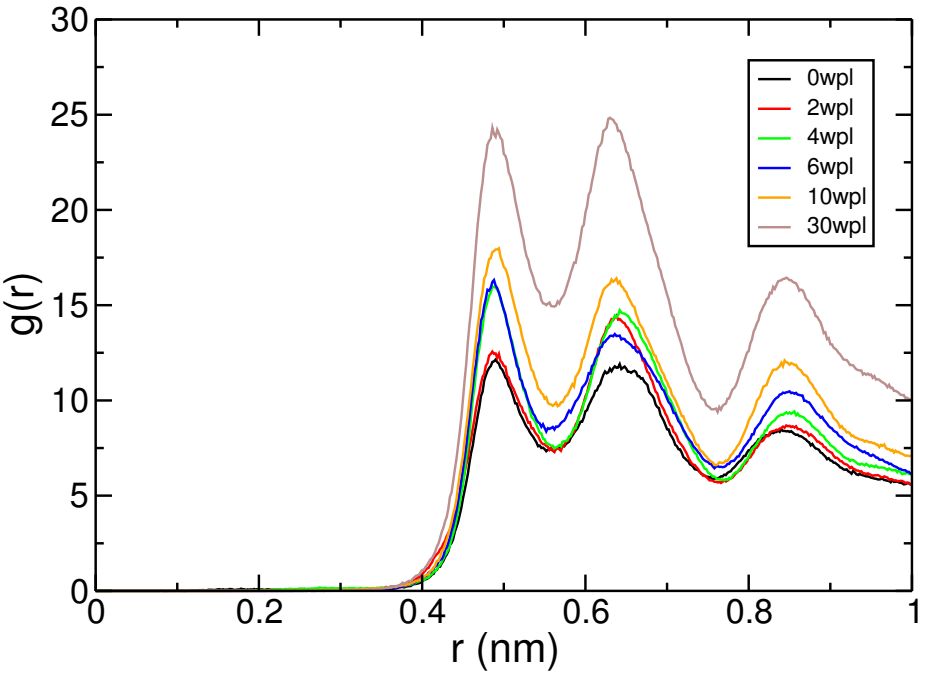

Figure 3.11: Radial distribution function of the centre of mass of ceramides as a function of hydration.

The addition of small amounts of water to ceramide bilayers can lead to a pooling effect at the interface. These pools can perturb the surrounding bilayers and one must wonder how this alters the headgroup arrangement. We have calculated the headgroup widths from the density profiles seen in Figure 3.12. The headgroup widths increases as a function of hydration from the anhydrous bilayer to the 6 wpl hydration level. Some ceramide headgroups are raised up from the interface to form hydrogen bonds with the pools of water thus leaving a greater distribution of headgroup widths. A narrow distribution is seen at the 10 wpl hydration level when the whole surface has been evenly covered but is greatly increased at the 30 wpl level when the ceramides are trying to saturate all of their hydrogen bonds. As a result of some ceramides rising above others, unfavourable interactions between headgroups and upper hydrocarbon tails can occur, not to mention gaps opening up for water molecules to permeate. To avoid both these steric clashes and hydrophobic penalties, the tilt in the tails is reduced to allow for slightly better packing thus preventing any possible water permeation. We believe this hydrophobic driving force is one of the contributors in changing the hydrocarbon chains' tilt angle, causing a knock on effect to the APL and thickness. Another possible contribution to this change in tail tilt angle is through a change in tilt of the headgroup. In Figure 3.13 we can see the customary increase in tilt angle to 92.830° upon the initial addition of water but further hydration leads to a retraction back to 89.845°. This small change in the headgroup tilt matches that of the tails, it is possible that the hydrophobic effect causes a rotation of the ceramide molecules.

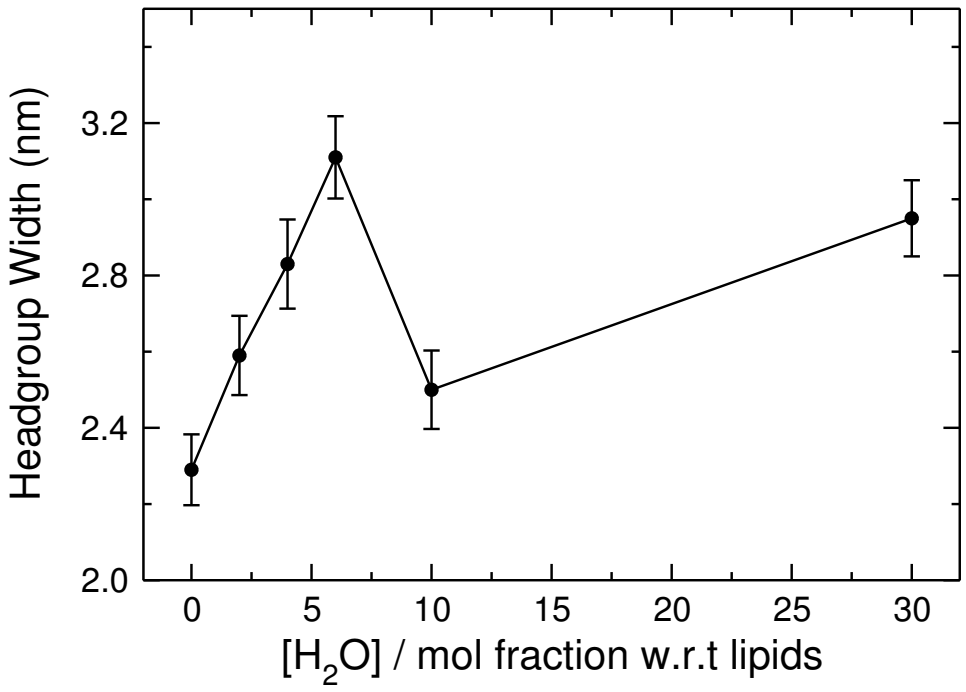

Figure 3.12: Headgroup widths as a function of hydration.

The final possible contribution to the structural modifications of the bilayers could be some form of conformational change. As the hydroxyl group, FG2, was the functional group that obtains the most hydrogen bonds through interactions with perpendicular ceramides and water, it is most likely the functional group to cause a change in the APL. We again calculated a tilt angle between the C20-H22 vector and the z axis, see Figure 3.13. There is a significant change in the angle when water in added to the system. The O21 and H22 stick up higher to try and gain a greater number of HBs leading to an increase in water hydrogen bonds and a decrease in perpendicular hydrogen bonds. Further hydration leads to a decrease of a 90° angle. There is now an optimal arrangement between the hydroxyl groups where they can create a high number of hydrogen bonds while avoiding a steric clash with one another.

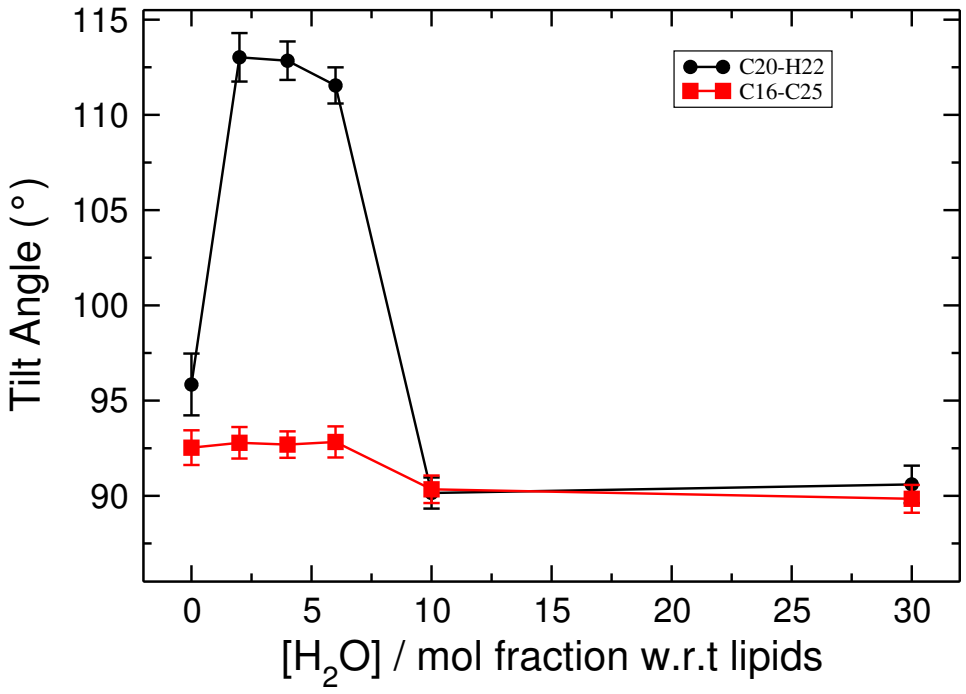

Figure 3.13: C20:H22 Tilt Angle as a function of hydration in black. C16-C25 Tilt Angle as a function of hydration in red.

The effects of hydration on the resulting properties for each bilayer system have been identified and are all inexplicably linked and affected by each other. For example, the tilt angle has a direct impact on the area per lipid of the system. As the tilt angle is decreased the distance of the ceramide in the bilayer normal direction will increase as a result. The area in which the lipid now occupies will have decreased, which is what is observed as the hydration level is increased from the anhydrous system to 6wpl. Due to the lack of interdigitation observed in our systems, the dominant factor for the change in the thickness is the affect of the tilt angle on the bilayer normal distance of the ceramides. Each of these properties are dependent on the others.

The high degree of disorder at the interface is a culmination of hydrogen bonding both between and within the leaflets and the headgroup interactions with water. As the interactions between the atoms of the ceramide molecules diminish as we navigate away from the interface and the volume in which they can rotate decreases, a more compact and thus ordered system arises. A higher degree of disorder at the bilayer midplane corresponds with a more fluid like region which is observed. The increase in order of the chains in line with the increased hydration level is consistent with the decrease in the area per lipid. A higher degree of order is akin to a more compact headgroup arrangement which in turn leads to a lower area per lipid value.

We first examine the number of ceramide-ceramide hydrogen bonds, Figure 3.8, where the total number of ceramide-ceramide hydrogen bonds includes lateral (between ceramides in the same layer) and perpendicular (between ceramides on different layers). As the level of hydration increases in the system there is an decrease in the number of

hydrogen bonds between ceramides. At hydration levels of 30wpl and 10wpl there is no change in the number of hydrogen bonds due to bulk water between the two bilayers in the system, therefore no perpendicular hydrogen bonds between ceramides are seen resulting in only the lateral ceramide hydrogen bonding network counting towards the total. The number of interactions increases as the amount of water molecules between the bilayers are reduced. Decreasing the hydration from 6wpl through to 2wpl there is an increase in hydrogen bonding accredited to the perpendicular ceramide-ceramide interactions. This effect is made more prominent by the fact that water molecules do not form a uniform layer at these levels of hydration. Instead, pools of water molecules are found to form resulting in areas where ceramides on one bilayer can interact with ceramides on another bilayer. This is further clarified by the large amount of hydrogen bonds seen when no water between the bilayers is present.

Looking at the hydrogen bonding between ceramide and water also in Figure 3.8, we see that as the level of hydration increases naturally the total number of ceramide-water hydrogen bonds also increases. It is noticeable that the number of hydrogen bonds is the same for both 10wpl and 30wpl. It can be assumed that there is a maximum number of hydrogen bonds that the ceramides can form with water, and this maximum is reached when the number of water molecules equates to bulk water. In this case it can be seen that both 10wpl and 30wpl can be classed as having bulk water, whereas the hydration level below (6wpl) is not quite on the level of bulk water. Combining the number of hydrogen bonds of ceramides with both ceramides and water allows us to determine the total number of hydrogen bonds that ceramides contain within the system. Overall this increases with greater levels of hydration, due to the gain of ceramide-water hydrogen bonds outweighing the loss of ceramide-ceramide interactions, but plateaus upon saturation of the system at 10wpl.

As the barrier properties of the SC are known to be due to the strong lateral hydrogen bonding between ceramide headgroups, it is paramount to study these interactions and understand their role with and without hydration. There is a significant difference in the number of hydrogen bonds between perpendicular leaflets on different bilayers in the anhydrous system and this rapidly decreases as more water is added to the system leading to no ceramide-ceramide interactions between perpendicular bilayers once bulk level water has been reached. There is also a noticeable difference in the number of hydrogen bonds between ceramides in the same leaflet in the anhydrous system compared with other systems that contain water. Further addition of water molecules does not seem to significantly affect the total hydrogen bonds between ceramide headgroups indicating that water lacks the capacity to penetrate the interface. Essentially the bilayer keeps its strong lateral hydrogen bonding network regardless of the addition of water. The small headgroups of the ceramide lipids are packed tight enough so that no water can effectively penetrate this lateral network and affect the hydrogen bonding between ceramides in a decisive manner. The hydrogen bonds lost from both the lateral and per-

pendicular ceramide-ceramide interactions only accounts between 30 and 50 percent of the gained ceramide-water hydrogen bonds. This suggests hydrogen bonding between the headgroup and water is energetically more favourable than competing headgroup-headgroup interactions.

The extent of hydrogen bonding of each functional group of the ceramide head was determined with respect to water, Figure 3.8. Of the four major functional groups on the ceramide headgroup, it is the hydroxyl groups that acquire the greater number of hydrogen bonds with water, mainly due the placement of these groups on the head they have greater flexibility and can extend out to interact with the solvent while the oxygen of the amide group acquires a greater number of hydrogen bonds than the nitrogen group. An increase in the hydration leads to a general increase in the total hydrogen bonds of the hydroxyl and the nitrogen of the amide functional groups. Where as there is no significant change in the number of hydrogen bonds of the oxygen of the amide group with water.

Small-angle X-ray scattering (SAXS) experiments of a range of hydrated samples of SC (6% to 60% w/w) shows there is no change in the position of the main diffraction peak but there is a small shift in the top of the peak for the fully hydrated 60% w/w level[26]. No swelling of the bilayers occurs and so the repeat distance remains fixed. It is believed that only small amounts of water are in the bilayers and the majority of it is absorbed by the corneocytes. Hence, the simulations of low levels of hydration here are of particular interest. Increase in the hydration led to stronger ordering which follows the general trend seen in these simulations. Although no change of phase was observed in these simulations, Infrared spectroscopy of low hydrated membranes has shown the possibility of a change to an orthorhombic phase[196]. Both dry and hydrated states have different repeat distances according to Ramen spectroscopy of CER [AS][198].

Simulation studies of varying hydration in phospholipids share some similar trends, notably the decrease in APL as hydration is decreased[200,201,220]. This also results in a thicker bilayer, less water molecules are located in the headgroup region and so the lipids can form a more ordered conformation indicated by a smaller APL, this smaller area results in the tails having to adopt a more extended conformation. The change in APL and thickness are less pronounced in ceramides than phospholipids as there will be less water below the headgroup due to strong lateral hydrogen bonding network between lateral ceramides. Hogberg also showed that the change in headgroup tilt may be related to the change in APL for DMPC bilayers, while Mashl *et al.*[200] calculated that the headgroup of DOPC becomes parallel to the membrane by roughly 3° when the hydration level is lowered.

3.5 Conclusions

By analysing ceramide NS simulations with varying hydration we have shown that the water content within the lipid matrix is an important component in determining the barrier properties of the SC. The change in hydration level has a direct impact on the bilayer conformation and thus its structural properties. Most noticeably at low levels of hydration a pooling effect of water can be seen on the surface of the bilayers. These localized pools of water, tilt the headgroup and alter the conformation of the hydroxyl groups. This ultimately affects the packing of the lipid tails, especially the tilt angle. As the properties of the chain tilt are related to the APL and the thickness, it can be shown that small changes to packing can affect all the properties of these bilayer systems. Regardless of the level of hydration the lateral hydrogen bonding network still plays a pivotal role in preventing the permeation of water molecules through the bilayers although diminishing perpendicular hydrogen bonds are replaced with those with water, increasing the total number of HBs when approaching saturation. This work helps to provide a more detailed insight into how the SC prevents dehydration at the molecular level so improved skin care products can be produced to help treat skin disease.

Chapter 4

Effect of Oleic Acid on the Permeation of Water through Model Skin Lipid Bilayers

4.1 Introduction

The lipid composition of a membrane determines its physiochemical properties such as its structure, dynamics, mechanical properties and permeability. One can alter the composition to modify its properties to fit a specific need, for example to enhance the permeability of the membranes for topic drug release[51,55,56,66,221–224]. As described in Section 1.2.6 the major lipid components of the SC are CERs, FFAs and CHOL. The FFAs are of particular interest, as they have significant influence on the packing and thus the structural properties of the membranes. Fatty acids are generally saturated in the SC, although some unsaturated species such as OA and linoleic acids have been found at low concentrations[225]. These unsaturated FFAs have known therapeutic properties and are commonly used as penetration enhancers for drug delivery[51,53–56], reduction in cardiovascular disease and tumours[58–62].

The effects of OA on phospholipid membranes have been studied on many occasions. OA has been shown to have a small fluidising effect on DPPC bilayers by decreasing the gel-to-liquid crystalline phase transition temperature by a couple of degrees[57,63]. Other experiments on DPPC bilayers show that OA disturbs the packing of the acyl chains[64] and there is evidence of OA-DPPC phase separation at high surface pressures in DPPC/OA monolayers[65]. Phase separation has also been observed in gel phase DPPC bilayers at high concentrations of OA[63]. Notman *et al.*[78] tested various OA concentrations on DPPC bilayers to determine the effect on the permeability. It was shown there was no variance of the chemical potential as a function of increasing amount of OA but the number of water permeation effects doubled for larger concentrations. It was determined that OA weakens interactions between headgroups leading to a small increase in the permeability of water. They concluded that any effects of OA on the

structure of the bilayer are likely to be subtle rather than large perturbations, although it is acknowledged that the effects may be more prominent in gel phase structures such as the ceramides in the SC. It was observed by Peters *et al.* that OA and its analogues alter their positions in fluid DMPC bilayers depending on their protonation status[81] and thus may have an effect on the structure. These structural effects are attributed to the kinked structure found in *cis*-OA *via* an unsaturated double bond. To explore the effects of saturation Leekumjorn *et al.*[82] used MD simulations of saturated and unsaturated fatty acids, including OA, within fluid DOPC. It was shown that that the unsaturated fatty acids are able to reduce the lipid ordering within the membrane and thus increase its fluidity. In contrast, the saturated fatty acids promoted a closer packing of the bilayer tails.

Interactions of OA may of course be different in the SC than in phospholipid bilayers due to the chemistry of the lipids and their resulting phase behaviour. As a result there has been an increase in the number of studies investigating the effects of OA on SC lipid models to develop therapeutic uses in industry. It is known that OA lowers the gel-to-liquid crystalline phase transition temperature of the SC[51,54,66] and below this OA exists as a separate phase. Reduction of this transition temperature leads to an increase in permeation[67] and it has been hypothesised that this is facilitated by the kinked structure of OA and its disruption of lipid packing, as previously mentioned. Hoopes *et al.*[79] studied these structural effects by modelling mixtures of CER NS, lignoceric acid and CHOL with varying concentrations of OA at 300 and 340 K. Upon addition of OA, both the interfacial and midplane densities, the thickness in the hydrophilic interface at 300 K and the overall thickness at 340 K were reduced. This is due to the interdigitation that coincides with the temperature increase but happens regardless of the OA. OA did not have a significant impact on the hydrogen bonding of the CERs but introduced greater ordering of the non-hydroxyl fatty acid of the CER just below the headgroup. Dynamical properties such as the diffusion of CHOL can be seen to increase as a function of OA. These findings were enhanced most recently by Akinshina and colleagues[80] through their investigation of the effects of unsaturation using MD simulations of differing concentrations of natural fatty acids with CER NS bilayers. Mixed CER and saturated oil bilayers remained stable even with high oil concentrations. Low oil concentrations lead to rigid bilayers due to better packing and a transfer of hydrogen bonds from lipid-water to lipid-lipid. Oils with unsaturation, such as OA, lead to instability of the bilayer structure at concentrations greater than 50%. The concentration required for this breakdown decreases as the number of *cis*-double bonds increase. With instability in the bilayer comes greater permeability.

It has been hypothesised that a possible mechanism for the enhanced penetration of small molecules is that OA fluidises the SC lipid membranes. It is thought that the introduction of OA into the membrane disrupts the packing and thus induces interdigitation which causes a reduction in the bilayer thickness. Any defects at the interface

caused by the OA could result in a weakening of the barrier to penetration[67,68]. Alternatively if phase separation does occur, permeants could directly diffuse through this OA layer. Despite the growing literature in this area, these hypothesis for the mechanism in which OA enhances penetration have not been fully examined. Therefore, in this study we analyse the various possible pathways in which a water molecule, can permeate through model membranes of SC lipids with the aid of OA and deduce which pathway is most likely through the use of Potential of Mean Constraint Force calculations. Three different pathways will be examined here: through a pure CER bilayer; through a pure OA bilayer; and through a mixed bilayer containing a 9:1 ratio of CER to OA. This molar ratio is consistent with topical penetration enhancers for pharmaceuticals[226]. As a result we hope to elucidate the mechanism of action of OA for enhanced penetration through structural analysis. Through the understanding of the mechanism of action one can design a more efficient drug delivery strategies.

4.2 Computational Methodology

4.2.1 Initial Configurations of the Bilayers

A configuration of an equilibrated pure hydrated ceramide bilayer at 100 ns was taken from our previous work[163] and used as the starting configuration for the steered MD simulation, where a water molecule is pulled from the bulk into the bilayer. The purpose of the steered MD simulation was to generate starting configurations for the PMCF free energy calculations. A pure OA bilayer was produced by replicating an OA molecule in the x and y directions, creating a 12×12 grid. This leaflet was then reflected in the xy plane to generate a 288 OA bilayer. Water was added above and below the bilayer to produce the same water per lipid ratio (30.2:1) as in the pure CER bilayer. The structure was energy minimised and equilibrated in the NPT ensemble, first with position restraints on the OA and then with them removed. A further 20 ns NPT run was carried out to ensure all the bilayer properties had reached equilibrium. The mixed system was produced by surrounding an OA molecule with ceramides to create a unit cell with a 9:1 ratio of CER:OA. This was replicated in the x, y and z directions to generate a bilayer containing 160 lipids. The resulting structure was energy minimised and a 5 ns NPT simulation with position restraints of 1000 kJ mol^{-1} on the ceramides was performed so the OA could equilibrate themselves within the CER bilayer. Next solvent was added above and below the bilayer in the same solvent to lipid ratio as before. Further energy minimisation and NPT ensemble simulations followed to equilibrate the water around the bilayer. A further 20 ns NPT run was made to ensure all the bilayer properties had reached equilibrium. The contents of each system can be found in Table 4.1.

System Contents				
System	CER2	OA	SOL	Total atoms
Pure CER	288	0	8696	40200
Pure OA	0	288	8696	32136
Mixed	144	16	4830	21882

Table 4.1: Molecular contents of Systems

4.2.2 Forcefield Parameters

The potential energy function and interaction parameters employed for the CER were based on the united atom forcefield of Berger[34], which was originally parameterized for phospholipids and uses GROMOS87 parameters for headgroups and specially adapted parameters for lipid tails. This forcefield is described in Section 2.2.9 and in detail in our previous works[156]. The forcefield parameters for the OA tails were also taken from Berger[34]. The water was modelled using the SPC potential[164].

4.2.3 Simulation Parameters

Simulations were carried out in the *NPT* ensemble using the GROMACS package[165], and employed the Nosé-Hoover thermostat[96] coupled separately to the lipid and water molecules with a time constant of 5 ps and a Parrinello-Rahman barostat[98] with a time constant of 5 ps and compressibility of 4.5 x 10^5 bar^{-1} for semi-isotropic pressure coupling. The simulation cell was kept orthogonal by setting the off-diagonal terms of the compressibility matrix to zero. Standard periodic boundary conditions were applied in all three directions. All bonds were constrained using the LINCS algorithm[104] and the time step was 1 fs. The LJ interaction cut-off was 1.2 nm using a shift function. PME summation was used for the electrostatics with a cut-off of 1.4 nm for the short range part of the calculation. Results were analysed using the GROMACS package[165] and MEMBPLUGIN[216] in VMD[217].

4.2.4 Free Energy Theory

To calculate the permeability coefficient of water in each of our bilayer systems, the PMCF method was used. This method is described in detail in Section 2.6.2. This method has been used previously to calculate the permeability of water through hydrated[45,163] and dehydrated[214] skin lipid bilayers. As well as seeing use to calculate the permeabilities of water and other small moelcules in numerous other bilayer studies[8,41,42,49,107,107]. In this method the permeant, a water molecule in our case, is constrained *via* the COM at a given height z in the bilayer (where z is the direction of the bilayer normal) and allowed to freely move in the xy plane. For each step, the equation of motion is calculated and then the coordinates of the permeant are corrected to satisfy the distance constraint between the COM of the permeant and the bilayer. The

force F_i required to maintain the constraint is calculated at each MD step and can be used to calculate the free energy. This method has been used and explained in depth in various of bilayer studies[8,41–43,107].

4.2.5 Free Energy Calculations

From the final equilibrated bilayer configurations, a water molecule from the bulk water was selected at random and pulled along the z direction at a rate of 0.01 nm ps^{-1} with a force constant of 1000 kJ mol^{-1} nm^2 towards the bilayer midplane. At every 0.2 nm separation along the bilayer normal, the configurations of the water molecule are saved. Each of these configurations were evolved for a minimum of 10 ns, with the selected water molecule constrained at its fixed z separation from the midplane. To compute the diffusion coefficient of the water, the simulations were extended for 500 ps where the F_z was collected every 0.001 ps. This procedure was replicated an additional time for the pure CER system and an additional two runs for the pure OA bilayer and the mixed system, with different initial xy coordinates of the permeating water each time. The permeability coefficient, P, can be calculated from the free energy profile and the diffusion coefficient. In this work, the permeability of water along the bilayer normal z was assessed for three different systems, pure CER, pure OA, and a mixed CER/OA bilayer.

4.2.6 Analysis

Structural Properties

Area per lipid, density profiles, lipid tail order parameters and numbers of HBs were calculated using the methods described in Section 3.2.4. In this case averages were computed over last 10 ns of the trajectory.

Bilayer Thickness

The CER bilayer thickness was calculated by computing the density profile of the N23 atom in the CER headgroup and by taking the distance between the peak N23 atom densities. The OA bilayer thickness was calculated by taking the distance between the peaks in the carboxylic oxygen atom density profile. The thickness of the mixed CER/OA bilayer was calculated by taking the distance between the peaks of the combined CER nitrogen and OA carboxylic oxygen atom density profile.

Lateral Diffusion Coefficients

The lateral diffusion coefficients were calculated using the Einstein relation from the g-msd tool in GROMACS[165].

4.3 Results

4.3.1 Structural Properties of the Bilayers

The focus of this work is on the permeation pathway of water through the SC lipid lamellae and to study the effect of OA on the barrier properties of the SC. However in order to validate the models used and to provide molecular level insights into the properties of the bilayer we first characterise the structural and dynamic properties of the bilayers and compare them with existing experimental data.

Observations

Snapshots of each system after equilibration are shown in Figure 4.1. A hexagonally packed gel-phase is seen for the pure CER system, while the pure OA is in a crystalline phase. In the mixed system there are no visible structural changes to the bilayer and the lipid tails remain in a well ordered gel phase. No water penetration is seen in any of the systems. No phase separation is observed in the mixed system and the OA tails align well with the CER tails in the bilayer normal.

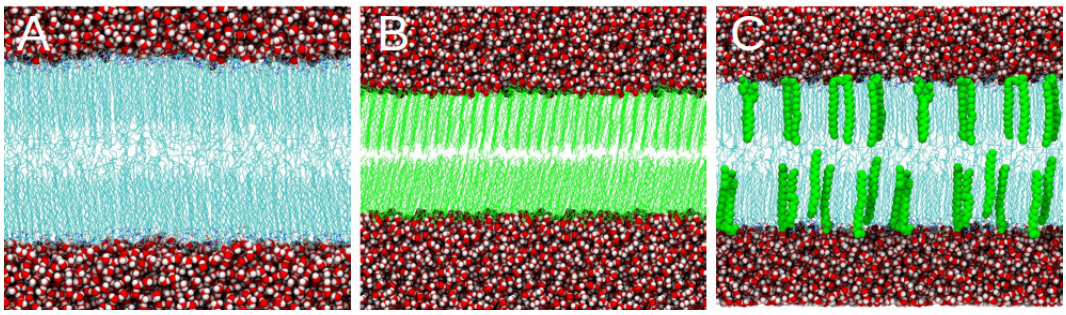

Figure 4.1: Pure CER system (A), pure OA system (B) and mixed CER/OA (C) all surrounded by water. CER chains coloured cyan, OA chain coloured green, nitrogen atoms in blue, oxygen atoms in red and hydrogen atoms in white.

Area per Lipid and Thickness

From Table 4.2, the APL of the CER system of 39.0 Å^2 follows close agreement with the experimental value of ∼40 Å^2 determined using X-ray diffraction[218], CER simulations by Das[8] of 38.9 Å^2 and previous simulations in Section 3.3. The OA system has a much smaller APL at 22.3 Å^2 compared to the CER, due to a smaller headgroup and only a single tail. The mixed system has a reduced APL compared to the pure CER. The APL predicted for the mixed system for ideal mixing is 37.2 Å^2 therefore the APL of 37.5 Å^2 from the mixed simulation indicates that there is a small expansion of the bilayer area due to the interaction of CER and OA. The thickness of the pure CER system at 5.1 nm matches that of experimental studies and previous simulations. The pure OA system has a thinner bilayer at only 4.5 nm due to a shorter chain length compared to CER. In the mixed system the CER thickness does not change but the

OA thickness increases in length. The OA tail could be forced into a more extended conformation to pack efficiently with the CER bulk.

System	APL / Å^2	Thickness / nm
Pure CER	$38.968 \pm 1 \times 10^{-3}$	5.1
Pure OA	$21.614 \pm 2 \times 10^{-3}$	4.5
Mixed	$37.537 \pm 2 \times 10^{-3}$	
(CER)		5.1
(OA)		4.9

Table 4.2: Structural properties of pure CER, pure OA and mixed CER/OA bilayers.

Density Profiles

The density profiles of the bilayer systems are shown in Figures 4.2, 4.3 and 4.4. Generally all the profiles show similar characteristics. There is a flat region corresponding to bulk water leading to a decrease in the water density at the interface, where the water interacts with the CER and OA headgroups. No water is found inside the bilayer in any of the three systems. The density of the lipids is highest at the interface due to the dense packing compared to the tails and decreases as one approaches the center of the bilayer. This low density area corresponds to the looser packing of the tails and interdigitation at the midplane for the CER system.

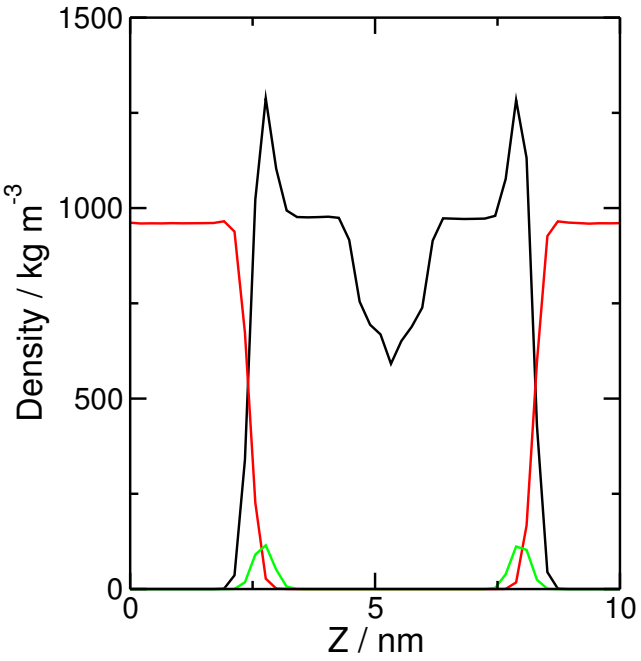

Figure 4.2: CER system density profile; CER in black, water in red and N23 atoms in green.

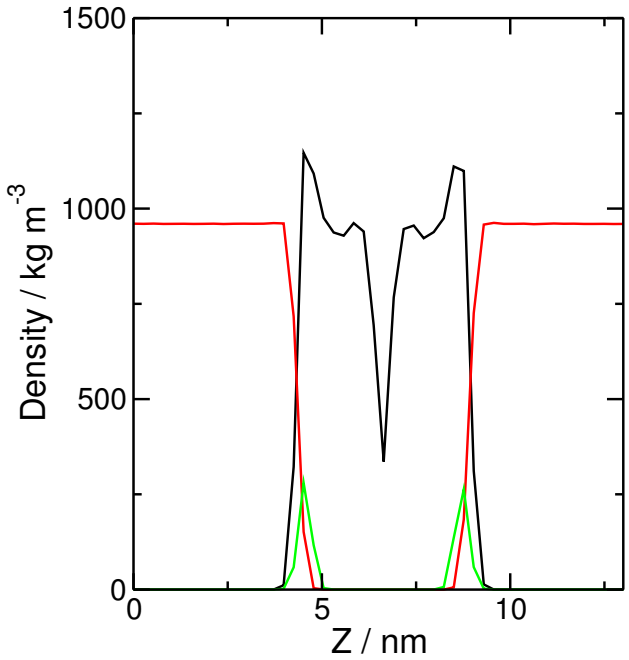

Figure 4.3: OA system density profile; OA in black, water in red and O19 atoms in green.

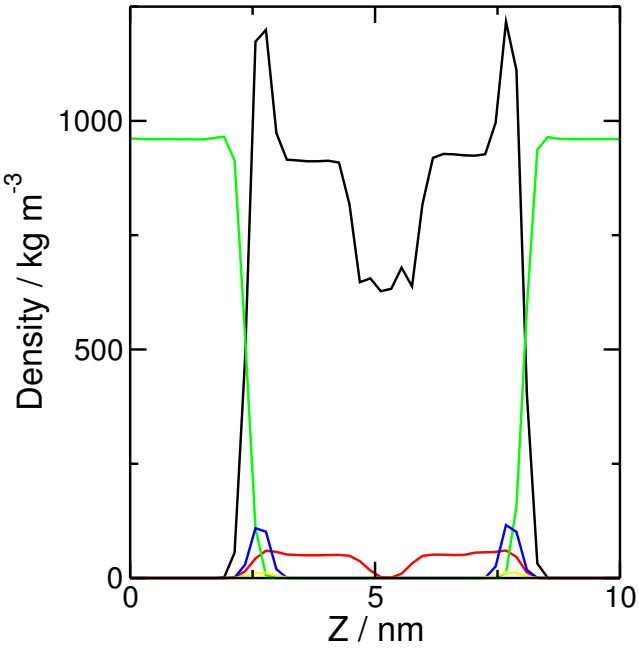

Figure 4.4: Mixed CER/OA system density profile; ceramide in black, OA in red, water in green, N23 atoms in blue and O19 atoms in yellow.

Order Parameters

CER NS has two hydrocarbon tails and by calculating the order parameters a measurement of the alignment of these chains with respect to the bilayer normal can be obtained. The order parameters of atoms in each chain are shown in Figure 4.5. The order parameter profiles for each chain of the CER are qualitatively similar, with a lower overall ordering of the C24 chain compared to the C16 chain. There is some

disorder for atoms in the chain closest to the interface and a high degree of order going down the chain into the most densely packed region of the bilayer. The order decreases again towards the center of the bilayer where a more fluid like region is found. The ceramides in the pure system are slightly more ordered than those in the mixed system although the order parameters are still indicative of a membrane in the gel phase, indicating there is no significant fluidisation in the presence of OA.

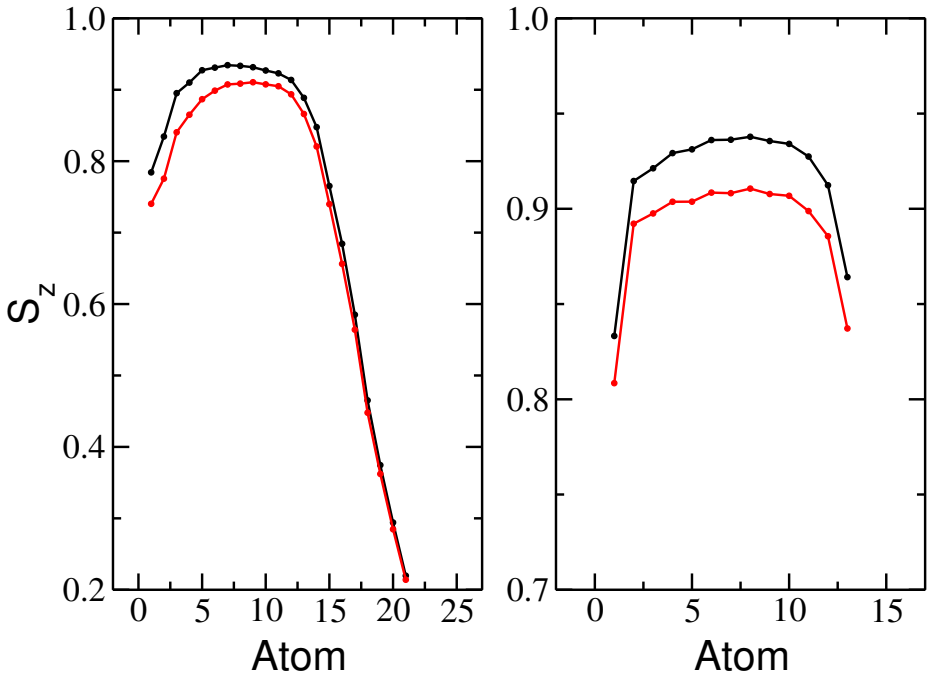

Figure 4.5: Order parameters for CER tail 1 (left) and tail 2 (right) as a function of the carbon atom of the CER tails; pure cCER system in black and mixed system in red.

Figure 4.6 shows that the OA chains in the pure system are less ordered than in the mixed which suggests that the ordered structure of the CERs influences the structure of the OA. This is contrary to the hypothesis that the 'kink' in OA causes the ceramide NS tails to disorder. While comparing both pure systems (Figure 4.7) we observe that the CER has a greater order than OA molecules throughout.

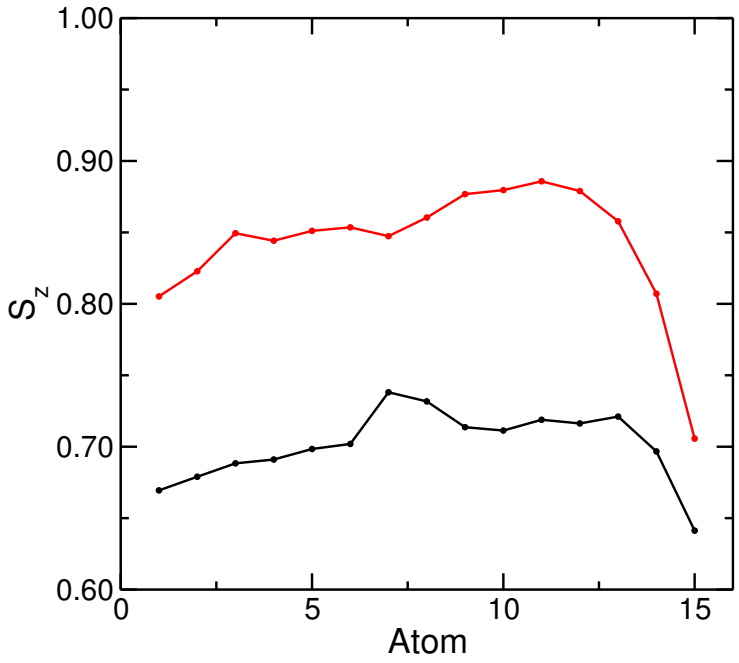

Figure 4.6: Order parameters for OA tail; pure OA system in black and mixed system in red.

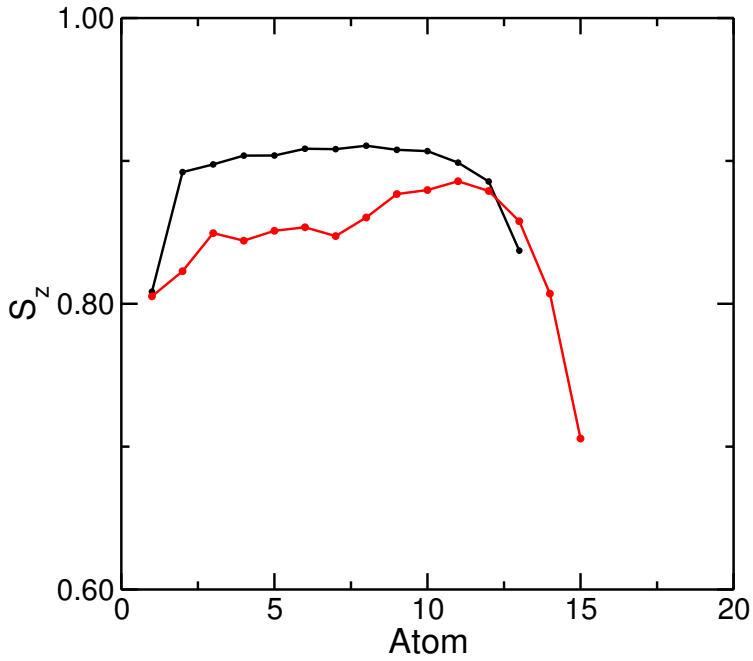

Figure 4.7: Order parameter comparison between C16 CER tail (black) and OA tail (red) in the mixed system.

By zooming in on the OA molecules in the mixed system (Figure 4.8), we see that some of the OA shows its distinct 'kinked' structure (B) which disrupts some of the local CER molecules from their well packed structure. But the majority of the OA aligns well with the CER chains (A), becoming more ordered than OA seen in the pure system.

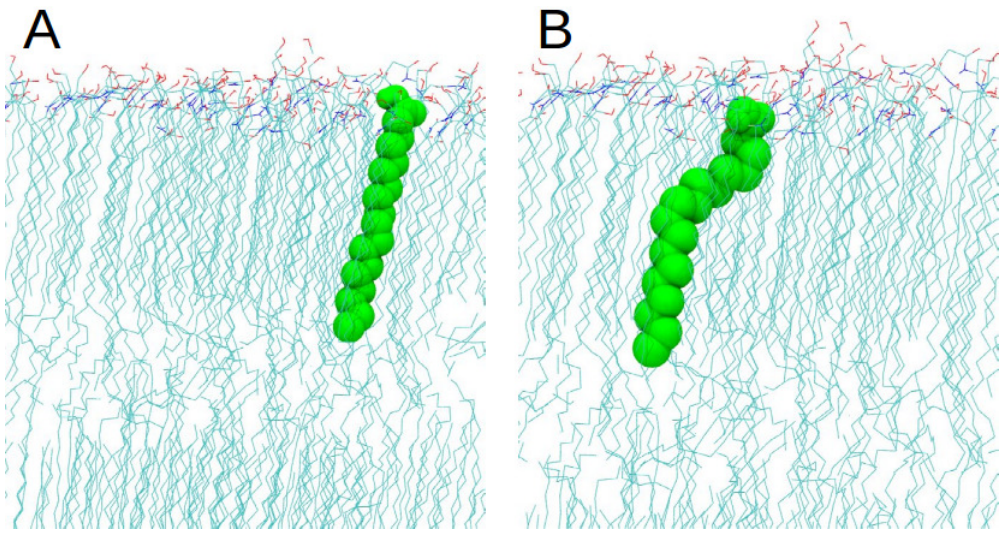

Figure 4.8: Snapshots showing that OA takes up two conformations; A) aligned B) kinked, in the mixed bilayer systems.

Hydrogen bonds

The SC is known to have a strong lateral hydrogen bonding network which gives it strong barrier properties. To understand how the penetration enhancer OA weakens this barrier the number of hydrogen bonds in each system were calculated and presented in Table 4.3. A CER forms 1.373 ± 0.038 hydrogen bonds per lipid with other lateral ceramides and 2.405 ± 0.064 with water in the pure system. Addition of OA reduces the lateral hydrogen bonds to 1.302 ± 0.080, and 0.119 ± 0.024 bonds are formed between CER and OA. The amount of hydrogen bonds between the CER and water is slightly increased to 2.455 ± 0.136, while pure OA forms less bonds with water at only 1.167 ± 0.276 per lipid. In the pure OA bilayer 0.267 ± 0.029 hydrogen bonds per lipid were formed between lateral lipids, which is considerably less than that calculated in the pure CER system. The overall number of lipid-lipid hydrogen bonds in the mixed system was less than in the pure CER suggesting that OA weakens the lateral network. This trend is also seen in the study by Akinshina *et al.* of *cis*-fatty acids[80] in CER bilayers.

Hydrogen bonding	
System (HB)	No. of HBs / Lipid
Mixed (Lipid-Lipid)	1.330 ± 0.052
Mixed (Lipid-Water)	2.241 ± 0.084
Mixed (Inter CER-CER)	1.302 ± 0.080
Mixed (Inter CER-OA)	0.119 ± 0.024
Mixed (CER-Water)	2.455 ± 0.136
Mixed (OA-Water)	1.167 ± 0.276
OA (Inter OA-OA)	0.267 ± 0.029
OA (OA-Water)	1.647 ± 0.070
CER (Inter CER-CER)	1.373 ± 0.038
CER (CER-Water)	2.405 ± 0.064

Table 4.3: Hydrogen bonding distribution for the pure CER, pure OA and mixed bilayers.

Lateral Diffusion Coefficients

The lateral diffusion coefficients of lipids for each of the pure systems and both the CER and OA in the mixed system are shown in Table 4.4. The CER system has a low diffusion rate of $4.496 \times 10^{-8} \pm 2.342 \times 10^{-8}$ cm^2 s^{-1} due to the slow mixing in the gel-phase at 305 K. The OA diffuses a magnitude faster which could be attributed to the lack of lateral hydrogen bonds compared to the pure CER system. The OA enhances the lateral diffusion of the CERs in the mixed bilayer. This effect of OA has been seen on other lipid systems in previous studies.

Lateral Diffusion Coefficients	
System	D / cm^2 s^{-1}
CER	$4.496 \times 10^{-8} \pm 2.342 \times 10^{-8}$
OA	$4.470 \times 10^{-7} \pm 3.590 \times 10^{-7}$
MIXED (CER)	$2.820 \times 10^{-7} \pm 7.710 \times 10^{-7}$
MIXED (OA)	$2.800 \times 10^{-7} \pm 7.790 \times 10^{-7}$

Table 4.4: Lateral diffusion coefficients for the pure CER, pure OA and mixed lipid system.

4.3.2 Water Permeation

To evaluate the permeation of a water molecule along the bilayer normal of the three different bilayer systems, the PMF for a water molecule moving from bulk water to the COM of the bilayer was calculated. The steered MD simulation used to pull the water molecule across the membrane does not cause significant disruption to its structure.

For the pure CER bilayer, when the water molecule is at $z = 0$ nm separation distance located within the midplane, it interacts with some of the nearby lipid tails. The water molecule has more freedom to explore at the midplane, see Figure 4.9c, compared to that of the densely packed hydrophobic tails at $z = 1.6$ nm in Figure 4.9b. At the interface the water molecule disrupts the headgroup hydrogen bonding between lateral CERs in Figure 4.9a. There is less interaction between the water molecule and the OA headgroup compared to the CER due to less hydrogen bonding, see Figure 4.10a. There is little space for the water to move within the hydrophobic core in Figure 4.10b and at the midplane in Figure 4.10c where the OA chains are not willing to be flexible. In Figure 4.11a the hydroxyl groups appear to orientate around the water molecule for favourable hydrophilic interactions. Further inside the bilayer, there is OA in the local environment, with the kinked hydrocarbon tail helping to create more space for the water molecule when surrounded by hydrophobic lipid chains (Figure 4.11b). At the midplane there is more free volume as the chains rotate to avoid the water molecule. The local OA creates more space between the CER lipid chain (Figure 4.11c).

To take into account the lateral heterogeneity of the CER/OA mixed bilayer, three independent PMF profiles were calculated, corresponding to different locations of the water molecule in the xy plane. Three independent profiles were also calculated for the pure OA bilayer and two for the pure CER bilayer. The independent PMF profiles for water in the pure CER, pure OA and mixed CER/OA bilayers are shown in Figures 4.12, 4.13 and 4.14 respectively. For the mixed system the local environment of the permeating water molecule was different with MIX1 referring to a ceramide-dominant surrounding and MIX2 and MIX3 referring to a pathway adjacent to an OA molecule. The average (AV) of the PMF for each system is also plotted.

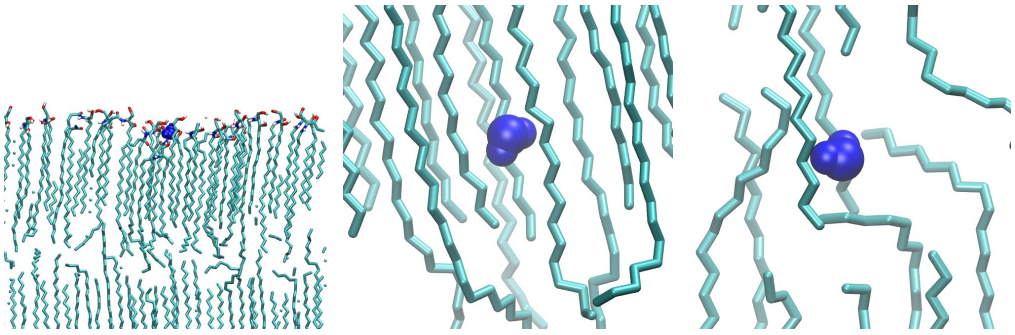

(a) CER1 at $z = 2.4$ nm (b) CER1 at $z = 1.2$ nm (c) CER1 at $z = 0.0$ nm

Figure 4.9: CER1 bilayer systems with the constrained water moelcule for PMF calculations in blue VDW fill at different z heights. Oxygen atoms shown in red, nitrogen in blue, hydrogen in grey and CER lipid tails in cyan.

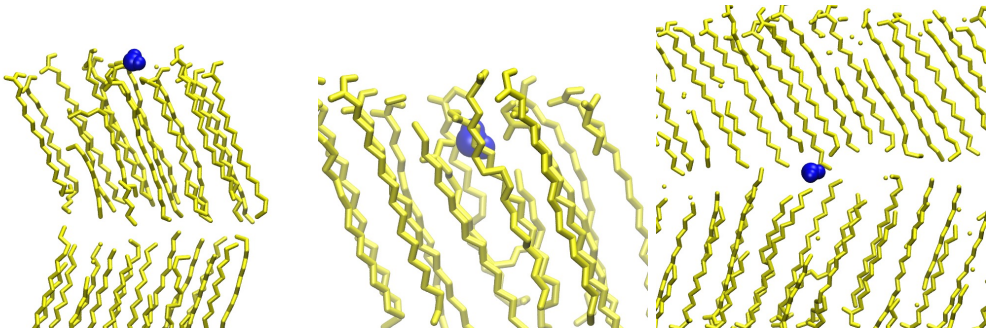

(a) OA1 at $z = 2.2$ nm (b) OA1 at $z = 1.6$ nm (c) OA1 at $z = 0.0$ nm

Figure 4.10: OA1 bilayer systems with the constrained water moelcule for PMF calculations in blue VDW fill at different z heights. Oxygen atoms shown in red, hydrogen in grey and OA in yellow.

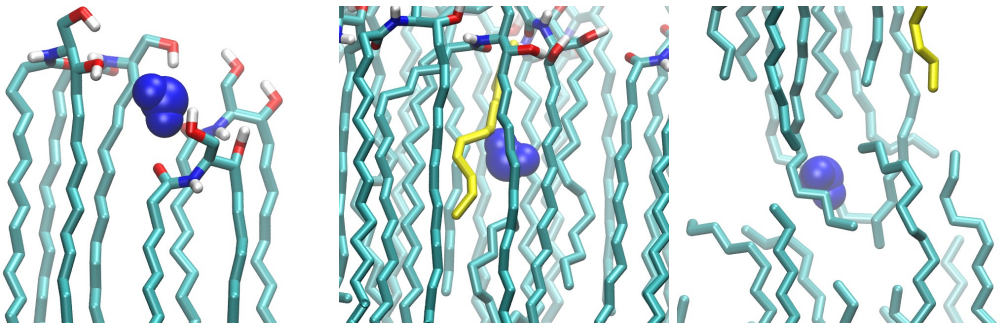

(a) MIX2 at $z = 2.4$ nm (b) MIX2 at $z = 1.8$ nm (c) MIX2 at $z = 0.0$ nm

Figure 4.11: MIX1 bilayer systems with the constrained water moelcule for PMF calculations in blue VDW fill at different z heights. Oxygen atoms shown in red, hydrogen in grey, nitrogen in blue, CER lipid tails in cyan and OA in yellow.

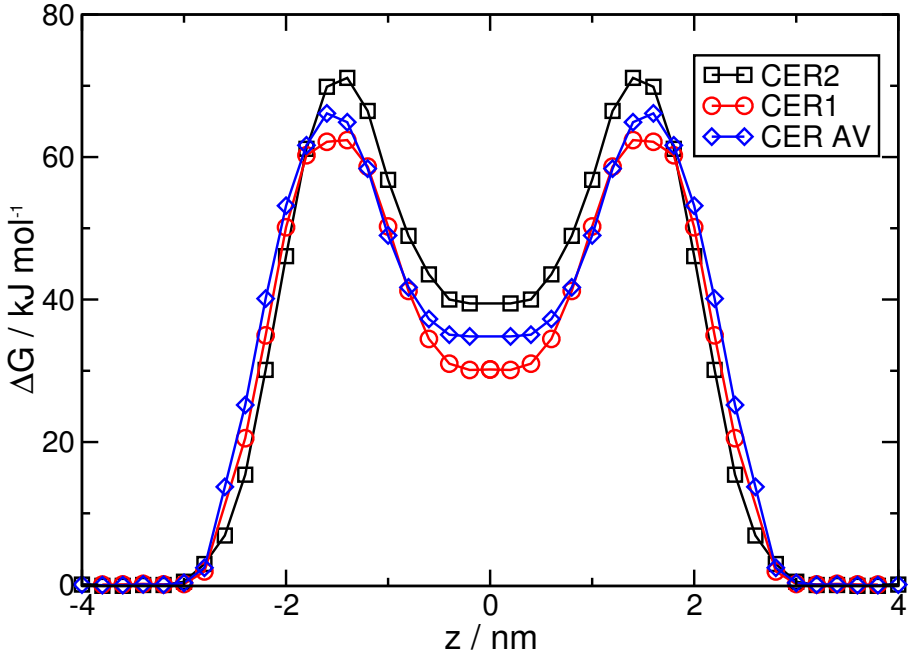

Figure 4.12: Ceramide Free energy profiles; CER1 in red circles, CER2 in black squares and the average of the two profiles labelled 'CER AV' in blue diamonds.

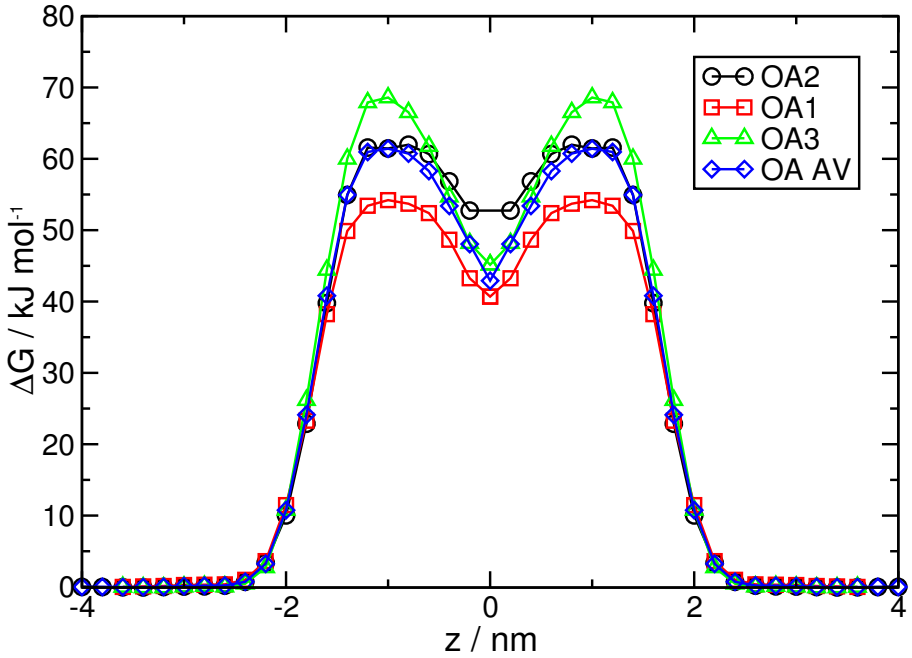

Figure 4.13: Oleic Acid Free energy profiles; OA1 in red squares, OA2 in black circles, OA3 in green triangles and the average of the three profiles labelled 'OA AV' in blue diamonds.

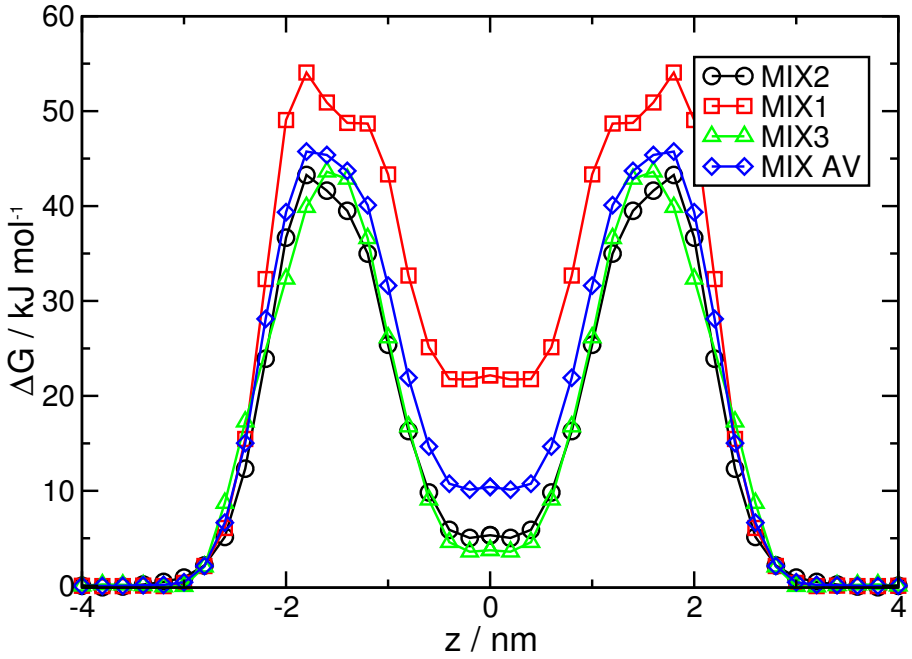

Figure 4.14: Mixed Ceramide/OA Free energy profiles; MIX1 in red squares, MIX2 in black circles, MIX3 in green triangles and the average of the three profiles labelled MIX AV in blue diamonds.

The average PMF for each of the systems shown in Figure 4.15. In each of the systems, as the water molecule migrates through the bulk water, the PMF is plateaued at its lowest value. The PMF starts to increase at the corresponding interface region, around 2.8 nm from the COM for the pure ceramide system until a peak of ∼66 kJ mol^{-1} is

reached at 1.6 nm from the COM of the bilayer. At the COM there is a local minimum of ∼35 kJ mol^{-1}. For the OA system the PMF starts to increase at 2.4 nm from the COM with a barrier height of ∼61 kJ mol^{-1} at 1 nm and a local minimum of ∼43 kJ mol^{-1} at the COM. Due to the differences of the local environment of the permeating water molecule the PMF of the mixed systems had a greater variance (Figure 4.14). In the CER dominated environment the PMF starts to increase at 2.8 nm from the COM with a barrier height of ∼54 kJ mol^{-1} at 1.8 nm and a local minimum of ∼22 kJ mol^{-1} at the COM. This is similar to the profile for a pure CER bilayer except that the centre of the bilayer seems to present a more favourable environment for water in the mixed system than in the pure CER system. The barrier height in this mixed bilayer is 10 kJ mol^{-1} lower. When OA is present in the local environment of the permeating water, the PMF starts to increase at 2.8 nm from the COM with a significantly lower barrier height of ∼43 kJ mol^{-1} at 1.6 nm and a local minimum of only ∼4 kJ mol^{-1} at the COM. This low minimum could be attributed to fewer C24 CER tails in the system and poorer packing at the midplane, this could allow water to become trapped at the COM.

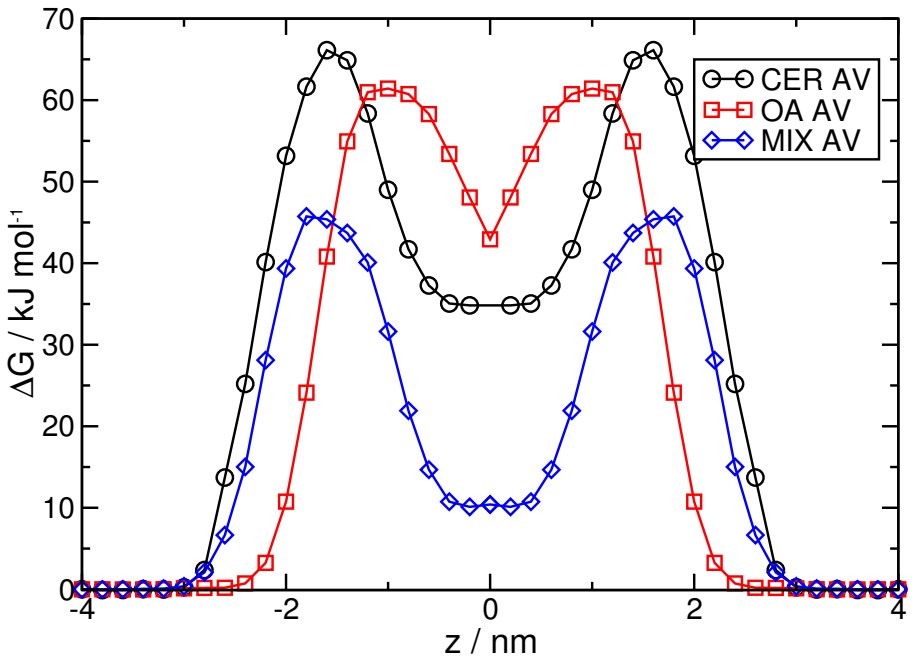

Figure 4.15: Comparison of Free energy profiles; CER AV in black circles, OA AV in red squares and MIX AV in blue diamonds.

4.3.3 Convergence of Free Energy Calculations

To make sure the free energy calculations were accurate the PMF was plotted every 2 ns, from 2 ns until the PMF converged. Systems took either 12 or 14 ns to converge. The convergence plots for the pure CER bilayers (Figures 4.16 and 4.17), the pure OA bilayers (Figures 4.18, 4.19 and 4.20) and the mixed bilayers (Figures 4.21, 4.22 and 4.23) are included below.

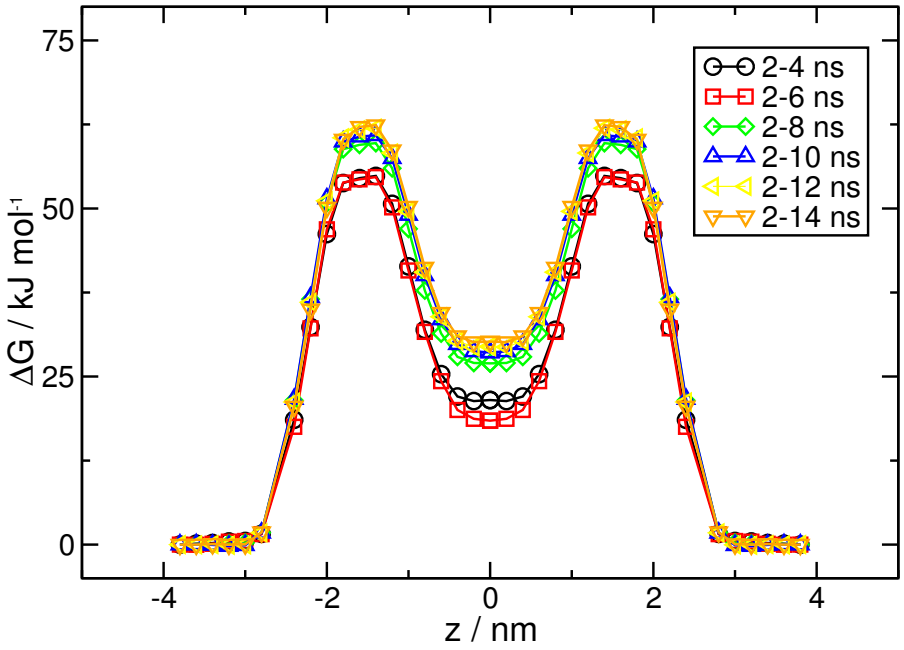

Figure 4.16: Convergence of free energy profile of CER1 over time. Black circle shows 2-4 ns, red square 2-6 ns, green diamond 2-8 ns, blue triangle up 2-10 ns, yellow triangle left 2-12 and orange triangle down 2-14 ns.

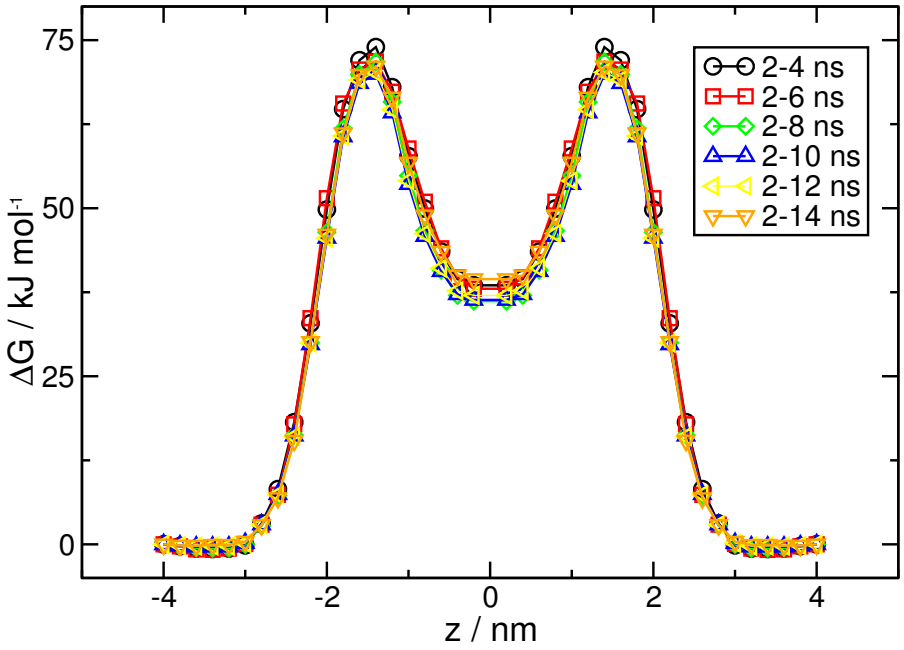

Figure 4.17: Convergence of free energy profile of CER2 over time. Black circle shows 2-4 ns, red square 2-6 ns, green diamond 2-8 ns, blue triangle up 2-10 ns, yellow triangle left 2-12 and orange triangle down 2-14 ns.

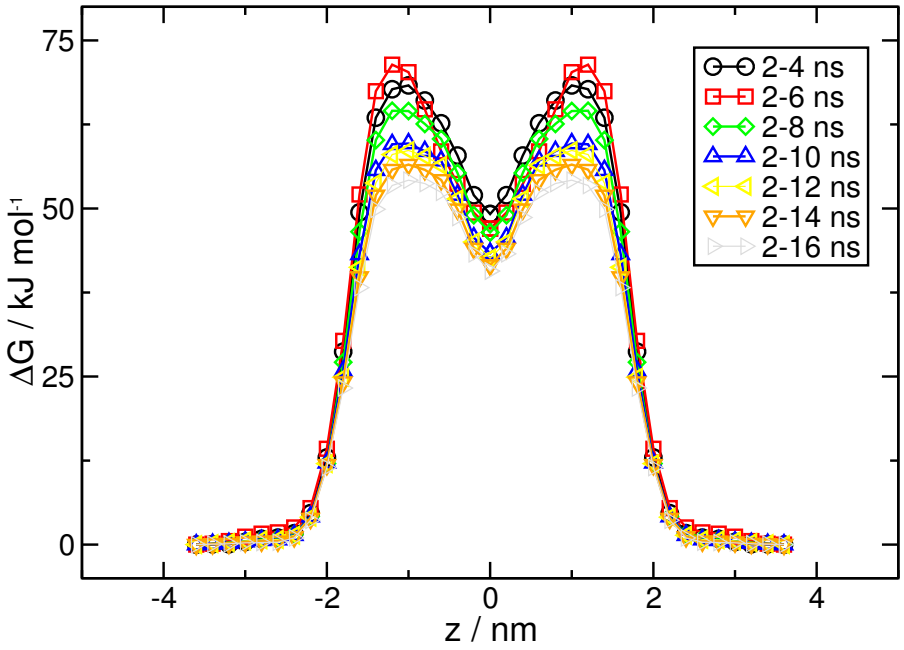

Figure 4.18: Convergence of free energy profile of OA1 over time. Black circle shows 2-4 ns, red square 2-6 ns, green diamond 2-8 ns, blue triangle up 2-10 ns, yellow triangle left 2-12 and orange triangle down 2-14 ns.

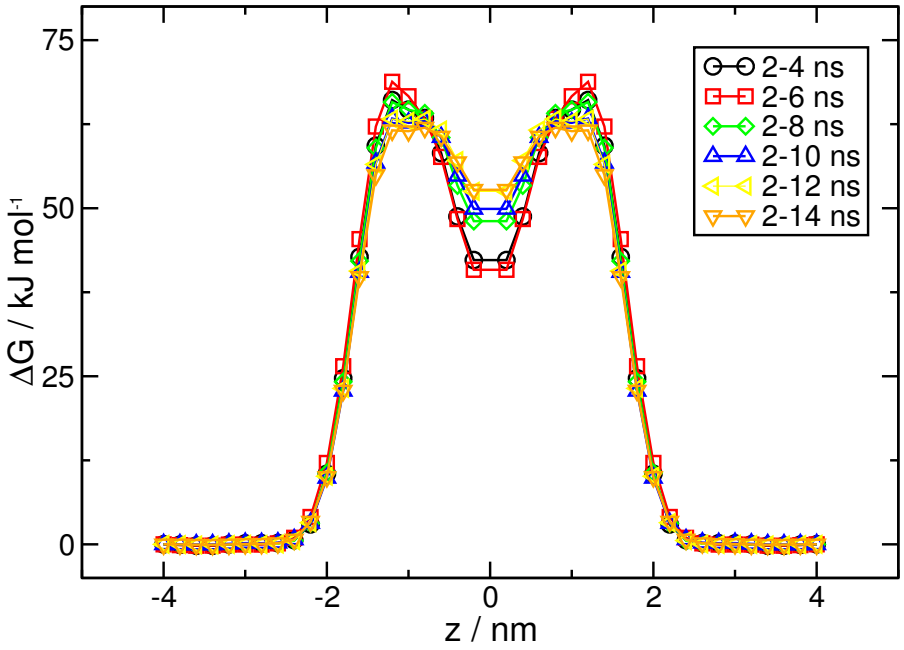

Figure 4.19: Convergence of free energy profile of OA2 over time. Black circle shows 2-4 ns, red square 2-6 ns, green diamond 2-8 ns, blue triangle up 2-10 ns, yellow triangle left 2-12 and orange triangle down 2-14 ns.

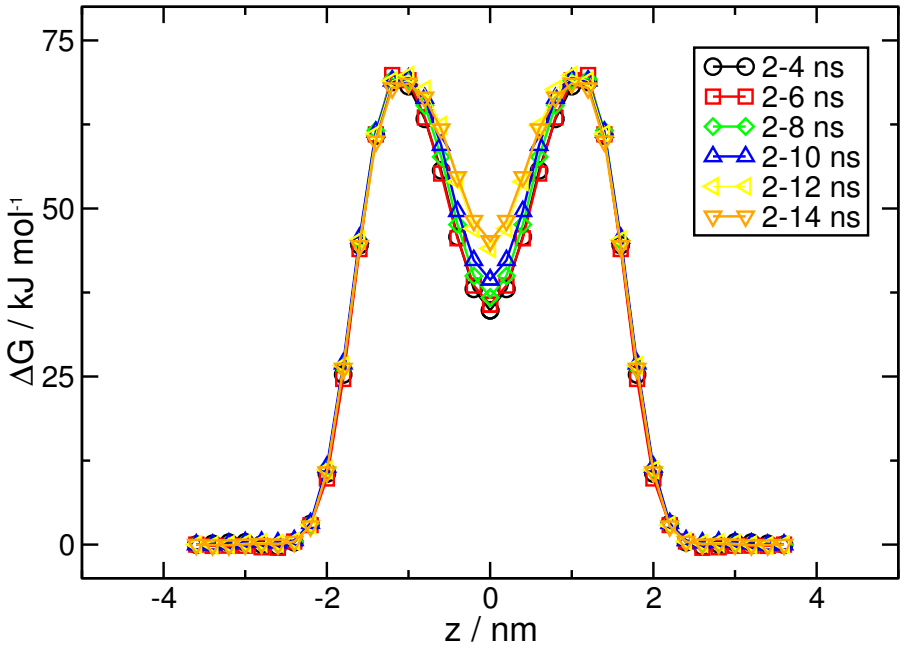

Figure 4.20: Convergence of free energy profile of OA3 over time. Black circle shows 2-4 ns, red square 2-6 ns, green diamond 2-8 ns, blue triangle up 2-10 ns, yellow triangle left 2-12 and orange triangle down 2-14 ns.

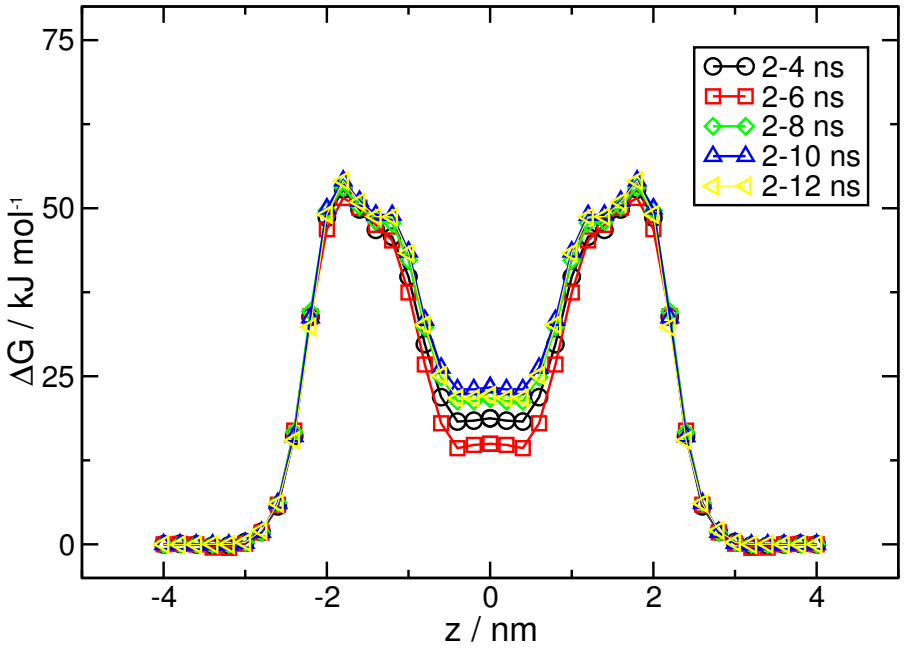

Figure 4.21: Convergence of free energy profile of MIX1 over time. Black circle shows 2-4 ns, red square 2-6 ns, green diamond 2-8 ns, blue triangle up 2-10 ns, yellow triangle left 2-12 and orange triangle down 2-14 ns.

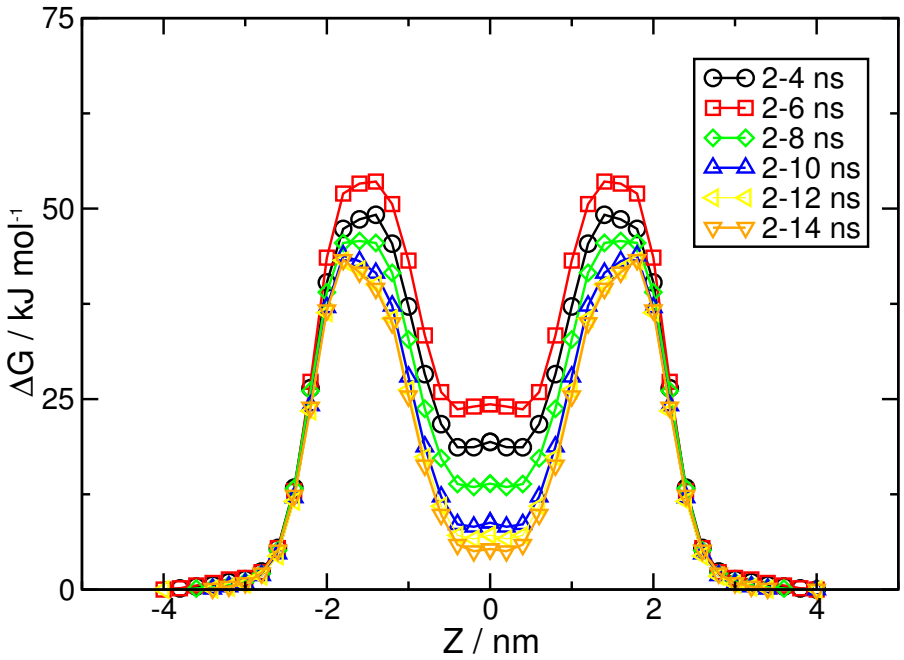

Figure 4.22: Convergence of free energy profile of MIX2 over time. Black circle shows 2-4 ns, red square 2-6 ns, green diamond 2-8 ns, blue triangle up 2-10 ns, yellow triangle left 2-12 and orange triangle down 2-14 ns.

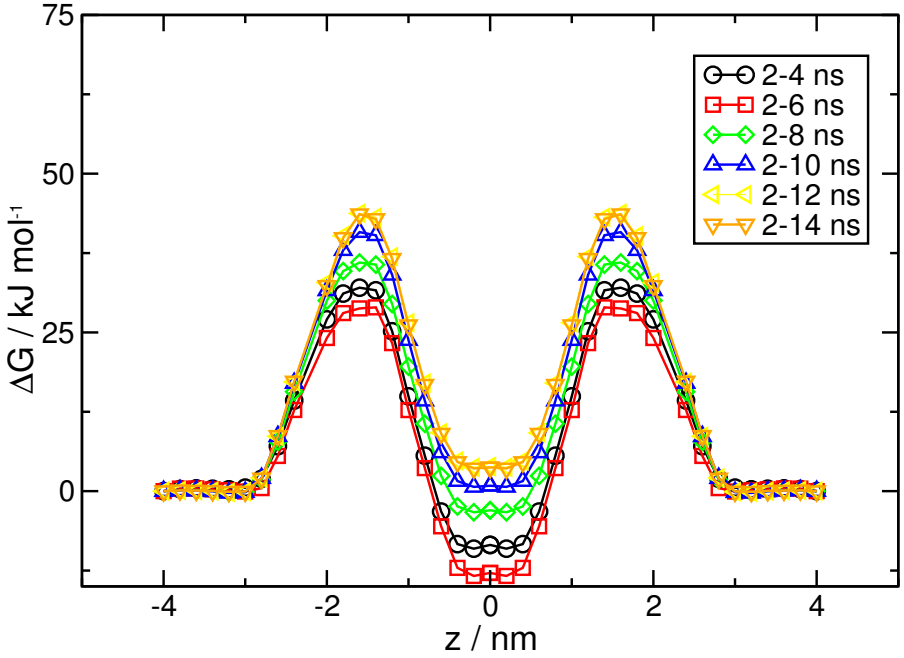

Figure 4.23: Convergence of free energy profile of MIX3 over time. Black circle shows 2-4 ns, red square 2-6 ns, green diamond 2-8 ns, blue triangle up 2-10 ns, yellow triangle left 2-12 and orange triangle down 2-14 ns.

4.3.4 Diffusion Coefficients

The diffusion of permeants through the bilayer normal, $D(z)$, can be calculated using the friction coefficient $I(\acute{t})$ at each time and height by integrating the autocorrelation function (ACF) from 0 to infinity as in Section 2.6.2. It is not feasible to integrate over

infinite time, so a sufficient time period must be used instead, therefore the diffusion coefficients calculated using this method may be sensitive to the simulation length and the total time over which the ACF is integrated. In these simulations, F_z is collected every 1 fs for a total of 500 ps and the ACF is integrated over 25 ps, which is sufficient for the ACF to reduce to zero.

The diffusion coefficients as a function of position in the bilayer are shown in Figures 4.24, 4.25 and 4.26. The diffusion coefficients generally follow the inverse trend to the PMF profile with low diffusion of water in regions where the free energy is high, except at 1.8 nm from the COM where we are approaching the maximum barrier height, the diffusion increases surprisingly, before decreasing as we go through the barrier (and the bilayer) with a increase at the COM.

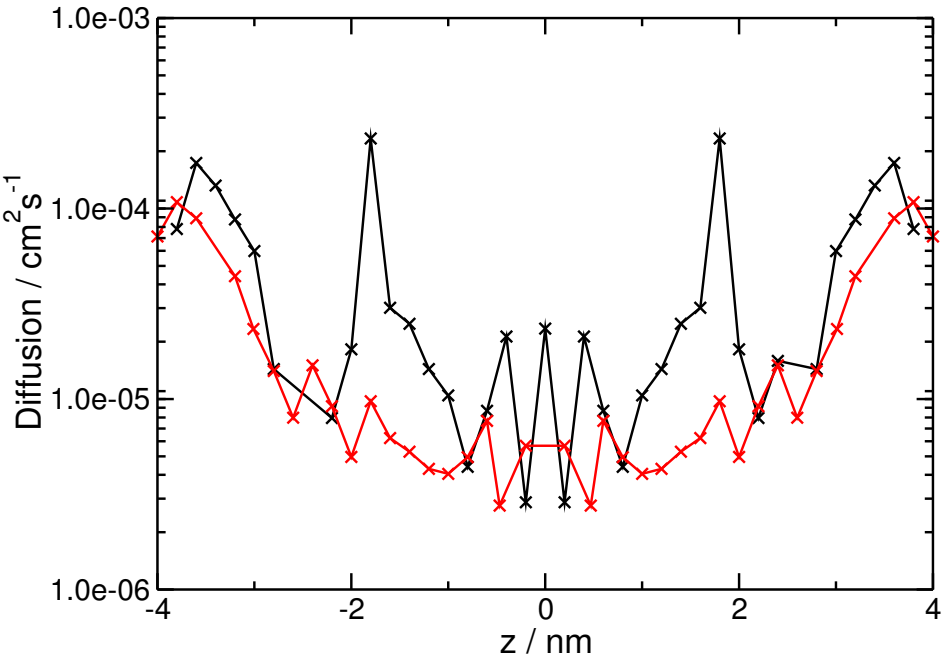

Figure 4.24: Diffusion coefficients as a function of bilayer height for CER1 (black) and CER2 (red).

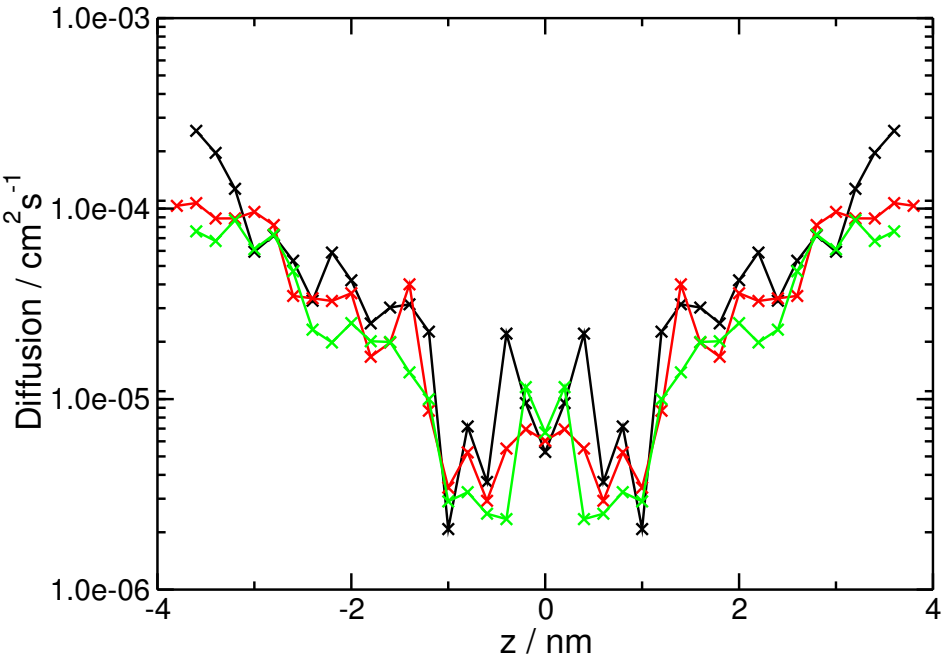

Figure 4.25: Diffusion coefficients as a function of bilayer height for the OA1 run (black), OA2 run (red) and OA3 run (green).

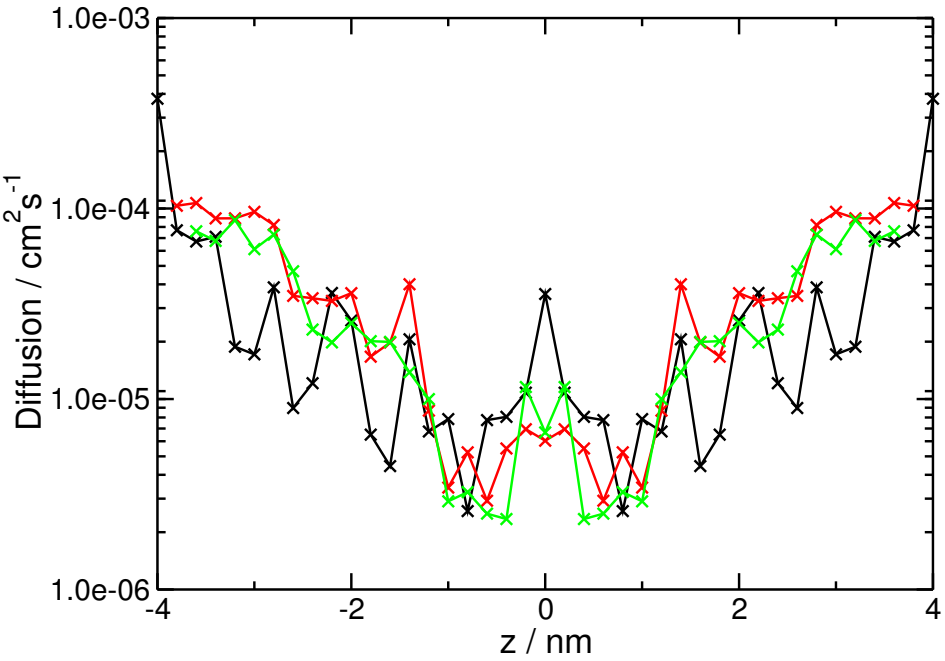

Figure 4.26: Diffusion coefficients as a function of bilayer height for the MIX1 run (black), MIX2 run (red) and MIX3 run (green).

4.3.5 Permeability

The permeability coefficient can be calculated from the values of the diffusion coefficient and the PMF as described in Section 2.6.2. In Table 4.5, permeation coefficients have been calculated for each system and their independent repeats. The mixed systems have the highest permeability, the one with an adjacent OA even more so. The

CER systems have on average the lowest permeability. It is important to note that the permeability coefficients are very sensitive to the barrier height of the PMF to due its exponential dependence. For clarity, the ACF integration time of 25 ps has been used in the calculation of the permeability, the ACF decays from 1 to 0 rapidly in this time frame and is a compromise time as it is not practical to extract the force for this large number of data points.

System	P / cm^2 s^{-1}
CER1	6.434 x 10^{-16}
CER2	5.071 x 10^{-18}
OA1	8.173 x 10^{-17}
OA2	1.787 x 10^{-15}
OA3	7.614 x 10^{-18}
MIX1	5.505 x 10^{-15}
MIX2	2.922 x 10^{-13}
MIX3	1.135 x 10^{-13}

Table 4.5: Permeability coefficients for pure CER, pure OA and mixed CER/OA systems.

4.4 Discussion

From the calculations of the permeability coefficients it can be concluded that the mixed system containing both CER and OA is the most permeable for the small permeant water, due to the larger permeability coefficients. The values of P for MIX2 (2.922×10^{-13}) and MIX3 (1.135×10^{-13}) are two orders magnitude larger than that of MIX1 (5.505×10^{-15}), showing that the local environment can have a significant impact on macroscopic properties of the bilayer such a permeability.

It can be seen that the permeability has direct correlation with the free energy profiles. The mixed system had the smallest energy barrier of ~ 54 kJ mol^{-1} for mainly ceramide local environment and ~ 43 kJ mol^{-1} with OA in the local environment. This barrier was ~ 12 kJ mol^{-1} lower than the pure ceramide system showing that the presence of OA lowers the free energy barrier of the system. This is due to the disruption of the strong lateral hydrogen bonding network between the ceramide headgroups caused by the embedded OA. The lack of lateral hydrogen bonding of the OA, combined with its kinked structure leads to greater disorder in the chains near the interface compared to the pure ceramide system, allowing for easier penetration of permeants into the bilayer.

The other significant factor is the diffusion coefficients at each height of the bilayers. When comparing the diffusion coefficients of the local environments for the mixed system (Figure 4.26, it can be seen that the diffusion is similar at the interface where there is bulk water. The diffusion is faster below the headgroup and down the chains with the OA environment due to the added disorder caused by the OA tails. The diffusion is slightly slower at the interface for the pure ceramide but the diffusion is slightly slower at the tail region and the COM when OA is in the local environment. From the analysis of our data we can say that addition of OA lowers the free energy barrier, decreases the diffusion in the tail region but overall increases the permeability of the bilayer.

The pure OA system also shows greater permeability than the pure ceramide system. The pure ceramide system has the largest energy barrier at ~ 66 kJ mol^{-1} compared to ~ 61 kJ mol^{-1} for the pure OA. This again is due to the strong lateral hydrogen bonding network, preventing the disruption of the bilayer by permeants. The diffusion is a lot faster at the interface and top half of the tails in the pure OA system compared to that of the ceramide as there is less order within the headgroups. Towards the COM the diffusion is of similar magnitude, while at the COM the diffusion of water is higher for the ceramide as the fluid tail region has significantly greater order. Despite the pure OA system having lower order parameters than the mixed systems around the interface and a lack of hydrogen bonding, the smaller headgroup of the OA in the gel-phase leading to a much smaller APL provides stronger resistance to permeation than the disruption to the packing in the mixed systems. Therefore in a phase separated system this pathway through an OA pool would still be a preferred route.

The mixed system has a higher permeability than the pure OA system due to the the lower free energy barrier caused by the disruption of the OA to the lateral hydrogen bonding network of the ceramides and a lowering of the order of the headgroup and tails due to the kinked tail structure. These effects have greater significance than the more disordered OA, with a lack of hydrogen bonding, as the small headgroup and single tail can pack well in the gel phase causing a smaller APL to prevent the penetration of permeants.

The permeability of the pure CER bilayer is rather small at $\sim 10^{-16}$ for CER1 and $\sim 10^{-18}$ for CER2 in comparison with other permeability studies of skin lipid bilayers. For example, Das et al.[45] calculated a value of 1.1×10^{-8} for the same system at 350 K which is many orders of magnitude larger. This difference in permeability can be attributed to the larger free energy barrier calculated, as the values for diffusion were of similar size, $\sim 10^{-4}$ - 10^{-6}, with the system at 350 K having a faster rate of diffusion. At 350 K a barrier height of 42.7 kJ mol^{-1} was calculated which is $\sim$ 25 kJ mol^{-1} smaller than that of the pure CER at 68 kJ mol^{-1}, this suggests that a temperature difference of 50 K could be significant enough to weaken the free energy barrier. This effect of the temperature on the permeability can also be seen when comparing the 2:2:1 bilayer at 300 and 350 K by Das. A difference of 5.3 kJ mol^{-1} in the barrier height is observed leading to two orders of magnitude difference in their permeability coefficients. The same trend can be observed when comparing the 1:1:1 fully hydrated simulations of Del Regno[204] at 305 K with Das[8] at 350 K. A difference of $\sim$ 5 kJ mol^{-1} in the barrier height leads again to a two magnitude order difference in the permeability coefficients (10^{-10} versus 10^{-8}). Arrenhius plots calculated from experiment over a temperature range from 278 to 323 K in Human SC gives an activation energy of $\sim$ 59.4 kJ mol^{-1} while for temperatures over 343 K for delipidized Human SC has a much lower energy of $\sim$ 26.4 kJ mol^{-1}. The same trend is seen for Porcine SC with the larger activation energy needed for lower temperatures and corresponds with the permeability coefficients.

The potential of mean force constraint method is more accurate at calculating permeability coefficients of DPPC bilayers, simulations by Bemporad and Marrink give a barrier height of 23-26 kJ mol^{-1} and Marrink calculates $P = 7 \pm 3 \times 10^{-2}$ which is in good agreement with experimental values and compares favourably with the activation energy of water in Hexadecane ($\sim$ 25 kJ mol^{-1})? .

As there is an exponential dependence of ΔG, the permeation depends strongly of the lipid composition of the bilayer. This has been investigated in the aforementioned simulation studies with the use of 1:1:1 and 2:2:1 ratios of skin lipids. The 2:2:1 bilayer in the study by Das *et al.* showed a permeability of increase of a magnitude at the same temperature. Del Regno also shows a higher permeability and attributes it to the presence of CHOL which increases the disorder in the bilayer and increases the free

volume. The addition of OA to the pure CER bilayer plays a similar role in creating a greater free volume and disorder within the membrane, reducing the permeability by a few orders of magnitude. The permeability values are still rather small compared to other mixed systems as only a 9:1 ratio was calculated to match with current formulations. It is suspected that an equal ratio of CER to OA would lead to coefficients of similar magnitude to calculated tertiary systems. A collection of free energy barriers, minima and permeability coefficients for previous simulations and experiments can be found in Table 4.6, where available.

Permeability Comparisons					
	T (K)	System[a]	ΔG_{max} (kJ/mol)	ΔG_{COM} (kJ/mol)	P (cm^2/s)
Simulations					
O'Neill	305	CER1	62.4	30.1	6.4 x 10^{-16}
	305	CER2	71.1	39.5	5.1 x 10^{-18}
	305	OA1	54.2	40.7	8.1 x 10^{-17}
	305	OA2	62.0	52.7	1.8 x 10^{-15}
	305	OA3	68.6	45.2	7.6 x 10^{-18}
	305	MIX1	54.1	22.2	5.5 x 10^{-15}
	305	MIX2	43.3	5.3	2.9 x 10^{-13}
	305	MIX3	43.6	3.7	1.1 x 10^{-13}
Das[214]	340	1.75:1.75:1			
		Double bilayer ≈18wpl	≈ 37	10.3 ± 3.6	-
Das[45]	350	1:0:0	42.7	≈ 29	1.1 × 10^{-8}
	350	1:1:1	34.6	-	8.2 × 10^{-8}
	350	2:2:1	33.8	-	1.3 × 10^{-7}
	300	2:2:1	38.5	-	3.7 × 10^{-9}
Del Regno[204]	305	1:1:1 FH	≈ 30	≈ 10	3.3 × 10^{-10}
	305	1:1:1 LH	≈ 27	≈ 5	5.3 × 10^{-9}
Bemporad[43]	-	DPPC	22.9 ± 1.9	1.8	-
Marrink[41]	350	DPPC	26 ± 2	24.5	7 ± 3 × 10^{-2}
Experiments					
Blank[227]		Human	-	-	≈ × 10^{-7}
Potts[228]		Porcine	-	-	≈ 1.1 ± 0.1 × 10^{-7}
Schatzberg[229]	-	Water in Hexadecane	24.9	-	-
Arrenhius					
Scheuplein[230]	278-323	Human SC	≈ 59.4	-	-
Scheuplein[230]	≥343	delipidized Human SC	≈ 26.4	-	-
Golden[226]	≤343	Porcine	≈ 72.0	-	-
Golden[226]	≥343	Porcine	≈ 23.8	-	-
Golden[226]	343	Porcine	-	-	5.86 ± 1.22 × 10^{-6}
Golden[226]	333	Porcine	-	-	2.23 ± 0.489 × 10^{-6}
Golden[226]	323	Porcine	-	-	1.01 ± 0.389 × 10^{-6}
Golden[226]	313	Porcine	-	-	5.11 ± 2.17 × 10^{-7}
Golden[226]	303	Porcine	-	-	3.14 ± 1.33 × 10^{-7}
Allenby[231]	303-338	Intact Human SC	≈ 64.4	-	-

Table 4.6: Comparison of Potential of mean force calculations of skin lipids in the literature. [a]Ratio of CER[NS]24:CHOL:FFA24 unless otherwise stated.

The permeability coefficients calculated here are significantly lower than the permeability calculated experimentally for human SC ($\sim 10^{-7}$ cm^2 s^{-1}), due to it containing unsaturated lipid tails and a highly polydisperse nature. Theses features are likely to reduce the permeability compared to the models presented here. Experimental patches are also likely to be defect free and so will give the lowest value for a range of permeabilities.

The self-diffusion coefficient of water in the bulk has been measured in the order of $\approx 10^{-4}$ cm^2 s^{-1} for the three different systems analysed in this study. This is in good agreement with other PMF simulations of skin lipids including fully hydrated 1:1:1 ratio of CER:CHOL:FFA bilayers by del Regno at 305 K[204] and of a pure CER bilayer at 350 K by Das *et al.* that calculated the diffusion at this magnitude[45]. Studies that compare the self-diffusion of various pure water models give values of 4.2(0.08) $\times 10^{-4}$ cm^2 s^{-1} for the SPC water model at temperatures around $\approx$ 300 K[232] and $\approx$ 4-5 $\times 10^{-4}$ cm^2 s^{-1} by van der Spoel[233]. These calculated values are in quantitative agreement with experiments using the diaphragm-cell technique that give a diffusion of 2.3 $\times 10^{-4}$ cm^2 s^{-1} at 298 K[234].

A limitation of this study is the idealised environment of the skin depicted in this model. Single and binary lipid compositions allow for computationally cheaper calculations and capture the general properties of the skin membranes. Alas, these models are lacking smaller molecules of NMF, oils and ions that are found on skin. Previous work by MacDermaid *et al.*[205] investigated a number of hydration levels with different pH conditions by initialising model systems with protonated and unprotonated FFAs at differing ratios. They observe that adhesion between lamellae becomes pH-dependent when reaching the relative humidity of the SC. Only one of the simulations at a higher pH level was able to maintain a stable multilamellar phase. In comparison, lower pH conditions cause the FFAs to change into an inverse micellar phase to produce disordered water droplets. Experiments from Hachem *et al.* show that a higher pH can negatively affect the barrier function of the SC by increasing the permeability of water and activating protease enzymes that destroy the bonds between corneocytes[235]. Observations by Leontiadou *et al.* show that sodium ions bind to the lipid-water interface and diffuse through the interface, this leads to an increase in line tension, followed by a destabilisation of the pore in DPPC membranes. Chlorine on the other hand prefers to situate in a bulk water environment or within the pore. Sodium ions can permeate through small pores but chlorine requires larger radii. An increase in salt ions has a destabilising effect on these pores and suggest that permeation rates are reduced with increasing ionic strength[236]. Therefore in future studies, it might be important to consider ions for higher complexity models.

4.5 Conclusion

In this study the permeation coefficients for three systems, pure CER, pure OA and a mixed CER/OA, have been calculated using the PMF and diffusion coefficients. The mixed system has the greatest permeability, followed by the pure OA, with the pure CER having the lowest. With the addition of OA into ceramide bilayers the most favourable pathway is through a heterogeneous environment, with local OA. The OA disrupts both the hydrogen bonding network and packing of the lipids which can allow greater space for permeants to penetration and create a pore in the bilayer, showing how OA is an effective penetration enhancer. In a phase separated system, an OA pool would still be a favoured route through the bilayer as the free energy barrier is still lower than the pure CER bilayer.

Chapter 5

Investigation of Finite System Size Effects on Coarse-grained Molecular Dynamics Simulations of Ceramide Bilayers

5.1 Introduction

The development of molecular modelling has greatly accelerated over the last 15 years, where upon larger biological systems can now be studied in depth, no more so than lipid bilayers. When modelling these systems we try to get an insight into their behaviour at the molecular level. With the use of specifically designed forcefields, we can get good agreement of structural and dynamical properties with known experimental data. Although the ability of forcefields will no doubt, always be in question, other factors when we model biological systems are also coming under more scrutiny. As the processing power of computers continues to improve year on year, the MD simulations that we can attempt, in terms of size and time, become ever more accessible. With this ability to simulate even larger systems, we can now directly look at the dependence of system size and deduce whether finite size effects in these systems have a significant impact on the bilayer properties, and thus warrants greater appreciation when building and testing our models.

Numerous studies have already been completed looking at dependence of system size on equilibrium properties in lipid bilayers. Most notably, was the debate on whether equilibrium area per lipid of small systems are underestimated due to suppressed undulations, undulations that are more readily seen in larger bilayer systems. To compensate for these lack of undulations it was suggested that a finite surface tension would be required[237]. This was disputed in another study, that did not find a dependence of surface tension on surface area[238]. To add further to this controversy, Lindahl and Edholm showed increased undulations would actually compress the lipid area[239]. The

work of a number of groups points to size dependent surface tension but is contradicted by studies by Marrink and later on Castro-Roman, that the effects of system size on surface tension are negligible in the stress-free regime[240,241]. Needless to say, finite size effects could be sensitive to the system makeup, as a general consensus in the literature has not quite been established.

Other structural and dynamical properties have been reported including electron density and deuterium order parameters[242] While many groups have shown strong system size dependence on diffusion coefficients for lipids in bilayers[243–247]. Although different forcefields and cut-off methods were used, making it hard to accurately compare such studies. The treatment of long range electrostatics relating to system size was noted by Klauda *et al.* and their work focused on dynamical quantities in PME simulations of varying sizes of DPPC bilayers.[248]

Finite system and periodicity effects have also been investigated on other biomolecules such as proteins[249–251] and solvation of ion interactions[252,253]. Bastuğ *et al.* performed free energy calculations of potassium ion from bulk to the membrane protein gramicidin A and showed that different system sizes has no noticeable effect[254]. Lee *et al.* on the contrary observed finite size artifacts when simulating asymmetric NaCl and KCl solutions separated by DPPC bilayers[255]. They warn that small water chambers could disrupt the ion distributions and water polarization data. While the finite number of lipids in their system prevented asymmetric change in area between the different chamber leaflets, resulting in an area decrease. For the first time we will consider the effect that the simulation set-up for bilayers surrounded by mixed solvents has on the simulation results. It is common for many authors to use high levels of hydration to solvate their lipid bilayer[45,163], or alternatively, switching to larger, even multilamellar systems[214]. In these studies the size of the bilayer and the total number of solvent molecules is usually fixed and seemingly arbitrarily chosen in advance. A major problem with this is that adsorption occurs at the interface and once the interface is saturated (at a certain concentration) the effect on the system is not known. It has not been tested yet if the size of the solvent layer (number of solvent molecules) or the size of the interface (the number of lipid molecules) has a significant impact on the results. Therefore, in this study we look at a number of CG ceramide bilayer systems, systematically changing the size of the bilayer. We also take a look at solvent effects on these systems, by altering the amount of a water/DMSO composition known to be a penetration enhancer, and compare with the previous atomistic study of DMSO penetration of ceramide bilayers[156]. The chemical structures of ceramide 2 and DMSO are shown in Section 1.3, Figures 1.3 and 1.12 respectively. We hope to determine any possible artifacts in our systems and advise future researchers on appropriate bilayer sizes and solvent concentrations. We have moved to a CG representation to improve the computational efficiency at the cost of chemical detail, which is not so important as we are testing the method here.

5.2 Computational Methodology

5.2.1 Initial Configurations

A single ceramide molecule was replicated in the x and y dimensions, producing a monolayer 8×4 long. This was replicated in the z direction to create a bilayer containing 128 lipids. This was used as a basic block in building the larger bilayer systems denoted "L". For the 2L systems, the L block was replicated in the x direction(2×1). For the 4L systems, the block was replicated in both the x and y (2×2). For the 8L systems, the block was replicated four times in the x direction and two times in the y (4×2). These four different bilayers are used to determine any size effects that may arise from our simulations. Each of these systems also contains four different solvent to lipid ratios, where the possible solvent effects can now be monitored. The solvent consisted of a composition of water and DMSO(0.625%). This percentage of DMSO was determined as the minimum concentration of DMSO that doesn't lead to penetration of the bilayer. In this way, we can use this system as a basis of comparison for other systems with variance in solvent or size. The contents of each of the 16 systems we have studied can be found in Table 5.2.

To equilibrate the systems an energy minimisation was first performed, followed by a 2 ns NPT run with position restraints of 1000 kJ mol−1 on the ceramides in all directions, enabling the solvent to equilibrate. Due to slow convergence of the volume of the solvent, we increased the reference pressure in the z direction to four times that in the x and y, running this for 200 ns. Once the volume had equilibrated, a 100 ns relaxation period with standard pressure was performed. Finally, position restraints were removed and the systems were ran for a further 100 ns in the NPT ensemble to ensure the systems had equilibrated and the area per lipid (APL) remained constant. All systems were ran at 305 K and 1 bar pressure. Systems were then ran for 2.5 μs where the first 1.5 are regarded as equilibration for penetration of DMSO in the bilayer. The final 1 μs trajectories are the production runs and were used for our analysis.

5.2.2 Computational details

The potential energy function and interaction parameters employed for ceramide NS were based on the modified Martini coarse-grained forcefield[110] of Sovova[9], using a 4:1 mapping of atomistic to bead. Details of this forcefield can be found earlier in Section 2.7.4. DMSO parameters were described by the forcefield of Notman seen in previous works[72] and has been detailed previously in Section 1.7.5. The water was modelled using the Martini forcefield[110].

Simulations were carried out in the *NPT* ensemble using the GROMACS package[165], and employed the V-rescale thermostats[95] coupled separately to the lipid and solvent molecules with a time constant of 5 ps and a Berendsen barostat[94] with a time constant of 1 ps and compressibility of 3.0 x 10^5 bar^{-1} for semi-isotropic pressure coupling. The simulation cell was kept orthogonal by setting the off-diagonal terms of the compressibility matrix to zero. Standard periodic boundary conditions were applied in all three directions. All bonds were constrained using the LINCS algorithm[104] with a time step of 30 fs. The Lennard-Jones interaction cut-off was 1.2 nm using a shift function and a cut-off of 1.4 nm was used for the coulombic interactions. Results were analysed using the GROMACS package and MEMBPLUGIN[216] in VMD[217].

5.2.3 Testing the percentage of DMSO

Initially the concentration of DMSO in the standard 1Lx30 system was indentical to that of the previous atomistic work of Notman *et al.*[156]. But due to the softer interactions of CG particles, DMSO penetration into the bilayer occurred rapidly and resulted in the bilayer being unstable, ultimately disintegrating it. A number of test systems with varying concentrations of DMSO were carried out, detailed in Table 5.3, to find the largest concentration of DMSO for which a bilayer remains stable without penetration leading to disintegration. High concentrations again led to disintegration of the membrane, while a number of lower concentrations achieved penetration but did not destroy the membrane. The membrane of the 0.625% DMSO concentration retained its structural integrity and allowed no penetration. Therefore a 0.625% concentration of DMSO was used for our systems in this study.

DMSO Percentage			
DMSO / %	W beads	DMSO beads	Total
20	768	1536	3968
15	816	1152	3632
10	864	768	3296
5	912	384	2960
4.375	918	336	2918
3.75	924	288	2876
2.5	936	192	2792
1.25	948	96	2708
0.625	954	48	2666

Table 5.1: Percentages of DMSO in system

A breakdown of the contents of these systems can be seen in Table 5.2. We predict that as the amount of DMSO increases (larger solvent systems) there is a strong likelihood that DMSO penetration will occur, and these solvent effects will be investigated.

System Contents						
L	L/S	W	DMSO	W beads	DMSO beads	Total
128(1L)	10	1272	8	318	16	1998
128(1L)	30	3816	24	954	48	2666
128(1L)	70	8904	56	2226	112	4002
128(1L)	100	12720	80	3180	160	5004
256(2L)	10	2544	16	636	32	3996
256(2L)	30	7632	48	1908	96	5332
256(2L)	70	17808	112	4452	224	8004
256(2L)	100	25440	160	6360	320	10008
512(4L)	10	5088	32	1272	64	7992
512(4L)	30	15264	96	3816	192	10664
512(4L)	70	35616	224	8904	448	16008
512(4L)	100	50880	320	12720	640	20016
1024(8L)	10	10176	64	2544	128	15984
1024(8L)	30	30528	192	7632	384	21328
1024(8L)	70	31232	448	17808	896	32016
1024(8L)	100	101760	640	25440	1280	40032

Table 5.2: System Contents

5.2.4 Pure Water Control Systems

In addition to the four different solvent to lipid ratios and the four different bilayer sizes, four control systems were tested. A 1Lx10, 1Lx100, 8Lx10 and 8Lx100 system containing only water as a solvent. These act as a good comparison with their multi-solvent counterparts so as to confirm that any finite size or periodicity effects are due to size only and not purely chemical effects caused by the DMSO.

5.3 Results

5.3.1 Observations

After simulating various sized systems with differing solvent to lipid ratios, the behaviour of these systems can be split into three different categories; stable bilayers, low solvent systems leading to size effects, and high solvent systems leading to bilayer destruction. These observations have been condensed into a "phase" diagram, see Figure 5.1, where the different symbols represent each distinct category. It can be seen that a number of boundaries are present that are dictated either by the number of solvents, lipids or both.

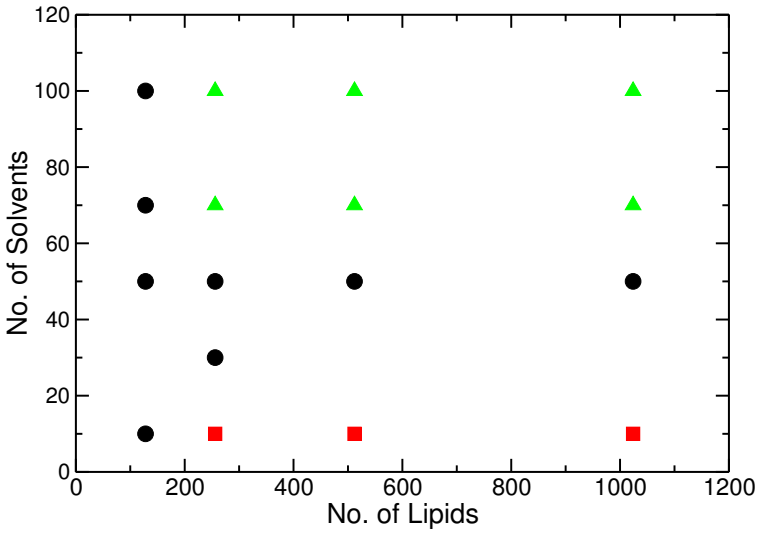

Figure 5.1: A phase diagram showing the state of each system. Systems with black circles are stable bilayers, red squares denotes systems with size effects.

Stable Systems

For the smallest systems (1L), a change in the solvent to lipid ratio did not change the general pattern of the bilayers. The bilayers remained stable with a two-leaflet configuration despite small amounts of DMSO penetrating the membranes. It can be seen that the majority of the DMSO molecules coagulate at the interface with the rest scattered in the bulk water or bilayer. As the solvent to lipid ratio is increased, the DMSO penetrates further into the bilayer and a greater number can be seen inside the membrane. In addition to the 1L systems, the 2Lx50, 4Lx50 and 8Lx50 systems also remained stable with penetration of DMSO into the bilayer.

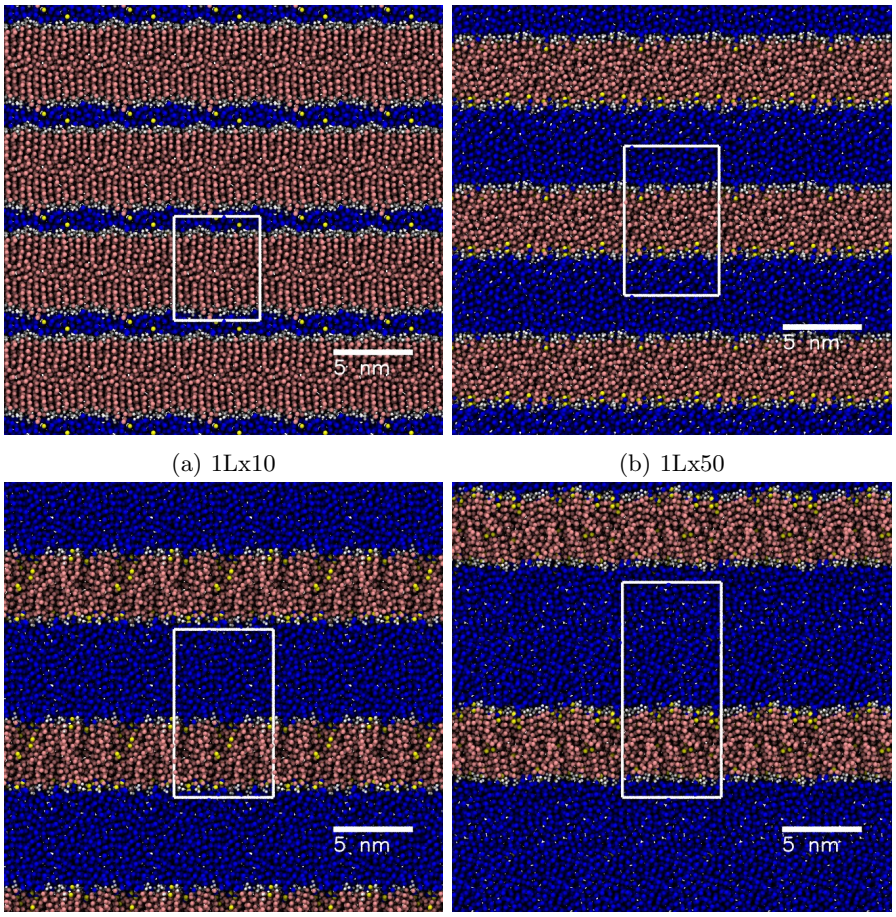

(a) 1Lx10 (b) 1Lx50

(c) 1Lx70 (d) 1Lx100

Figure 5.2: Stable 1L systems shown in a white simulation cell surrounded by periodic images. Ceramide headgroup in white, tails in grey, water in blue and DMSO in yellow.

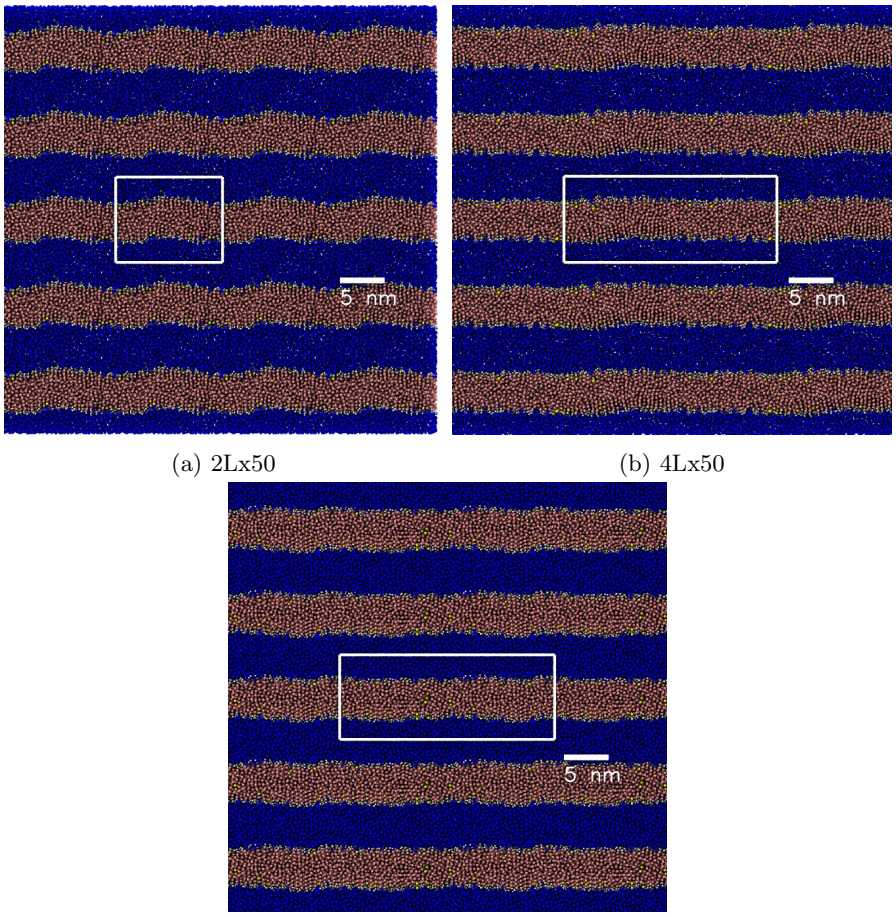

(a) 2Lx50

(b) 4Lx50

(c) 8Lx50

Figure 5.3: Stable 2Lx50, 4Lx50 and 8Lx50 systems shown in white simulation cell surrounded by periodic images. Ceramide headgroup in white, tails in grey, water in blue and DMSO in yellow.

Low solvent Systems

When there are systems with a low amount of solvent, for example 10 solvent per lipid, covering the surface area of larger membranes (2L, 4L and 8L), the solvent may be spread thin across this area. With a lack of solvent chamber, this can lead to interactions of the membrane with it's periodic image, often causing the solvent chamber to be separated into smaller sections. This in turn causes the structure of the bilayer to breakdown leading to penetration of DMSO. The magnitude of this effect is further exacerbated by the undulations of larger bilayers, as the interaction of the real and periodic images is more frequent. This could be deemed a periodicity effect and can seen in larger bilayer systems with low solvent levels.

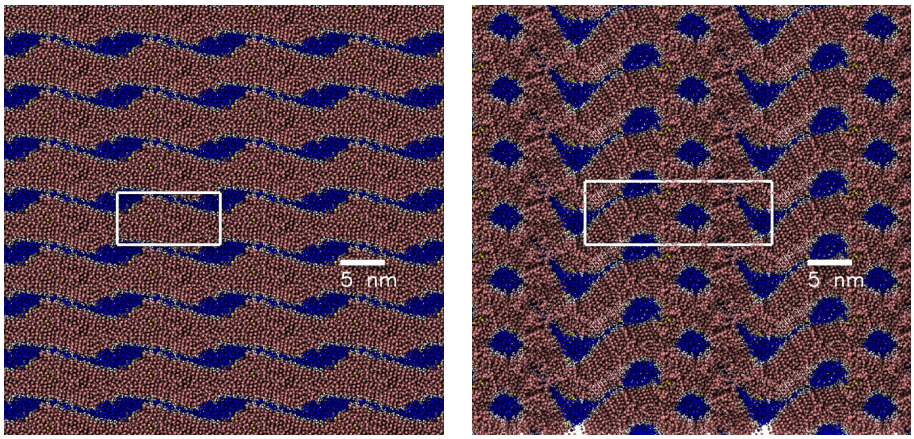

(a) 2Lx10 (b) 4Lx10

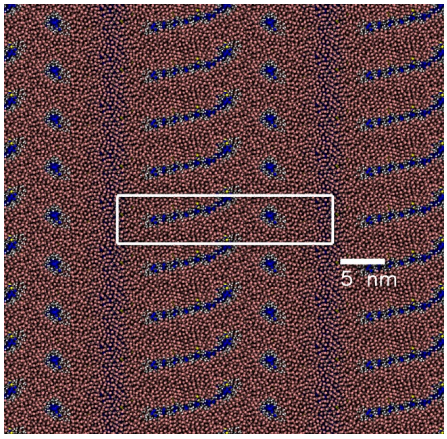

(c) 8Lx10

Figure 5.4: Low solvent systems shown in a white simulation cell surounded by periodic images. Ceramide headgroup in white, tails in grey, water in blue and DMSO in yellow.

High DMSO Systems

For the bilayer systems that have a high amount of DMSO molecules (70 and 100 solvent per lipid), it can be seen that DMSO agglomerates at the interface leading to penetration of DMSO and eventually water. Further increases of DMSO and water either break up the bilayer into smaller sections (2Lx70, 2Lx100, 4Lx70, 4Lx100) or completely disintegrate the bilayer (8Lx70 and 8Lx100).

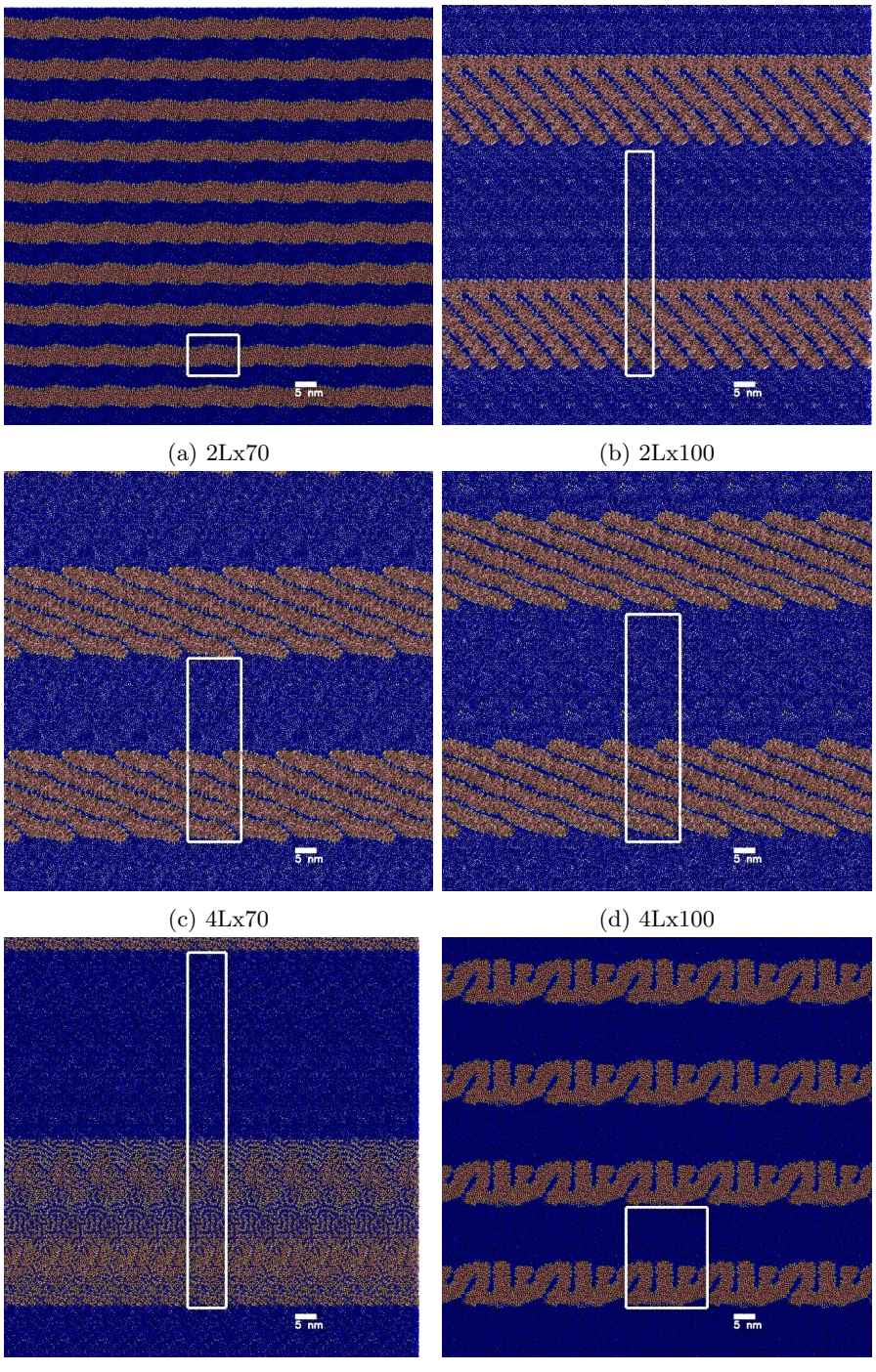

(a) 2Lx70 (b) 2Lx100

(c) 4Lx70 (d) 4Lx100

(e) 8Lx70 (f) 8Lx100

Figure 5.5: High DMSO systems shown in a white simulation cell surounded by periodic images. Ceramide headgroup in white, tails in grey, water in blue and DMSO in yellow.

5.3.2 DMSO density

To check that the systems had reached equilibrium, the density of DMSO was measured over time, convergence of the DMSO density at different parts of the system gives us confidence that further simulation time will not change the structure of the bilayer. Again, the systems are grouped into 3 sections according to the "phase" diagram (Figure 5.1) as their DMSO density plots are of similar nature.

Stable Systems

In general the 1L systems equilibrated well, producing clear peaks of DMSO at the interface and a plateau in the bulk region. Therefore there is no need to extend the simulation time for the 1Lx50 (Figure 5.6b), 1Lx70 (Figure 5.6c) and 1Lx100 (Figure 5.6d) systems. The 1Lx10 system (Figure 5.6a) doesn't have as well defined peaks due to the low solvent chamber between leaflets on the simulation cell and periodic image. DMSO appears to have transferred from the interface of one leaflet to the other, across the thin solvent chamber. There are some fluctuations of the DMSO peaks but they remain largely unchanged for the other stable systems (Figures 5.7a, 5.7b and 5.7c). Only in the 8Lx100 system is an increase in DMSO observed at the interface, but this remains constant for the final microsecond. As the amount of solvent in the 1L system is increased, both the DMSO density peaks at the interface increase, as well as the amount inside the bilayer.

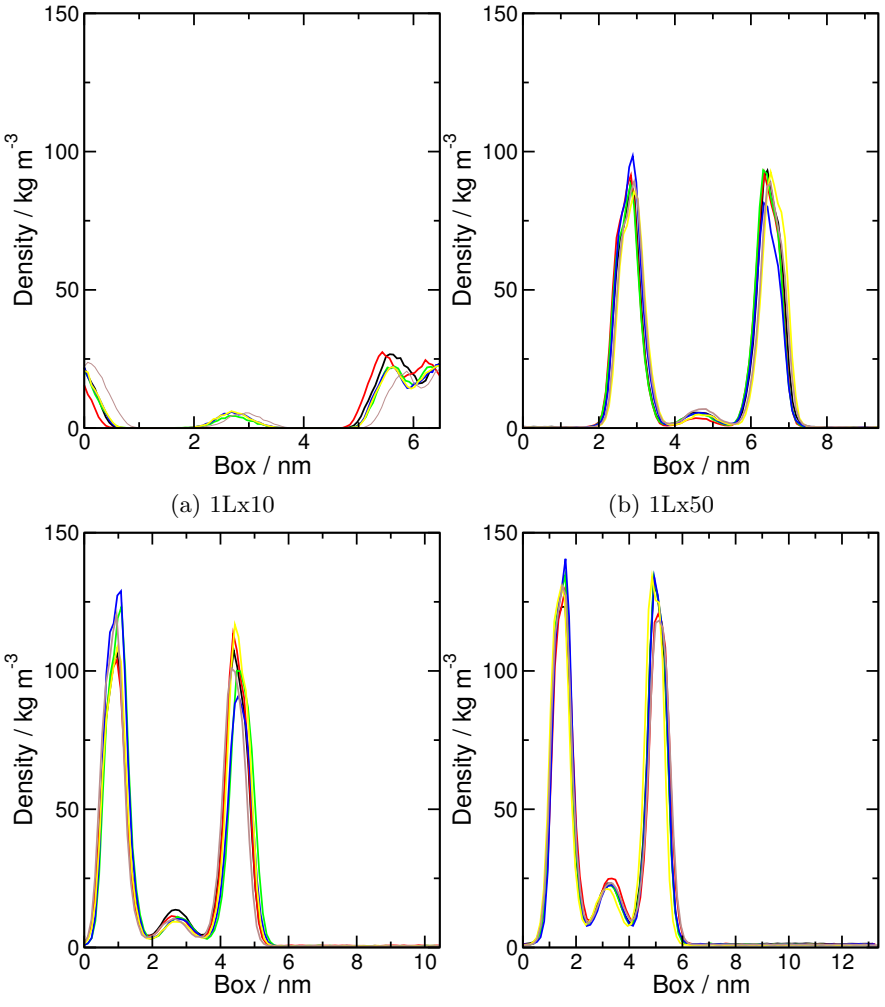

(a) 1Lx10 (b) 1Lx50

(c) 1Lx70 (d) 1Lx100

Figure 5.6: DMSO density over time for 1L systems. 0-500 ns in black, 500-1000 ns in red, 1000-1500 ns in green, 1500-2000 ns in blue, 2000-2500 ns in yellow and 2500-3000 ns in brown.

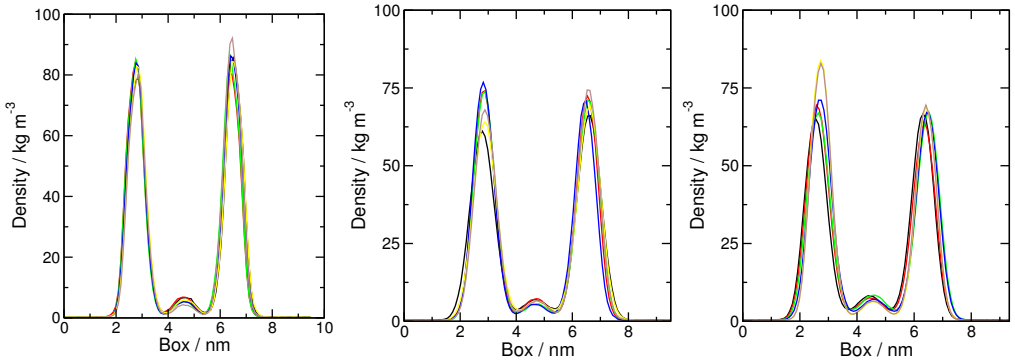

(a) 2Lx50 (b) 4Lx50 (c) 8Lx50

Figure 5.7: DMSO density over time for stable bilayer systems. 0-500 ns in black, 500-1000 ns in red, 1000-1500 ns in green, 1500-2000 ns in blue, 2000-2500 ns in yellow and 2500-3000 ns in brown.

Low Solvent Systems

As was seen in the observations of these systems, the periodicity effect caused by the low solvent chamber between leaflets leads to smaller sections of the bilayer with pools of water and DMSO. Hence, there is a lack of clear DMSO density peaks especially with the larger bilayers, see Figure 5.8c, where DMSO tends to uniformity.

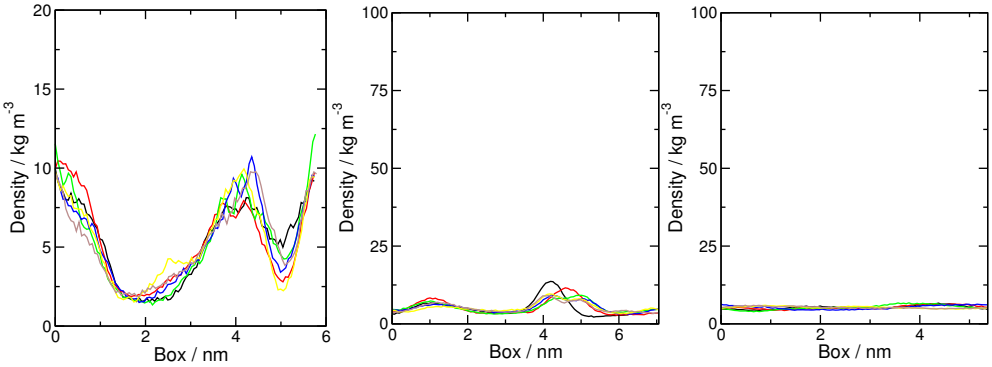

(a) 2Lx10 (b) 4Lx10 (c) 8Lx10

Figure 5.8: DMSO density over time for low solvent systems. 0-500 ns in black, 500-1000 ns in red, 1000-1500 ns in green, 1500-2000 ns in blue, 2000-2500 ns in yellow and 2500-3000 ns in brown.

High DMSO Systems

The systems that contain the highest amount of solvent, and thus the most DMSO molecules, all follow the same DMSO density pattern. There is still some DMSO within the bulk water with clear peaks at the interface but then high levels of DMSO within the bilayer. The DMSO density peaks, within the bilayer, fluctuate as DMSO from the interface penetrates the membrane, while other molecules are expelled.

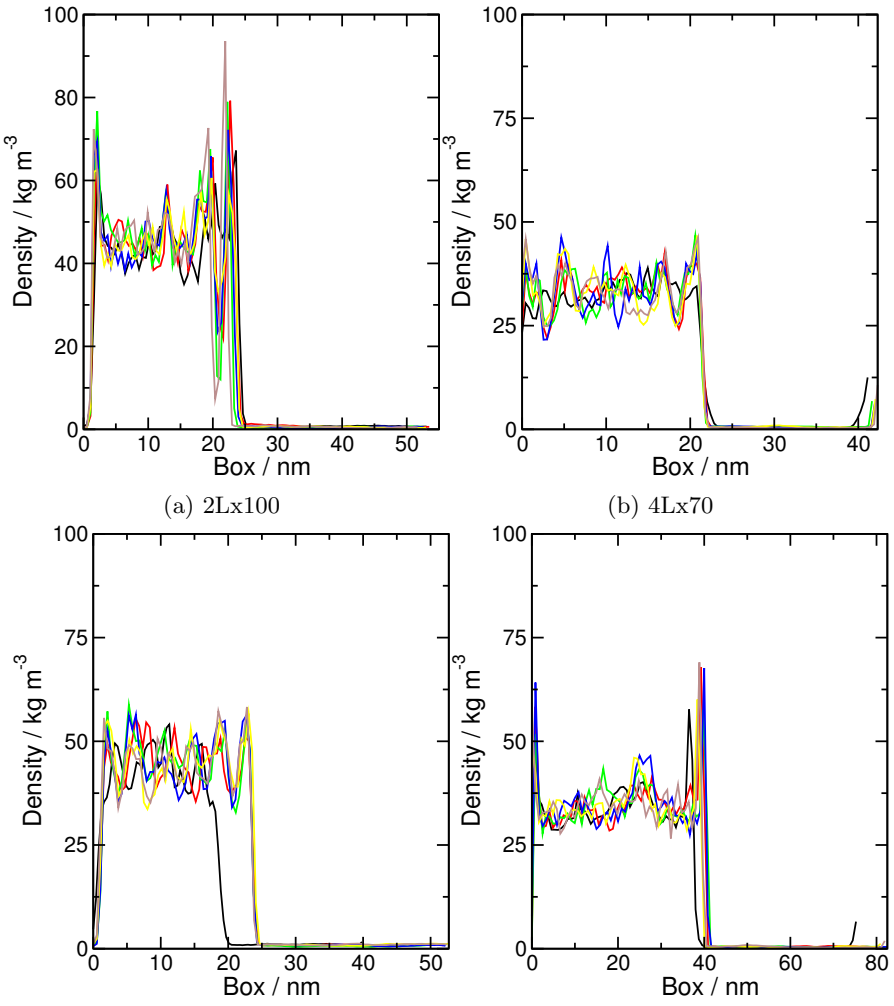

(a) 2Lx100

(b) 4Lx70

(c) 4Lx100

(d) 8Lx70

Figure 5.9: DMSO density over time for high DMSO systems. 0-500 ns in black, 500-1000 ns in red, 1000-1500 ns in green, 1500-2000 ns in blue, 2000-2500 ns in yellow and 2500-3000 ns in brown.

5.3.3 Density Profiles

Stable Systems

There is a small amount of penetration of DMSO into the bilayer in the 1L systems, as can be seen in the density profile Figure 5.10. The small amount of DMSO within the bilayers do not have a significant impact on the structure of the bilayer.

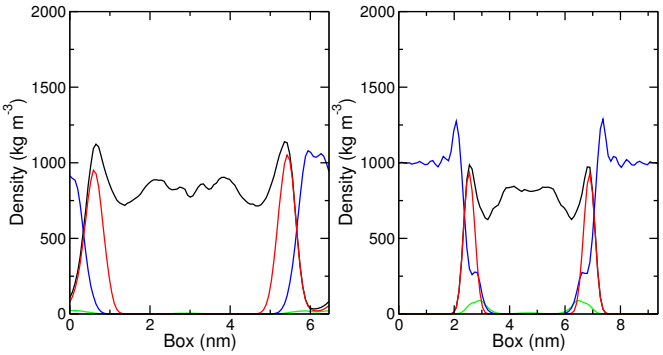

(a) 1Lx10 (b) 1Lx50

(c) 1Lx70 (d) 1Lx100

Figure 5.10: Density components of the 1L systems, with ceramide(black), water(blue), DMSO(yellow) and ceramide headgroup(red)

The DMSO density mainly centres around two peaks, at the interface of the bilayer, interacting with the lipid headgroups. Both the ceramide density and headgroups have well defined profiles. Water has favourable interactions with the hydrophilic ceramide headgroups and so high density peaks are seen in this area with the density plateauing indicating bulk water. The same type of profiles are also observed for the 2Lx50, 4Lx50 and 8Lx50 systems, see Figure 5.11.

It can be seen that as the amount of solvent, as thus DMSO increases, there is greater penetration of DMSO and larger density peaks in the centre of the bilayer. It is interesting to note that as the solvent increases the headgroup peaks decreases and becomes broader. No water is found inside the bilayers.

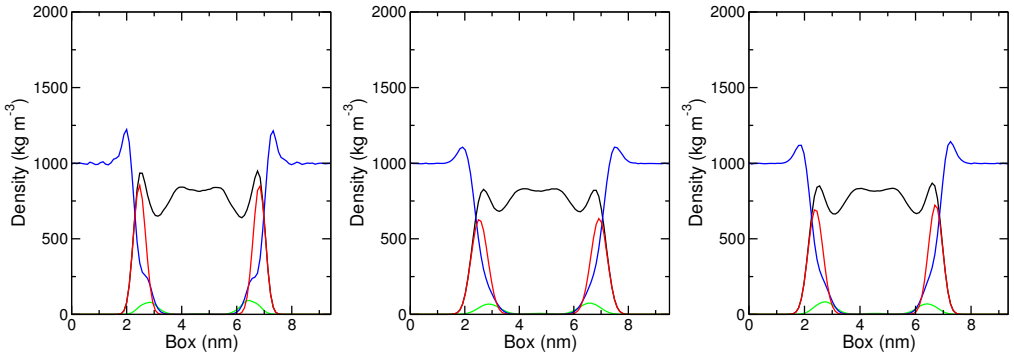

(a) 2Lx50 (b) 4Lx50 (c) 8Lx50

Figure 5.11: Density components of the 1L systems, with ceramide(black), water(blue), DMSO(yellow) and ceramide headgroup(red)

Low Solvent Systems

In the low solvent systems the ceramide density profile has less structure and has been disrupted. This is clear in the 4Lx10 system (Figure 5.12b), where water is enclosed within the ceramides. In the 8Lx10 system (Figure 5.12c) all the components are becoming uniform throughout the simulation cell.

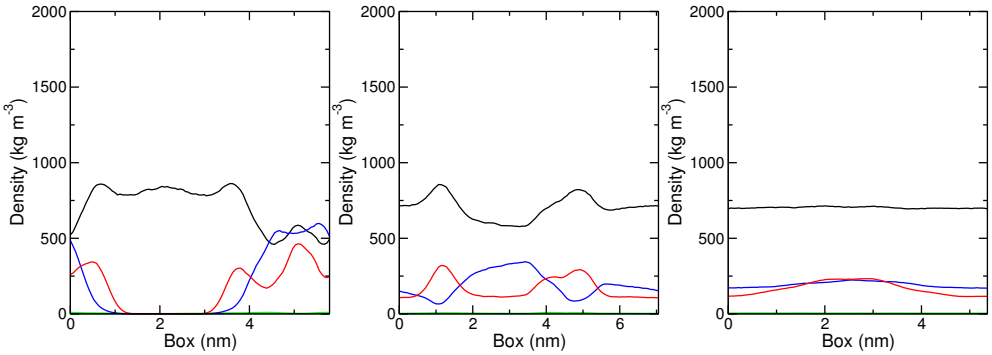

(a) 2Lx10 (b) 4Lx10 (c) 8Lx10

Figure 5.12: Density components of the 2L systems, with ceramide(black), water(blue), DMSO(yellow) and ceramide headgroup(red)

High DMSO Systems

In the high solvent systems the ceramide density profile has less structure and has been disrupted (Figure 5.13). High amounts water and DMSO have penetrated into the membrane causing it to disintegrate.

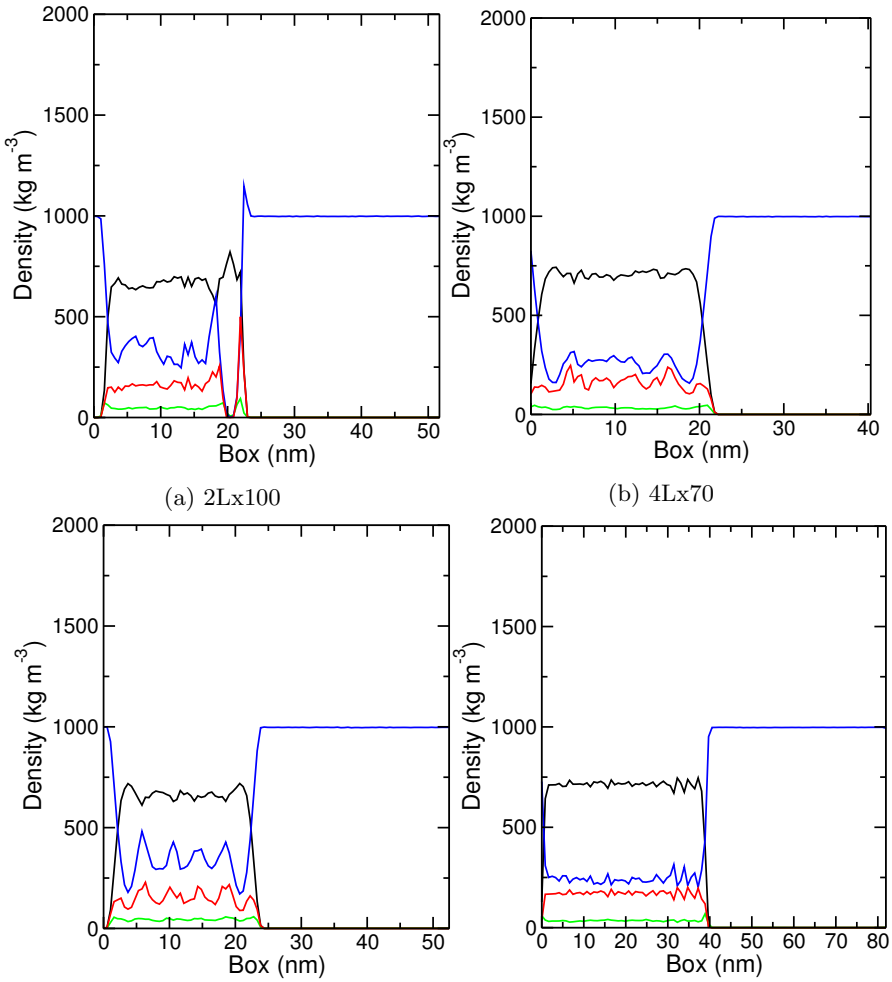

(a) 2Lx100

(b) 4Lx70

(c) 4Lx100

(d) 8Lx70

Figure 5.13: Density components of the high DMSO systems, with ceramide(black), water(blue), DMSO(yellow) and ceramide headgroup(red).

5.3.4 DMSO distribution

To better quantify the DMSO distribution within the stable systems, the percentage of DMSO found at the interface, bulk or inside the bilayer was calculated, see Table 5.3. The interface was defined as the distance between the peak of the headgroup density and the plateau of the bulk water. The bulk was defined as plateau of the water density and the inside of the bilayer was defined as the distance between the headgroups of both leaflets. Only the bilayers that remained stable were used as it is difficult to define clear sections in the low and high solvent systems.

For the 1Lx10 system, the majority of the DMSO was found within the bilayer itself at 53.6%, 33.4% in the bulk water and only 13.0% at the interface. As the amount of solvent is increased in the 1L system, the DMSO agglomerates at the interface at 92.2% while approximately only 7.4% penetrates into the bilayer, the rest is situated within the bulk water. Increasing the amount of solvent for the 1L system leads to an large amount of DMSO at the interface. Further increases in DMSO concentration

causes a decrease in the percentage of DMSO at the interface, ultimately an increase in penetration to the bilayer and situated in the bulk. For the other systems with 50 solvents per lipid the DMSO is distributed significantly at the interface, around 95%, with ≈4.5% inside and ≈0.5% in bulk.

DMSO Distribution			
System	Interface (%)	Bilayer (%)	Bulk (%)
1Lx10	13.0	53.6	33.4
1Lx50	92.2	7.4	0.4
1Lx70	91.8	7.0	1.2
1Lx100	87.3	10.0	2.7
2Lx50	95.8	3.8	0.4
4Lx50	94.8	4.7	0.5
8Lx50	94.9	4.6	0.5

Table 5.3: Distribution of DMSO within bilayer.

5.3.5 Structural Properties

Both the APL and thickness of the stable bilayer systems were calculated, Table 5.4, to give an indication of the effect of DMSO on the structural properties of the ceramide bilayer. The APL was calculated from the xy area of the bilayer over the number of lipids in a leaflet using the last 300 ns of the production run. The thickness is calculated as the distance between the peaks of the H1 bead headgroup density over the final 500 ns of the production run, which lie on different leaflets.

Structural Properties		
System	APL (nm^2)	Thickness (nm)
1Lx10	0.459 ± 0.003	5.029
1Lx50	0.562 ± 0.007	4.535
1Lx70	0.603 ± 0.006	4.324
1Lx100	0.625 ± 0.008	4.456
2Lx50	0.554 ± 0.003	4.567
4Lx50	0.549 ± 0.002	4.610
8Lx50	0.559 ± 0.002	4.620

Table 5.4: Area per lipid and thickness for stable systems with DMSO.

The APL for all of these bilayers are larger than the standard 0.4 nm^2 for atomistic CER bilayers. The smallest system 1L×10 has an APL of 0.459 nm^2 and this increases at higher solvent to lipid ratios with a 0.625 nm^2 APL for the 1L×100 system. The

values of APL for the 50 solvent per lipid ratio are similar regardless of the bilayer size.

The thickness generally decreases, from 5.029 nm, as a greater amount of solvent as thus DMSO, is added. This decreases to 4.324 nm for the 1L×70 system, but then has a slight increase compared with the 1L×100 at 4.456 nm. Again, there is not much change in the thickness when changing the size of the bilayer and maintaining the same solvent to lipid ratio.

5.4 Discussion

For all the systems larger than 1L with 10 solvent molecules per lipid (2L×10, 4L×10 and 8L×10), the size of the solvent chamber was rather small enabling the lipid headgroups to interact with the periodic image of the opposite bilayer which in turn leads to the disruption of the structural integrity of the bilayer. Solvent becomes encapsulated by the lipids and the lipids form a hexagonal phase. The structural integrity of the 1L×10 system is not disrupted despite having the same solvent to lipid ratio. It is likely that the undulations that are seen in larger membranes provide a way for the distance between a real leaflet and image leaflet to be lessened to an extent where they can interact where the smallest 1L×10 system tends to be flat. This in itself could be classed as a periodic effect, with the amount of solvent to correctly model bilayer systems having been already discussed in Chapter 3 for atomistic CER bilayers with varying solvent levels, and concluding that 10 water molecules per lipid is enough to be considered bulk, it stands to reason that the simplification of coarse-graining the system may also be impacting these periodic effects. Another factor could be the accuracy of the forcefield, as shown by the moderately small percentage of DMSO (0.625%) required to penetrate and even disintegrate the bilayer, as opposed to the higher concentrations used in previous atomistic simulations[156].

It can be seen for the smaller stable bilayers (1L×10 and 1L×50), that DMSO only shows a small penetration enhancement effect, whereas for larger bilayers (2L×50, 4L×50 and 8L×50) and solvent to lipid ratios (1L×70 and 1L×100), a greater amount of penetration can be found. This seems to suggest that even though there is the same percentage DMSO in each system, the actual number amount of DMSO is important in its mechanism of penetration. Greater addition of DMSO to the solvent phase leads to agglomeration at the interface due to favourable interactions with the hydrophilic ceramide headgroups, as opposed to bulk solvent interactions. The propensity of DMSO at the interface leads to a build up of DMSO before any penetration takes place. It is plausible to suggest that further simulation time could yield penetration despite minimal changes in the DMSO density over time. In the large systems with high concentrations of DMSO (2L×70, 4L×70, 8L×70, 2L×100, 4L×100 and 8Lx100) has a significant effect on the structural integrity of the bilayers. The large permeability enhancing effect of DMSO leads to significant penetration of DMSO and water into the

bilayers. This in turn leads to the breakdown of the bilayer structure.

From the stable density plots (Figure 5.10) it is clear that as the amount of DMSO added to the system increases, the density at the interface becomes larger, as well as the amont of DMSO within the bilayer. As the interface is flooded with more solvent the CER lipid density becomes less defined. The water density starts to shift inwards, suggesting some water molecules are beginning to penetrate deeper in the headgroup region. The headgroup density peaks shrink in line with the CER density. There is no difference between the DMSO density peaks at the interface for the stable systems with 50 solvent molecules per lipid regardless of bilayer size, see Figure 5.11. For the low solvent systems, the lack of a big enough solvent chamber to prevent leaflet interaction is evident in Figure 5.12. The ceramide density has no clear structure and eventually has uniformity across the simulation box for the large 8L×10 system. In the high DMSO concentration systems, a large amount of DMSO and water has penetrated into the bilayer, see Figure 5.13 causing it to break up on itself. The change in density of DMSO over time was plotted for the three different phases, see Figures 5.6, 5.7, 5.8 and 5.9. The change in DMSO halted generally after a microsecond, where further simulation time did not yield a significant change.

The DMSO distribution as a percentage of the density has been calculated at the interface, within the bilayer and in the bulk solvent, see Table 5.3, for each of the stable bilayer systems. In the 1L×10 system the majority of the DMSO is found in the bulk (53.6%), this can be attributed to the fluctuation of a relatively small number of DMSO molecules within the system. For the larger concentrations of DMSO in the 1L systems, the DMSO is distributed significantly at the interface, starting at 92.2% for the 1L×50 and decreasing hereafter. Although in real terms the density at the interface did increase, the fact that the overall percentage did not, indicates that the interface is becoming saturated. As the ceramide headgroups become saturated, addition of DMSO leads to an increase in the bulk from 0.4 to 2.7% in the 1L×50 and 1L×100 systems respectively. An increase in the penetration of DMSO into the bilayer is also observed as a greater number of DMSO molecules at the interface act as spacers between lipid headgroups and increase the permeability of the membrane. There is little change in the DMSO distribution for 50 solvents per molecule when the bilayer size is increased, as there is the same ratio of DMSO molecules to binding sites and so a change in the rate of penetration does not occur.

As the size of the bilayer increases from 1L to 8L the larger surface area results in a larger number of binding sites for DMSO at the interface and leads to an increase in the percentage of DMSO at the interface. The larger amount of DMSO at the interface facilitates in the disruption of the lateral CER-CER hydrogen bonding network leading to a fluidisation of the bilayer, which has been seen for systems of high solvent to lipid ratio and thus high DMSO content. This more permeable state allows deeper

penetration of DMSO into the bilayer and even small amounts of water. An increase in the DMSO to solvent ratio has a significant effect on the phase of the bilayer. Just by doubling the DMSO concentration from 0.625 to 1.25% leads to a rapid fluidisation of the bilayer, lipid extraction and eventually disintegration. An increase in the solvent to lipid ratio ultimately makes more DMSO molecules available to adsorb at the interface and again facilitates added disruption of the bilayer. As seen with previous atomistic simulations[29], a fluidisation of the bilayer occurs upon the increase of DMSO whether that be *via* an increased concentration, through a higher solvent to lipid ratio or a greater number of binding sites *via* a larger surface area as seen in these CG systems.

Although comparisons with previous atomistic simulations are difficult to do due to the different percentage of DMSO in the solvent, we can observe similar trends as both are artificially increasing the number of DMSO molecules, by increasing the mol fraction in the atomistic simulations or through a larger solvent to lipid ratio. At larger DMSO values both atomistic and CG simulations lead to a liquid-crystalline phase, and at particularly high concentrations, disintegration. Agglomeration of DMSO to the interface and penetration into the bilayer causes a number of structural changes, most notably the area per headgroup and the membrane thickness (calculated values for the stable bilayers are given in Table 5.4). As the solvent per lipid ratio is increased, the APL increases too, reaching a value of 0.625 nm^2 for the 1L×100. This is rationalised as the DMSO disrupting the lateral headgroup interactions by acting as spacers between the CERs, this in turn causes an increase in the APL. This trend is seen in atomistic simulations, with a range of 0.60-0.70 nm[29]. The CG systems studied here have a slightly smaller APL, between 0.45-0.65 nm, which is to be expected as a higher concentration of DMSO was used. Systems with the 50 solvent per lipid ratio has similar APL values. As the APL increases, there is more space for the lipid tails to fill, which in turn decreases the bilayer thickness. The thickness of a pure ceramide bilayer has a thickness of 5 nm in the atomistic calculations of Notman *et al.* but significantly decreases to roughly 3.5 nm at mol fractions greater than 0.4, the CG simulations follow this trend going from 5.029 nm to 4.324 nm.

DMSO has been shown to alter the membrane structure in a concentration dependent manner in phospholipid bilayers using a variety of techniques[161,256–259]. Infrared spectroscopy indicates that DMSO causes dehydration of the headgroup region[260] by replacing water in the inner regions of the headgroup[?] . The suggested mechanism is that DMSO binds directly to the choline headgroup, displacing the choline bound water, through electrostatic interactions. This was determined through a combination of specular neutron reflection, Brewster angle microscopy and MD simulations[?] . Shashkov *et al.* also acknowledge the strong interactions between DMSO and water and have attributed part of this dehydration to their chemistry. An increase in the mole fraction of DMSO in water, leads to a linear increase of the pre- and main transition temperatures for a number of phospholipids when examined by DSC and X-ray diffrac-

tion[161]. This is accompanied by reductions in the multilamellar repeat distance due to a reduction in the solvent chamber space between bilayers. As DMSO molecules occupy the area just beneath the headgroups, they act as spacer molecules pushing the headgroups apart, leading to an increased area per lipid. An increases in the headgroup area enables lipid tails to expand into a larger free volume reducing the thickness[261]. With high concentrations of DMSO in the presence of cholesterol-containing membranes the formation of pores can occur. Under the influence of DMSO, the formation of pores increases the permeability of water, calcium ions and small drug molecules in living cell membranes[262].

The interaction of DMSO with skin lipids is similar to that of phospholipids. The CERs are found in a more organised state, the gel phase, at physiological temperatures rather than the liquid-crystalline phase of phospholipids. The strong lateral hydrogen bonding network of the SC lipids require high concentrations of DMSO to create a significant permeability enhancing effect[50,69,263]. At these concentrations the bilayers are fluidised[51] and undergo a gel-to-liquid crystalline phase transition. At low concentrations DMSO accumulates at the interface forming hydrogen bonds at the expense of water-lipid hydrogen bonds, allowing them to partition between headgroups and slowly into the bilayer. DMSO can also induce pores in CERs but has a lower probability due the stronger lipid-lipid interactions.

There are similar observations between these simulations and those of experiment. Low concentrations of DMSO can be seen to accumulate at the interface rather than in the bulk due to DMSO's high propensity to form hydrogen bonds with the CER headgroups and displacing water from the interface. Higher concentrations are seen to create a permeability enhancing effect on the bilayers, allowing penetration of DMSO into the bilayers. Structural changes occur leading to a less organised, thinner membrane with larger area per lipid, indicative of a gel-to-liquid crystalline phase change known to happen experimentally. The formation of pores are not seen in these simulations. It can be seen here that size and solvents effects have an important contribution to the penetration enhancement of small molecules such as DMSO and such effects need to be considered carefully when setting up simulations of that nature.

5.5 Conclusions

By studying different ceramide bilayers sizes with different concentrations of mixed water-DMSO solvents, we were able to observe any finite size or periodicity effects that may impact the true results of the simulations. We observed what could either be a periodic artifact caused through lack of solvation for larger scale bilayers due to interactions between a leaflet and its periodic image or a different phase. It is well known that high concentrations of such solute can lead to a fluidisation of membranes as DMSO molecules at the interface disrupt lateral hydrogen bonding leading to the formation of pore that are not energetically unfavourable. The study shows that even by keeping the percentage of DMSO the same throughout, an increase in the actual number of DMSO molecules has a significant penetration enhancing effect and can lead to fluidising membranes. Therefore, our results indicate that one should be careful when simulating permeation enhancers with different sized membranes. It suggests that a solvent chamber greater than 10 solvent per lipid is necessary for system sizes of at least 256 lipids to avoid finite size effects in simulations of lipid membranes in mixed solvents. A solvent to lipid value of 70 or greater should be avoided for larger systems as there is a high amount of DMSO that causes fluidisation of the membrane. It remains to be seen in our results can be generalised to other lipid bilayer systems in different solvent mixtures but the use of CG model could be used to study larger systems.

Chapter 6

Conclusions

The skin is the largest organ in the human body where its main function is to provide a protective barrier from the external environment. An understanding of the skin barrier is essential for: applications in medicine, pharmaceutics and the personal care industry; the assessment of saftey, toxicity and bioavailability of chemicals that may come into contact with skin; and the development of technologies that interface with skin, such as haptic devices.

The lipid matrix within the SC, the topmost layer of skin, is believed to be the main contributor to the skin's barrier properties. A major problem, which impedes progress in the applications areas mentioned above, is that the organisation of the SC lipids into the lamellar layers and the contributions of the lipids to the barrier properties of the skin remains poorly understood. Furthermore, knowledge of how bioactive molecules or skin formulation ingredients interact with the skin lipids and modulate their barrier properties is limited.

This thesis has attempted to address these issues through the use of MD computer simulations of model bilayers of SC lipids under a variety of different conditions. The use of MD simulations has allowed these membranes to be studied at the atomistic level, which is not accessible through conventional experiments. MD simulations themselves suffer from limitations and it is important to have a good grasp of how the choices made by the researcher when setting up the simulation may impact the results. In this thesis the effect of changing the size of the simulated bilayer system (both number of lipids and number of solvent molecules) have been explored in detail.

Water plays an important role in the structure and dynamics of lipid bilayers. In the literature, most MD simulation studies on skin focus on single, fully hydrated SC lipid bilayers despite experiments indicating that only a small amount of water exists within stacks of lipid lamellae. In Chapter 3, the first MD simulations of two CER bilayers stacked on top of each other were reported. Six double-ceramide bilayer systems were simulated with varying amounts of water placed between the bilayers, ranging from no water to fully hydrated bilayers. The aim of the study was to determine the effects of

the level of hydration on the structural and dynamic properties of the bilayers and to further our understanding of how the water content of skin contributes to its optimal flexibility and permeability, which is required for normal function. Furthermore, the double-bilayer models were chosen to better (compared to individual bilayers) represent the skin lipid lamellae and allow for the calculation of inter-leaflet HBs between bilayers that were separated by a low number of water molecules per lipid.

The results presented in Chapter 3 show that the hydration level within the lipid matrix has a direct impact on the bilayer conformation and thus the barrier properties of the SC. At low hydration a pooling effect is observed on the bilayer surface rather than a uniform distribution of water molecules. This rearrangement of water molecules on the surface is likely driven by the change in entropy associated with increasing the disorder of the water and reducing the interfacial tension between water and the CERs. This water pooling affects the order and orientation of the CERs. A water pool allows the spread of CERs from a packed conformation to form HBs with water. To compensate there is an altering of the lipid tilt angle, which in turn modifies other structural properties of the bilayer. At low levels of hydration the APL becomes slightly larger compared with high hydration levels and in turn the membrane thickness decreases. As the hydration level is lowered, the amount of CER-water HBs decreases and these are replaced with CER-CER HBs between adjacent bilayers. The lateral hydrogen bonding network within a bilayer remains unchanged. Therefore it is suggested that lowering the hydration strengthens the interaction between the lipid lamellae and improves the overall integrity of the SC. This pooling effect of water on the bilayer surface is significant because it indicates a non-continuous aqueous phase could be present in the SC. That is, the observation of distinct water pools essentially eliminates the possibility of a lateral polar pathway through the SC as a molecule would have to transverse energy barriers to move from the pool to a dry region on the bilayer surface. The work done in this chapter has laid the foundation for the development of more realistic SC models in the future, which could combine the low level of hydration and double-bilayer arrangement developed here with multicomponent-lipid bilayers and/or additive molecules.

Chapter 4 of the thesis considers the effect of the unsaturated FFA OA on the structure and permeability of CER bilayers. OA is of particular interest in skin-lipid studies due to its common use as a skin penetration enhancer for drug delivery. Due to its non-polar nature and the fact that FFAs are a major component of the SC lipids it is expected that OA partitions into the SC lipid lamellae. There have been a number of hypothesised mechanisms for how OA interacts with the skin lipids to facilitate the penetration of small molecules. The most prominent hypotheses are that (i) OA disperses within the SC lipids and disrupts their packing and fluidises the membrane or that (ii) OA phase separates and forms a pool in the membrane; permeants may diffuse through the pool or along the interface between the pool and the SC lipids. In Chapter 4, three possible pathways along which a water molecule could permeate through the

SC lipids in the presence OA were analysed through the use of PMCF calculations. These were: (i) through a pure CER bilayer; (ii) through a pure OA bilayer; and (iii) through a mixed CER/OA bilayer. From this the most likely pathway for permeation was deduced and a mechanism of action put forward.

It was determined through free energy calculations and the calculation of permeability coefficients, that a mixed system of CER and OA has a greater permeability than either of the pure systems and thus would be a more favourable pathway for permeants, such as water, to migrate through. It was important to note that the pure OA system was more permeable than the pure CER bilayer suggesting that in the case of a phase separated system an OA pool would still be considered a more favourable pathway due to the lower free energy barrier. In the mixed CER/OA bilayer, it was shown that OA lowers the free energy barrier by disrupting the lateral hydrogen bonding network between the CER headgroups by forming far fewer hydrogen bonds. OA also reduces the ordering of CER tails due to some of the OA molecules adopting the *cis* conformation and having a kinked structure. Calculation of the permeability coefficients of these three different pathways has allowed us to predict which will be most likely favourable. Through the understanding of this mechanism of action, one can design more efficient drug delivery strategies using a penetration enhancer such as OA.

Chapter 5 explores some of the methodological issues to be considered when simulating lipid bilayers with additive molecules such as penetration enhancers. The effects of concentration dependent penetration enhancers on lipid bilayers have been studied abundantly in the literature. In these studies the size of the bilayer and the total number of solvent molecules is usually fixed at an arbitrarily chosen value, while the concentration of penetration enhancer is altered. A major problem is the saturation of the interface for given concentrations leads to unknown effects. Therefore in Chapter 5, MD simulations of a number of CG CER bilayer systems surrounded by a mixture of water and DMSO, a well-known penetration enhancer, were carried out. The effects of systematically changing the size of the bilayer and the total number of solvent molecules were analysed. Observations of the solvent effects on these systems, by altering the solvent to lipid ratio, were compared with the previous atomistic MD simulations of similar systems.

The simulations revealed that at low solvent to lipid ratios and larger bilayers, the small solvent chamber allows interactions of the CER bilayer with its periodic image causing disruption to the bilayer conformation and leading to a change to the hexagonal phase. The effect is more prominent in the larger the system due to increased undulations. Solvent effects are observed when the amount of DMSO at the interface is higher for larger bilayer systems despite the same solvent to lipid ratio. The larger surface area can accommodate a greater number of DMSO molecules at the interface, but due to the penetration enhancement effect of DMSO, the bilayers become fluidised and are

filled with DMSO. An increase in the solvent to lipid ratio leads to an increase in the APL and a decrease in membrane thickness. The trends of these structural changes compare well with experiment and previous simulations. High solvent to lipid ratios cause disintegration of the bilayers. From these simulations, we deduce that, in MD simulations, it is the absolute number of penetration enhancer molecules that is important and not just the concentration. It is recommended to have a minimum solvent chamber to avoid periodic artifacts. It can be seen here that size and solvents effects need to be considered carefully when setting up simulations that contain a penetration enhancing solvent such as DMSO.

A limitation of the model used in this thesis is that it is assumed that the simple CER model bilayers are a good representation of real skin due to CER being the most abundant component of the SC that dictates the major properties of the lipid matrix. A more accurate model of the skin using CHOL and FFA as well as CER would be desirable but requires additional computational power to equilibrate the mixtures. A simple model could allow for clearer characterisation of effects on the membrane and give insights into the structure and how this relates to the barrier properties of the skin. The length scales of the atomistic simulations were limited by the size of the systems compared to that of the CG, where hundreds of nanoseconds could be attained.

The investigations in this thesis could be extended to further improve the understanding of the structure and organisation of the SC and how it contributes to the barrier function of the skin. In Chapter 3, the variation of hydration could be extended to both larger multilayers (>3) and a more complex model containing CHOL and FFAs. A more complex model could also be used in Chapter 4 to obtain permeability coefficients closer in magnitude to that of experiment. The variation of OA concentration could be explored, as the effect of a small concentration was simulated. A fourth possible pathway for the CER/OA systems could also be envisaged: water could permeate through the interface between a pool of OA and a pool of CER in a phase separated system. To better probe this barrier to permeation along the z-axis, free energy calculations could be performed while constraining the permeating water in both the x and y directions.

Bibliography

[1] Notman, R. Molecular Simulations of the Interaction of Penetration Enhancing Molecules with Lipid Bilayers. Ph.D. thesis, Kings College London, London, UK, 2007.

[2] Janssens, M.; van Smeden, J.; Gooris, G. S.; Bras, W.; Portale, G.; Caspers, P. J.; Vreeken, R. J.; Hankemeier, T.; Kezic, S.; Wolterbeek, R.; Lavrijsen, A. P.; Bouwstra, J. A. *Journal of Lipid Research* **2012**, *53*, 2755–2766.

[3] Vávrová, K.; Kováčik, A.; Opálka, L. *Acta Facultatis Pharmaceuticae Universitatis Comenianae* **2017**, *64*.

[4] Forslind, B. *Acta dermatovenereologica* **1994**, *74*, 1–6.

[5] Bouwstra, J. A.; Dubbelaar, F. E.; Gooris, G. S.; Ponec, M. *Acta dermatovenereologica Supplementum* **2000**, *208*, 23–30.

[6] Hadgraft, J.; Lane, M. E. *Phys. Chem. Chem. Phys.* **2011**, *13*, 5215–5222.

[7] Barry, B. W. *Nature Biotechnology* **2004**, *22*, 165.

[8] Das, C.; Noro, M. G.; Olmsted, P. D. *Biophysical journal* **2009**, *97*, 1941–1951.

[9] Sovová, Ž.; Berka, K.; Otyepka, M.; Jurečka, P. *The Journal of Physical Chemistry B* **2015**, *119*, 3988–3998.

[10] Elias, P. M. *The Journal of investigative dermatology* **1983**, *80 Suppl*, 44s–49s.

[11] Madison, K. C.; Swartzendruber, D. C.; Wertz, P. W.; Downing, D. T. *The Journal of investigative dermatology* **1987**, *88*, 714–718.

[12] Bouwstra, J. a.; Dubbelaar, F. E.; Gooris, G. S.; Weerheim, a. M.; Ponec, M. *Biochimica et Biophysica Acta* **1999**, *1419*, 127–136.

[13] Masukawa, Y.; Narita, H.; Shimizu, E.; Kondo, N.; Sugai, Y.; Oba, T.; Homma, R.; Ishikawa, J.; Takagi, Y.; Kitahara, T.; Takema, Y.; Kita, K. *Journal of lipid research* **2008**, *49*, 1466–1476.

[14] Norlén, L.; Nicander, I.; Lundsjö, a.; Cronholm, T.; Forslind, B. *Archives for dermatological research Archiv fur dermatologische Forschung* **1998**, *290*, 508–516.

[15] Moore, D. J.; Rerek, M. E.; Mendelsohn, R. *The Journal of Physical Chemistry B* **1997**, *101*, 8933–8940.

[16] David J. Moore, M. E. R. *Acta Dermato-Venereologica* **2000**, *80*, 16–22.

[17] Ohta, N.; Hatta, I. *Chemistry and Physics of Lipids* **2002**, *115*, 93–105.

[18] Wegener, M.; Neubert, R.; Rettig, W.; Wartewig, S. *Chemistry and Physics of Lipids* **1997**, *88*, 73–82.

[19] Bouwstra, J. A.; Gooris, G. S.; Dubbelaar, F. E.; Weerheim, A. M.; Ponec, M. *The journal of investigative dermatology Symposium proceedings the Society for Investigative Dermatology Inc and European Society for Dermatological Research* **1998**, *3*, 69–74.

[20] Neubert, R.; Rettig, W.; Wartewig, S.; Wegener, M.; Wienhold, a. *Chemistry and Physics of Lipids* **1997**, *89*, 3–14.

[21] Schreiner, V.; Pfeiffer, S.; Lanzendörfer, G.; Wenck, H.; Diembeck, W.; Gooris, G. S.; Proksch, E.; Bouwstra, J. *Journal of Investigative Dermatology* **2000**, *114*, 654–660.

[22] Moore, D. J.; Rerek, M. E.; Mendelsohn, R. *The Journal of Physical Chemistry B* **1997**, *101*, 8933–8940.

[23] Imokawa, G.; Abe, A.; Jin, K.; Higaki, Y.; Kawashima, M.; Hidano, A. *Journal of Investigative Dermatology* **1991**, *96*, 523–526.

[24] Bouwstra, J. A.; Gooris, G. S.; Vries, M.-d.; van der Spek, J. A.; Bras, W. *International Journal of Pharmaceutics* **1992**, *84*, 205–216.

[25] Bouwstra, J. A.; Gooris, G. S.; Bras, W.; Downing, D. T. *Journal of Lipid Research* **1995**, *36*, 685–695.

[26] Bouwstra, J. A.; Gooris, G. S.; van der Spek, J. A.; Bras, W. *Journal of Investigative Dermatology* **1991**, *97*, 1005–1012.

[27] Norlén, L. *The Journal of investigative dermatology* **2001**, *117*, 830–836.

[28] Pandit, S. a.; Scott, H. L. *The Journal of chemical physics* **2006**, *124*, 14708.

[29] Notman, R.; den Otter, W. K.; Noro, M. G.; Briels, W. J.; Anwar, J. *Biophysical journal* **2007**, *93*, 2056–2068.

[30] Shah, J.; Atienza, J. M.; Rawlings, a. V.; Shipley, G. G. *Journal of lipid research* **1995**, *36*, 1945–1955.

[31] Brockman, H. L.; Momsen, M. M.; Brown, R. E.; He, L.; Chun, J.; Byun, H.-S.; Bittman, R. *Biophysical journal* **2004**, *87*, 1722–1731.

[32] Moore, D. J.; Rerek, M. E.; Mendelsohn, R. *International Journal of Cosmetic Science* **1999**, *21*, 353–368.

[33] Höltje, M.; Förster, T.; Brandt, B.; Engels, T.; Von Rybinski, W.; Höltje, H. D. *Biochimica et Biophysica Acta* **2001**, *1511*, 156–167.

[34] Berger, O.; Edholm, O.; Jähnig, F. *Biophysical Journal* **1997**, *72*, 2002–2013.

[35] Papadimitriou, N. I.; Kainourgiakis, M. E.; Karozis, S. N.; Charalambopoulou, G. C. *Molecular Simulation* **2015**, *41*, 1122–1136.

[36] Moore, T. C.; Iacovella, C. R.; Hartkamp, R.; Bunge, A. L.; McCabe, C. *The Journal of Physical Chemistry B* **2016**, *120*, 9944–9958, PMID: 27564869.

[37] Boddé, H. E.; Kruithof, M. A. M.; Brussee, J.; Koerten, H. K. *International Journal of Pharmaceutics* **1989**, *53*, 13–24.

[38] Akomeah, F. K.; Martin, G. P.; Brown, M. B. *Journal of Pharmaceutical Sciences* **2007**, *96*, 824–834.

[39] Dias, M.; Hadgraft, J.; Lane, M. E. *International Journal of Pharmaceutics* **2007**, *340*, 65–70.

[40] Franz, T. *The Journal of investigative dermatology* **1975**, *64*, 190–195.

[41] Marrink, S.-J.; Berendsen, H. J. C. *Journal of Physical Chemistry* **1994**, *98*, 4155–4168.

[42] Marrink, S. J.; Berendsen, H. J. C. *Journal of Physical Chemistry* **1996**, *100*, 16729–16738.

[43] Bemporad, D.; Essex, J. W.; Luttmann, C. *The Journal of Physical Chemistry B* **2004**, *108*, 4875–4884.

[44] Bemporad, D.; Luttmann, C.; Essex, J. W. *Biochimica et Biophysica Acta (BBA) - Biomembranes* **2005**, *1718*, 1–21.

[45] Das, C.; Olmsted, P. D.; Noro, M. G. *Soft Matter* **2009**, *5*, 4549.

[46] Paloncýová, M.; DeVane, R. H.; Murch, B. P.; Berka, K.; Otyepka, M. *Langmuir* **2014**, *30*, 13942–13948.

[47] Gupta, R.; Dwadasi, B. S.; Rai, B. *The Journal of Physical Chemistry B* **2016**, *120*, 12536–12546.

[48] Gupta, R.; Sridhar, D. B.; Rai, B. *The Journal of Physical Chemistry B* **2016**, *120*, 8987–8996.

[49] Orsi, M.; Essex, J. W. *Soft Matter* **2010**, *6*, 3797.

[50] Williams, A. C.; Barry, B. W. *Advanced Drug Delivery Reviews* **2004**, *56*, 603–618.

[51] Barry, B. W. *Journal of Controlled Release* **1987**, *6*, 85–97.

[52] Karande, P.; Jain, A.; Mitragotri, S. *Nature biotechnology* **2004**, *22*, 192–197.

[53] Cooper, E. R. *Journal of Pharmaceutical Sciences* **1984**, *73*, 1153–1156.

[54] Barry, B. W.; Bennett, S. L. *Journal of Pharmacy and Pharmacology* **1987**, *39*, 535–546.

[55] Williams, A. C.; Barry, B. W. *Advanced Drug Delivery Reviews* **2012**, *64, Supple*, 128–137.

[56] Lane, M. E. *International Journal of Pharmaceutics* **2013**, *447*, 12–21.

[57] Maghraby, G. M. M. E.; Williams, A. C.; Barry, B. W. *International Journal of Pharmaceutics* **2004**, *276*, 143–161.

[58] Dominiczak, A. F.; McLaren, Y.; Kusel, J. R.; Ball, D. L.; Goodfriend, T. L.; Bohr, D. F.; Reid, J. L. *American Journal of Hypertension* **1993**, *6*, 1003.

[59] Tzonou, A.; Lipworth, L.; Garidou, A.; Signorello, L. B.; Lagiou, P.; Hsieh, C.-c.; Trichopoulos, D. *International Journal of Cancer* **1996**, *68*, 300–304.

[60] Ruiz-Gutiérrez, V.; Muriana, F. J. G.; Guerrero, A.; Cert, A. M.; Villar, J. *Journal of hypertension* **1996**, *14*, 1483–1490.

[61] Funari, S. S.; Barceló, F.; Escribá, P. V. *Journal of lipid research* **2003**, *44*, 567–575.

[62] Hardman, W. E. *The Journal of Nutrition* **2004**, *134*, 3427S–3430S.

[63] Inoue, T.; Yanagihara, S.; Misono, Y.; Suzuki, M. *Chemistry and Physics of Lipids* **2001**, *109*, 117–133.

[64] da Silva, A. M. G.; Romão, R. I. S. *Chemistry and Physics of Lipids* **2005**, *137*, 62–76.

[65] Busquets, M. A.; Mestres, C.; Alsina, M. A.; Antón, J.; Reig, F. *Thermochimica Acta* **1994**, *232*, 261–269.

[66] Tanojo, H.; Geest, A. B.-v.; Bouwstra, J. A.; Junginger, H. E.; Boodé, H. E. *Thermochimica Acta* **1997**, *293*, 77–85.

[67] Francoeur, M. L.; Golden, G. M.; Potts, R. O. *Pharmaceutical research* **1990**, *7*, 621–627.

[68] Ongpipattanakul, B.; Burnette, R. R.; Potts, R. O.; Francoeur, M. L. *Pharmaceutical research* **1991**, *8*, 350–354.

[69] Kligman, A. *JAMA* **1965**, *193*, 796–804.

[70] Anigbogu, A. N. C.; Williams, A. C.; Barry, B. W.; Edwards, H. G. M. *International Journal of Pharmaceutics* **1995**, *125*, 265–282.

[71] Laden, K. *J Soc Cosmet Chem* **1968**, *19*.

[72] Notman, R.; Noro, M.; O'Malley, B.; Anwar, J. *Journal of the American Chemical Society* **2006**, *128*, 13982–13983.

[73] Gurtovenko, A. A.; Anwar, J. *The journal of physical chemistry. B* **2007**, *111*, 10453–10460.

[74] Gurtovenko, A. A.; Anwar, J. *The Journal of Physical Chemistry B* **2007**, *111*, 13379–13382.

[75] Hanslick, J. L.; Lau, K.; Noguchi, K. K.; Olney, J. W.; Zorumski, C. F.; Mennerick, S.; Farber, N. B. *Neurobiology of Disease* **2009**, *34*, 1–10.

[76] Gurtovenko, A. A.; Anwar, J. *The Journal of Physical Chemistry B* **2009**, *113*, 1983–1992.

[77] Busquets, M. A.; Mestres, C.; Alsina, M. A.; Anton, J. M. G. **1993**, 261–269.

[78] Notman, R.; Noro, M. G.; Anwar, J. *The journal of physical chemistry. B* **2007**, *111*, 12748–12755.

[79] Hoopes, M. I.; Noro, M. G.; Longo, M. L.; Faller, R. *The journal of physical chemistry. B* **2011**, *115*, 3164–3171.

[80] Akinshina, A.; Das, C.; Noro, M. G. *Phys. Chem. Chem. Phys.* **2016**, *18*, 17446–17460.

[81] Peters, G. H.; Hansen, F. Y.; Møller, M. S.; Westh, P. *The Journal of Physical Chemistry B* **2009**, *113*, 92–102.

[82] Leekumjorn, S.; Cho, H. J.; Wu, Y.; Wright, N. T.; Sum, A. K.; Chan, C. *Biochimica et Biophysica Acta (BBA) - Biomembranes* **2009**, *1788*, 1508–1516.

[83] Weiner, S. J.; Kollman, P. A.; Nguyen, D. T.; Case, D. A. *Journal of Computational Chemistry* **1986**, *7*, 230–252.

[84] Allinger, N. L.; Yuh, Y. H.; Lii, J. H. *Journal of the American Chemical Society* **1989**, *111*, 8551–8566.

[85] Wolfe, S.; Rauk, A.; Tel, L. M.; Csizmadia, I. G. *J. Chem. Soc. B* **1971**, 136–145.

[86] Jorgensen, W. L.; Tirado-Rives, J. *Journal of the American Chemical Society* **1988**, *110*, 1657–1666.

[87] Dickson, C. J.; Madej, B. D.; Skjevik, . A.; Betz, R. M.; Teigen, K.; Gould, I. R.; Walker, R. C. *Journal of Chemical Theory and Computation* **2014**, *10*, 865–879, PMID: 24803855.

[88] Klauda, J. B.; Venable, R. M.; Freites, J. A.; OConnor, J. W.; Tobias, D. J.; Mondragon-Ramirez, C.; Vorobyov, I.; MacKerell, A. D.; Pastor, R. W. *The Journal of Physical Chemistry B* **2010**, *114*, 7830–7843, PMID: 20496934.

[89] Poger, D.; Van Gunsteren, W. F.; Mark, A. E. *Journal of Computational Chemistry* **2010**, *31*, 1117–1125.

[90] Ryckaert, J.-P.; Bellemans, A. *Chemical Physics Letters* **1975**, *30*, 123 – 125.

[91] Mombelli, E.; Morris, R.; Taylor, W.; Fraternali, F. *Biophysical Journal* **2003**, *84*, 1507 – 1517.

[92] Verlet, L. *Phys. Rev.* **1967**, *159*, 98–103.

[93] Hockney, R. W.; Goel, S. P.; Eastwood, J. W. *Journal of Computational Physics* **1974**, *14*, 148–158.

[94] Berendsen, H. J. C.; Postma, J. P. M.; van Gunsteren, W. F.; DiNola, A.; Haak, J. R. *The Journal of Chemical Physics* **1984**, *81*, 3684–3690.

[95] Bussi, G.; Donadio, D.; Parrinello, M. *The Journal of Chemical Physics* **2007**, *126*, 14101.

[96] Nosé, S. *The Journal of Chemical Physics* **1984**, *81*, 511.

[97] Hoover, W. G. *Phys. Rev. A* **1985**, *31*, 1695–1697.

[98] Parrinello, M.; Rahman, A. *Journal of Applied Physics* **1981**, *52*, 7182–7190.

[99] Nosé, S.; Klein, M. L. *Molecular Physics* **1983**, *50*, 1055–1076.

[100] Metropolis, N.; Rosenbluth, A. W.; Rosenbluth, M. N.; Teller, A. H.; Teller, E. *The Journal of Chemical Physics* **1953**, *21*, 1087.

[101] Ewald, P. P. *Annalen der Physik* **1921**, *369*, 253–287.

[102] Hockney, R. W.; Eastwood, J. W. *Computer Simulation Using Particles*; Advanced book program: Addison-Wesley; McGraw-Hill, 1981.

[103] Ryckaert, J.-P.; Ciccotti, G.; Berendsen, H. J. *Journal of Computational Physics* **1977**, *23*, 327 – 341.

[104] Hess, B.; Bekker, H.; Berendsen, H. J. C.; Fraaije, J. G. E. M. *Journal of Computational Chemistry* **1997**, *18*, 1463–1472.

[105] Kstner, J. *Wiley Interdisciplinary Reviews: Computational Molecular Science* **2011**, *1*, 932–942.

[106] Barducci, A.; Bonomi, M.; Parrinello, M. *Wiley Interdisciplinary Reviews: Computational Molecular Science* **2011**, *1*, 826–843.

[107] Bemporad, D.; Luttmann, C.; Essex, J. W. *Biophysical journal* **2004**, *87*, 1–13.

[108] Marrink, S. J.; de Vries, A. H.; Mark, A. E. *The Journal of Physical Chemistry B* **2004**, *108*, 750–760.

[109] Monticelli, L.; Kandasamy, S. K.; Periole, X.; Larson, R. G.; Tieleman, D. P.; Marrink, S.-J. *Journal of Chemical Theory and Computation* **2008**, *4*, 819–834, PMID: 26621095.

[110] Marrink, S. J.; Risselada, H. J.; Yefimov, S.; Tieleman, D. P.; de Vries, A. H. *The journal of physical chemistry. B* **2007**, *111*, 7812–24.

[111] Ramadurai, S.; Holt, A.; Schafer, L. V.; Krasnikov, V. V.; Rijkers, D. T. S.; Marrink, S. J.; Killian, J. A.; Poolman, B. *Biophysical Journal* **2010**, *99*, 1447–1454.

[112] de Jong, D. H. A molecular view on the organizational complexity of proteins in membranes. Ph.D. thesis, 2013.

[113] Xu, T.; Zvelindovsky, A. V.; Sevink, G. J. A.; Lyakhova, K. S.; Jinnai, H.; Russell, T. P. *Macromolecules* **2005**, *38*, 10788–10798.

[114] Cooke, I. R.; Kremer, K.; Deserno, M. *Phys. Rev. E* **2005**, *72*, 011506.

[115] Wang, Z.-J.; Frenkel, D. *The Journal of Chemical Physics* **2005**, *122*, 234711.

[116] Frink, L. J. D.; Frischknecht, A. L. *Phys. Rev. E* **2005**, *72*, 041923.

[117] Markvoort, A. J.; Pieterse, K.; Steijaert, M. N.; Spijker, P.; Hilbers, P. A. J. *The Journal of Physical Chemistry B* **2005**, *109*, 22649–22654, PMID: 16853948.

[118] Pool, R.; Bolhuis, P. G. *Phys. Chem. Chem. Phys.* **2006**, *8*, 941–948.

[119] Izvekov, S.; Voth, G. A. *The Journal of Physical Chemistry B* **2005**, *109*, 2469–2473, PMID: 16851243.

[120] Elezgaray, J.; Laguerre, M. *Computer Physics Communications* **2006**, *175*, 264 – 268.

[121] Monticelli, L. *Journal of Chemical Theory and Computation* **2012**, *8*, 1370–1378.

[122] MacCallum, J. L.; Bennett, W. F. D.; Tieleman, D. P. *Biophysical journal* **2008**, *94*, 3393–3404.

[123] de Jong, D. H.; Periole, X.; Marrink, S. J. *Journal of Chemical Theory and Computation* **2012**, *8*, 1003–1014, PMID: 26593362.

[124] Risselada, H. J.; Marrink, S. J. *Proceedings of the National Academy of Sciences* **2008**, *105*, 17367–17372.

[125] Singh, G.; Tieleman, D. P. *Journal of Chemical Theory and Computation* **2011**, *7*, 2316–2324.

[126] Monticelli, L.; Tieleman, D. P.; Fuchs, P. F. J. *Biophysical journal* **2010**, *99*, 1455–1464.

[127] Castillo, N.; Monticelli, L.; Barnoud, J.; Tieleman, D. P. *Chemistry and Physics of Lipids* **2013**, *169*, 95–105.

[128] Sengupta, D.; Marrink, S. J. *Phys. Chem. Chem. Phys.* **2010**, *12*, 12987–12996.

[129] Marrink, S. J.; Periole, X.; Tieleman, D. P.; de Vries, A. H. *Phys. Chem. Chem. Phys.* **2010**, *12*, 2254–2256.

[130] Dahlberg, M. *The Journal of Physical Chemistry B* **2007**, *111*, 7194–7200, PMID: 17542632.

[131] Lopez, C. A.; Sovova, Z.; van Eerden, F. J.; de Vries, A. H.; Marrink, S. J. *Journal of Chemical Theory and Computation* **2013**, *9*, 1694–1708, PMID: 26587629.

[132] Lee, H.; Pastor, R. W. *The Journal of Physical Chemistry B* **2011**, *115*, 7830–7837, PMID: 21618987.

[133] Ogushi, F.; Ishitsuka, R.; Kobayashi, T.; Sugita, Y. *Chemical Physics Letters* **2012**, *522*, 96 – 102.

[134] Hinner, M. J.; Marrink, S.-J.; de Vries, A. H. *The Journal of Physical Chemistry B* **2009**, *113*, 15807–15819, PMID: 19894688.

[135] Hu, M.; de Jong, D. H.; Marrink, S. J.; Deserno, M. *Faraday Discuss.* **2013**, *161*, 365–382.

[136] Fuhrmans, M.; Marrink, S. J. *Journal of the American Chemical Society* **2012**, *134*, 1543–1552, PMID: 22191854.

[137] Periole, X.; Huber, T.; Marrink, S.-J.; Sakmar, T. P. *Journal of the American Chemical Society* **2007**, *129*, 10126–10132, PMID: 17658882.

[138] Frederix, P. W. J. M.; Ulijn, R. V.; Hunt, N. T.; Tuttle, T. *The Journal of Physical Chemistry Letters* **2011**, *2*, 2380–2384, PMID: 23795243.

[139] Yefimov, S.; van der Giessen, E.; Onck, P. R.; Marrink, S. J. *Biophysical Journal* **2008**, *94*, 2994 – 3002.

[140] Ahmad, S.; Johnston, B. F.; Mackay, S. P.; Schatzlein, A. G.; Gellert, P.; Sengupta, D.; Uchegbu, I. F. *Journal of The Royal Society Interface* **2010**, *7*, S423–S433.

[141] Shih, A. Y.; Freddolino, P. L.; Arkhipov, A.; Schulten, K. *Journal of Structural Biology* **2007**, *157*, 579 – 592, Advances in Molecular Dynamics Simulations.

[142] Baoukina, S.; Tieleman, D. P. *Biophysical Journal* **2010**, *99*, 2134 – 2142.

[143] Kulovesi, P.; Telenius, J.; Koivuniemi, A.; Brezesinski, G.; Rantamki, A.; Viitala, T.; Puukilainen, E.; Ritala, M.; Wiedmer, S. K.; Vattulainen, I.; Holopainen, J. M. *Biophysical Journal* **2010**, *99*, 2559 – 2567.

[144] Lopez, C. A.; Rzepiela, A. J.; de Vries, A. H.; Dijkhuizen, L.; Hnenberger, P. H.; Marrink, S. J. *Journal of Chemical Theory and Computation* **2009**, *5*, 3195–3210, PMID: 26602504.

[145] Rossi, G.; Fuchs, P. F. J.; Barnoud, J.; Monticelli, L. *The Journal of Physical Chemistry B* **2012**, *116*, 14353–14362, PMID: 23137188.

[146] Dong, J.; Zhou, J. *Macromolecular Theory and Simulations* **2013**, *22*, 174–186.

[147] Melo, M. N.; Ingólfsson, H. I.; Marrink, S. J. *The Journal of Chemical Physics* **2015**, *143*, 243152.

[148] Fritz, D.; Koschke, K.; Harmandaris, V. A.; van der Vegt, N. F. A.; Kremer, K. *Phys. Chem. Chem. Phys.* **2011**, *13*, 10412–10420.

[149] Yesylevskyy, S. O.; Schfer, L. V.; Sengupta, D.; Marrink, S. J. *PLOS Computational Biology* **2010**, *6*, 1–17.

[150] Waheed, Q.; Tjörnhammar, R.; Edholm, O. *Biophysical Journal* **2012**, *103*, 2125–2133.

[151] Rodgers, J. M.; Sørensen, J.; de Meyer, F. J.-M.; Schiøtt, B.; Smit, B. *The Journal of Physical Chemistry B* **2012**, *116*, 1551–1569.

[152] Lai, K.; Wang, B.; Zhang, Y.; Zhang, Y. *Phys. Chem. Chem. Phys.* **2012**, *14*, 5744–5752.

[153] Sun, S.; Wong, J. T. Y.; Zhang, T.-Y. *Soft Matter* **2011**, *7*, 147–152.

[154] Guo, S.; Moore, T. C.; Iacovella, C. R.; Strickland, L. A.; McCabe, C. *Journal of Chemical Theory and Computation* **2013**, *9*, 5116–5126.

[155] Metcalf, R.; Pandit, S. A. *The Journal of Physical Chemistry B* **2012**, *116*, 4500–4509.

[156] Notman, R.; den Otter, W. K.; Noro, M. G.; Briels, W. J.; Anwar, J. *Biophysical journal* **2007**, *93*, 2056–68.

[157] Marrink, S. J.; Risselada, J.; Mark, A. E. *Chemistry and Physics of Lipids* **2005**, *135*, 223–244.

[158] Yu, Z. W.; Quinn, P. J. *Bioscience Reports* **1994**, *14*, 259–281.

[159] Geerke, D. P.; Oostenbrink, C.; van der Vegt, N. F. A.; van Gunsteren, W. F. *The Journal of Physical Chemistry B* **2004**, *108*, 1436–1445.

[160] RASMUSSEN, D. H.; MACKENZIE, A. P. *Nature* **1968**, *220*, 1315.

[161] Yu, Z. W.; Quinn, P. J. *Biophysical Journal* **1995**, *69*, 1456–1463.

[162] Sum, A. K.; de Pablo, J. J. *Biophysical Journal* **2003**, *85*, 3636–3645.

[163] Thind, R.; O'Neill, D. W.; Del Regno, A.; Notman, R. *Chem. Commun.* **2015**, *51*, 5406–5409.

[164] Berendsen, H. J. C.; Postma, J. P. M.; Van Gunsteren, W. F.; Hermans, J. *Intermolecular Forces* **1981**, *11*, 331–338.

[165] Hess, B.; Kutzner, C.; van der Spoel, D.; Lindahl, E. *Journal of Chemical Theory and Computation* **2008**, *4*, 435–447.

[166] Lavrijsen, A. P. M.; Bouwstra, J. A.; Gooris, G. S.; Weerheim, A.; Boddé, H. E.; Ponec, M. *Journal of Investigative Dermatology* **1995**, *105*, 619–624.

[167] Yamamoto, A.; Serizawa, S.; Ito, M.; Sato, Y. *Archives of Dermatological Research* **1991**, *283*, 219–223.

[168] Wertz, P. W.; Swartzendruber, D. C.; Abraham, W.; Madison, K. C.; Downing, D. T. *Archives of Dermatology* **1987**, *123*, 1381–1384.

[169] Melnik, B.; Hollmann, J.; Plewig, G. *British Journal of Dermatology* **1988**, *119*, 547–548.

[170] Motta, S.; Monti, M.; Sesana, S.; Caputo, R.; Carelli, S.; Ghidoni, R. *Biochimica et Biophysica Acta* **1993**, *1182*, 147–151.

[171] Tagami, H.; Kobayashi, H.; O'goshi, K.; Kikuchi, K. *Journal of Cosmetic Dermatology* **2006**, *5*, 140–149.

[172] Choi, E. H.; Man, Ã. M.-q.; Wang, Ã. F.; Zhang, X.; Brown, B. E.; Feingold, K. R.; Ã, P. M. E. **2005**, 288–293.

[173] Ishikawa, J.; Yoshida, H.; Ito, S.; Naoe, A.; Fujimura, T.; Kitahara, T.; Takema, Y.; Zerweck, C.; Grove, G. L. *J Cosmet Dermatol* **2013**, *12*, 3–11.

[174] Lisante, T. A.; Nunez, C.; Zhang, P.; Mathes, B. M. *Journal of drugs in dermatology : JDD* **2017**, *16*, 671676.

[175] Stettler, H.; Kurka, P.; Wagner, C.; Sznurkowska, K.; Czernicka, O.; Bhling, A.; Bielfeldt, S.; Wilhelm, K.-P.; Lenz, H. *Journal of Dermatological Treatment* **2017**, *28*, 251–257, PMID: 27545858.

[176] Koppes, S. A.; Charles, F.; Lammers, L. A.; Frings-Dresen, M.; Kezic, S.; Ruste-Meyer, T. *Acta Dermato-Venereologica* **2016**, *96*.

[177] Simpson, E.; Bhling, A.; Bielfeldt, S.; Bosc, C.; Kerrouche, N. *Journal of Dermatological Treatment* **2013**, *24*, 122–125, PMID: 22812593.

[178] Oh, M. J.; Cho, Y. H.; Cha, S. Y.; Lee, E. O.; Kim, J. W.; Kim, S. K.; Park, C. S. Novel phytoceramides containing fatty acids of diverse chain lengths are better than a single C18-ceramide N-stearoyl phytosphingosine to improve the physiological properties of human stratum corneum. 2017.

[179] Choi, H. K.; Cho, Y. H.; Lee, E. O.; Kim, J. W.; Park, C. S. *Archives of dermatological research* **2017**, *309*, 795803.

[180] Huang, H.; Chang, T. *International Journal of Dermatology 47*, 812–819.

[181] Sanghun, J.; Yunhi, C. *Journal of Medicinal Food* **2015**, *18*, 999–1006, PMID: 26355951.

[182] Morifuji, M.; Oba, C.; Ichikawa, S.; Ito, K.; Kawahata, K.; Asami, Y.; Ikegami, S.; Itoh, H.; Sugawara, T. *Journal of Dermatological Science* **2015**, *78*, 224 – 231.

[183] Warner, R. R.; Myers, M. C.; Taylor, D. A. *The Journal of investigative dermatology* **1988**, *90*, 218–224.

[184] Yadav, S.; Wickett, R. R.; Pinto, N. G.; Kasting, G. B.; Thiel, S. W. *Skin Research and Technology* **2009**, *15*, 172–179.

[185] Bernstein, J. E. *Clinics in Dermatology* **1996**, *14*, 567–569.

[186] Madison, K. C. *Journal of Investigative Dermatology* **2003**, *121*, 231–241.

[187] Groen, D.; Gooris, G. S.; Barlow, D. J.; Lawrence, M. J.; van Mechelen, J. B.; Demé, B.; Bouwstra, J. A. *Biophysical Journal* **2011**, *100*, 1481–1489.

[188] Fitter, J.; Lechner, R. E.; Dencher, N. A. *The Journal of Physical Chemistry B* **1999**, *103*, 8036–8050.

[189] Ulrich, A. S.; Watts, A. *Biophysical Journal* **1994**, *66*, 1441–1449.

[190] Binder, H. *European Biophysics Journal* **2006**, *36*, 265–279.

[191] Sirota, E. B.; Smith, G. S.; Safinya, C. R.; Plano, R. J.; Clark, N. A. *Science* **1988**, *242*, 1406–1409.

[192] Raghunathan, V. A.; Katsaras, J. *Phys. Rev. Lett.* **1995**, *74*, 4456–4459.

[193] Trapp, M.; Gutberlet, T.; Juranyi, F.; Unruh, T.; Dem, B.; Tehei, M.; Peters, J. *The Journal of Chemical Physics* **2010**, *133*, 164505.

[194] Jendrasiak, G. L.; Smith, R. L. *Chemistry and Physics of Lipids* **2001**, *113*, 55 – 66.

[195] Tfayli, A.; Jamal, D.; Vyumvuhore, R.; Manfait, M.; Baillet-Guffroy, A. *The Analyst* **2013**, *138*, 6582.

[196] Garidel, P.; Flting, B.; Schaller, I.; Kerth, A. *Biophysical Chemistry* **2010**, *150*, 144 – 156, Special Issue: Membrane Interacting Peptides - Towards the Understanding of Biological Membranes.

[197] Tan, G.; Xu, P.; Lawson, L. B.; He, J.; Freytag, L. C.; Clements, J. D.; John, V. T. *Journal of Pharmaceutical Sciences 99*, 730–740.

[198] Raudenkolb, S.; Wartewig, S.; Brezesinski, G.; Funari, S. S.; Neubert, R. H. *Chemistry and Physics of Lipids* **2005**, *136*, 13 – 22.

[199] Högberg, C.-J.; Lyubartsev, A. P. *The Journal of Physical Chemistry B* **2006**, *110*, 14326–14336.

[200] Mashl, R. J.; Scott, H. L.; Subramaniam, S.; Jakobsson, E. *Biophysical journal* **2001**, *81*, 3005–3015.

[201] Pinnick, E. R.; Erramilli, S.; Wang, F. *Molecular Physics* **2010**, *108*, 2027–2036.

[202] Zhang, Z.; Berkowitz, M. L. *The Journal of Physical Chemistry B* **2009**, *113*, 7676–7680, PMID: 19413360.

[203] Mashaghi, A.; Partovi-Azar, P.; Jadidi, T.; Nafari, N.; Maass, P.; Tabar, M. R. R.; Bonn, M.; Bakker, H. J. *The Journal of Chemical Physics* **2012**, *136*, 114709.

[204] Del Regno, A.; Notman, R. *Phys. Chem. Chem. Phys.* **2018**, *20*, 2162–2174.

[205] MacDermaid, C. M.; Devane, R. H.; Klein, M. L.; Fiorin, G. *Biophysical Journal* **2015**, *108*, 243a.

[206] Kutzner, C.; Grubmüller, H.; de Groot, B. L.; Zachariae, U. *Biophysical Journal* **2011**, *101*, 809–817.

[207] Kopfer, D. A.; Song, C.; Zachariae, U.; de Groot, B. L. *Biophysical Journal* **2014**, *106*, 539a.

[208] Machtens, J.-P.; Briones, R.; Alleva, C.; de Groot, B. L.; Fahlke, C. *Biophysical Journal* **2017**, *112*, 1396–1405.

[209] Shi, C.; He, Y.; Hendriks, K.; de Groot, B. L.; Cai, X.; Tian, C.; Lange, A.; Sun, H. *Nature Communications* **2018**, *9*, 717.

[210] Murad, S.; Powles, J. G. *The Journal of Chemical Physics* **1993**, *99*, 7271–7272.

[211] Kalra, A.; Garde, S.; Hummer, G. *Proceedings of the National Academy of Sciences* **2003**, *100*, 10175–10180.

[212] Iwai, I.; Han, H.; den Hollander, L.; Svensson, S.; Öfverstedt, L.-G.; Anwar, J.; Brewer, J.; Bloksgaard, M.; Laloeuf, A.; Nosek, D.; Masich, S.; Bagatolli, L. A.; Skoglund, U.; Norlén, L. *Journal of Investigative Dermatology* **2012**, *132*, 2215–2225.

[213] Das, C.; Noro, M. G.; Olmsted, P. D. *Phys. Rev. Lett.* **2013**, *111*, 148101.

[214] Das, C.; Noro, M. G.; Olmsted, P. D. *Soft Matter* **2014**, *10*, 7346–7352.

[215] Moore, T. C.; Iacovella, C. R.; Leonhard, A. C.; Bunge, A. L.; MCabe, C. *Biochemical and Biophysical Research Communications* **2017**,

[216] Guixa-Gonzalez, R.; Rodriguez-Espigares, I.; Ramirez-Anguita, J. M.; Carrio-Gaspar, P.; Martinez-Seara, H.; Giorgino, T.; Selent, J. *Bioinformatics* **2014**, *30*, 1478–1480.

[217] Humphrey, W.; Dalke, A.; Schulten, K. *Journal of Molecular Graphics* **1996**, *14*, 33–38.

[218] Dahlén, B.; Pascher, I. *Chemistry and Physics of Lipids* **1979**, *24*, 119–133.

[219] Löfgren, H.; Pascher, I. *Chemistry and Physics of Lipids* **1977**, *20*, 273–284.

[220] Högberg, C.-J.; Lyubartsev, A. P. *The Journal of Physical Chemistry B* **2006**, *110*, 14326–14336.

[221] Santoyo, S.; Ygartua, P. *European Journal of Pharmaceutics and Biopharmaceutics* **2000**, *50*, 245–250.

[222] Lopes, L. B.; Collett, J. H.; Bentley, M. V. L. B. *European Journal of Pharmaceutics and Biopharmaceutics* **2005**, *60*, 25–30.

[223] Lopes, L. B.; Lopes, J. L. C.; Oliveira, D. C. R.; Thomazini, J. A.; Garcia, M. T. J.; Fantini, M. C. A.; Collett, J. H.; Bentley, M. V. L. B. *European Journal of Pharmaceutics and Biopharmaceutics* **2006**, *63*, 146–155.

[224] Lopes, L. B.; Speretta, F. F. F.; Bentley, M. V. L. B. *European Journal of Pharmaceutical Sciences* **2007**, *32*, 209–215.

[225] Leyden, J. J.; Rawlings Anthony V., . *Skin moisturization*; New York : Marcel Dekker, 2002.

[226] Golden, G. M.; Guzek, D. B.; Kennedy, A. E.; McKie, J. E.; Potts, R. O. *Biochemistry* **1987**, *26*, 2382–2388, PMID: 3620451.

[227] Blank, I. H.; Moloney, J.; Emslie, A. G.; Simon, I.; Apt, C. *Journal of Investigative Dermatology* **1984**, *82*, 188 – 194.

[228] Potts, R. O.; Francoeur, M. L. *Journal of Investigative Dermatology* **1991**, *96*, 495 – 499.

[229] Schatzberg, P. *The Journal of Physical Chemistry* **1963**, *67*, 776–779.

[230] Scheuplein, R. J.; Blank, I. H. *Physiological Reviews* **1971**, *51*, 702–747.

[231] ALLENBY, A. C.; FLETCHER, J.; SCHOCK, C.; TEES, T. F. S. *British Journal of Dermatology 81*, 31–39.

[232] Mark, P.; Nilsson, L. *The Journal of Physical Chemistry A* **2001**, *105*, 9954–9960.

[233] van der Spoel, D.; van Maaren, P. J.; Berendsen, H. J. C. *The Journal of Chemical Physics* **1998**, *108*, 10220–10230.

[234] Mills, R. *The Journal of Physical Chemistry* **1973**, *77*, 685–688.

[235] Hachem, J.-P.; Crumrine, D.; Fluhr, J.; Brown, B. E.; Feingold, K. R.; Elias, P. M. *Journal of Investigative Dermatology* **2003**, *121*, 345–353.

[236] Leontiadou, H.; Mark, A. E.; Marrink, S.-J. *Biophysical Journal* **2007**, *92*, 4209–4215.

[237] Feller, S. E.; Pastor, R. W. *The Journal of Chemical Physics* **1999**, *111*, 1281–1287.

[238] Tieleman, D. P.; Berendsen, H. J. C. *The Journal of Chemical Physics* **1996**, *105*, 4871–4880.

[239] Lindahl, E.; Edholm, O. *Biophysical Journal* **2000**, *79*, 426–433.

[240] Marrink, S. J.; Mark, A. E. *The Journal of Physical Chemistry B* **2001**, *105*, 6122–6127.

[241] Castro-Román, F.; Benz, R. W.; White, S. H.; Tobias, D. J. *The Journal of Physical Chemistry B* **2006**, *110*, 24157–24164.

[242] de Vries, A. H.; Chandrasekhar, I.; van Gunsteren, W. F.; Hünenberger, P. H. *The Journal of Physical Chemistry B* **2005**, *109*, 11643–11652.

[243] Essmann, U.; Berkowitz, M. L. *Biophysical Journal* **1999**, *76*, 2081–2089.

[244] Lindahl, E.; Edholm, O. *The Journal of Chemical Physics* **2001**, *115*, 4938–4950.

[245] Patra, M.; Karttunen, M.; Hyvönen, M. T.; Falck, E.; Vattulainen, I. *The Journal of Physical Chemistry B* **2004**, *108*, 4485–4494.

[246] Yeh, I.-C.; Hummer, G. *The Journal of Physical Chemistry B* **2004**, *108*, 15873–15879.

[247] Klauda, J. B.; Brooks, B. R.; MacKerell, A. D.; Venable, R. M.; Pastor, R. W. *The Journal of Physical Chemistry B* **2005**, *109*, 5300–5311.

[248] Klauda, J. B.; Brooks, B. R.; Pastor, R. W. *The Journal of Chemical Physics* **2006**, *125*, 144710.

[249] Hünenberger, P. H.; McCammon, J. A. *The Journal of Chemical Physics* **1999**, *110*, 1856–1872.

[250] Weber, W.; Hünenberger, P. H.; McCammon, J. A. *The Journal of Physical Chemistry B* **2000**, *104*, 3668–3675.

[251] Villarreal, M. A.; Montich, G. G. *Journal of Biomolecular Structure and Dynamics* **2005**, *23*, 135–142.

[252] Hünenberger, P. H.; McCammon, J. A. *Biophysical Chemistry* **1999**, *78*, 69–88.

[253] Rozanska, X.; Chipot, C. *The Journal of Chemical Physics* **2000**, *112*, 9691–9694.

[254] Batu, T.; Patra, S. M.; Kuyucak, S. *Chemical Physics Letters* **2006**, *425*, 320–323.

[255] Lee, S.-J.; Song, Y.; Baker, N. A. *Biophysical Journal* **2008**, *94*, 3565–3576.

[256] Gordeliy, V. I.; Kiselev, M. A.; Lesieur, P.; Pole, A. V.; Teixeira, J. *Biophysical Journal* **1998**, *75*, 2343–2351.

[257] Kiselev, M. A.; Lesieur, P.; Kisselev, A. M.; Grabielle-Madelmond, C.; Ollivon, M. *Journal of Alloys and Compounds* **1999**, *286*, 195–202.

[258] Shashkov, S. N.; Kiselev, M. A.; Tioutiounnikov, S. N.; Kiselev, A. M.; Lesieur, P. *Physica B: Condensed Matter* **1999**, *271*, 184–191.

[259] Kiselev, M. A.; Gutberlet, T.; Lesieur, P.; Hauss, T.; Ollivon, M.; Neubert, R. H. H. *Chemistry and Physics of Lipids* **2005**, *133*, 181–193.

[260] Chen, X.; Allen, H. C. *The Journal of Physical Chemistry A* **2009**, *113*, 12655–12662.

[261] Yu, Z. W.; Quinn, P. J. *Biochimica et biophysica acta* **2000**, *1509*, 440–450.

[262] de Ménorval, M.-A.; Mir, L. M.; Fernández, M. L.; Reigada, R. *PLOS ONE* **2012**, *7*, 1–12.

[263] Anigbogu, A. N. C.; Williams, A. C.; Barry, B. W.; Edwards, H. G. M. *International Journal of Pharmaceutics* **1995**, *125*, 265–282.